Wavelet Transform and Some of Its Real-World Applications

Edited by Dumitru Baleanu

WAVELET TRANSFORM AND SOME OF ITS REAL-WORLD APPLICATIONS

Edited by **Dumitru Baleanu**

Contributors

Zuofeng Zhou, Tilendra Shishir Sinha, Rajkumar Patra, Rohit Raja, Ravi Prakash Dubey, Devanshu Chakravarty, Mohammad Rezazadeh Mehrjou, Norman Mariun, Mahdi Karami, Sahar Zolfaghari, Samsul Bahari Mohd. Noor, Mohd Zainal Abidin Ab. Kadir, Norhisam Misron, Mohd. Amran Mohd. Radzi, Mohammad Hamiruce Marhaban, Gholamreza Anbarjafari, Pejman Rasti, Morteza Daneshmand, Cagri Ozcinar, Blanca E. Carvajal-Gamez, Omar Chavez, Martin Valtierra-Rodriguez, Juan Pablo Amezquita-Sanchez, Alejandro Mungaray, Luis Mario Rodriguez, Aurelio Dominguez

Notice

Statements and opinions expressed in the chapters are these of the individual contributors and not necessarily those of the editors or publisher. No responsibility is accepted for the accuracy of information contained in the published chapters. The publisher assumes no responsibility for any damage or injury to persons or property arising out of the use of any materials, instructions, methods or ideas contained in the book.

We are IntechOpen, the world's largest scientific publisher of Open Access books.

3,250+
Open access books available

106,000+
International authors and editors

112M+
Downloads

151
Countries delivered to

Our authors are among the
Top 1%
most cited scientists

12.2%
Contributors from top 500 universities
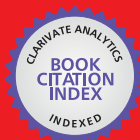
Interested in publishing with us?
Contact book.department@intechopen.com

Numbers displayed above are based on latest data collected.
For more information visit www.intechopen.com

Meet the editor

Dumitru Baleanu received a B.Sc. degree in Physics from the University of Craiova, Romania, in 1988, an M.Sc. degree from the University of Bucharest, Romania, in 1989, and a Ph.D. degree from the Institute of Atomic Physics, Romania, in 1996. He is Professor at the Institute of Space Sciences, Romania, and since 2000 he is visiting staff member at Cankaya University, Turkey. He published 500 papers in journals indexed in SCI. He is a co-editor of five books published by Springer. He is coauthor of three books published by Elsevier and World Scientific. He is an editorial board member of six ISI journals and is on the 2015 Highly Cited Researcher list in mathematics. His Hirsch index is 33.

Contents

Preface

Wavelets are excellent signal-processing tools that enable the analysis of several timescales of the local properties of complex signals presenting nonstationary zones. They have a large number of applications in several fields of science and engineering. The penetration of wavelets in the scientific community was very fast. This book presents some interesting real-world applications of wavelet theory.

In Chapter 1, we present the progressive–regressive strategy for biometrical authentication. Chapter 2 deals with the resolution enhancement–based image compression technique using singular value decomposition and wavelet transforms. In Chapter 3, we treat the adaptive wavelet packet transform. In Chapter 4, the scaling factor threshold estimator in different color models using a discrete wavelet transform for steganographic algorithms has been described. Chapter 5 explains the wavelet-based analysis of MCSA for fault detection in electrical machines. The book ends with Chapter 6 which discusses the empirical wavelet transform–based detection of anomalies in ULF geomagnetic signals associated with seismic activities with a fuzzy logic–based system for automatic diagnosis.

The book is intended for both students and researchers interested in the fascinating field of wavelet theory and its real-world applications.

Dumitru Baleanu
Cankaya University, Turkey

Progressive-Regressive Strategy for Biometrical Authentication

Tilendra Shishir Sinha, Raj Kumar Patra, Rohit Raja,
Devanshu Chakravarty and Ravi Prakash Dubey

Abstract

This chapter thoroughly investigates the use of the progressive–regressive strategy for biometrical authentication through the use of human gait and face images. A considerable amount of features were extracted and relevant parameters computed for such an investigation and a vast number of datasets developed. The datasets consist of features and computed parameters extracted from human gait and face images from various subjects of different ages. Soft-computing techniques, discrete wavelet transform (DWT), principal component analysis and the forward–backward dynamic programming method were applied for the best-fit selection of parameters and the complete matching process. The paretic and non-paretic characteristics were classified through Naïve Bayes' classification theorem. Both classification and recognition were carried out in parallel with test and trained datasets and the whole process of investigation was successfully carried out through an algorithm developed in this chapter. The success rate of biometrical authentication is 89%.

Keywords: Lifting scheme of discrete wavelet transform (LSDWT), inverse-lifting scheme of discrete wavelet transform (ILSDWT), soft-computing technique, unidirectional temporary associative memory technique (UTAM), forward–backward dynamic programming, principal component analysis

1. Introduction

This chapter attempts to explain the process of biometrical authentication by considering human gait and face images. The authentication process has been carried out in parallel with the test data and the trained data, which consists of a variety of human gait and face images taken of subjects of different ages.

This chapter is separated into three parts: the first deals with the general mathematical problem of formulating a model for biometrical authentication; the second provides a methodology for corpus formation using human gait and face images; and the third presents case studies for biometrical authentication, along with conclusions and applications. In the first part, the frames of images were mathematically analysed and normalised. They were categorised into odd and even components, thus validating the process of splitting the frames using the lifting scheme of discrete wavelet transform (LSDWT). The detail and coarser components have been estimated. Further the above calculated values have been used to validate the process of merging the frames through the inverse-lifting scheme of discrete wavelet transform (ILSDWT). A considerable amount of parameters have been estimated using statistical, digital and morphological image-processing methods. The next part of this chapter presents the experimental formation of two different corpuses: firstly a noise-free artificial gait model and secondly a noise-free artificial face model. The facts and figures of the above mentioned corpuses were reached and discussed in considerable length using; the LSDWT, the ILSDWT, soft-computing based techniques, the forward–backward dynamic programming of neural networks, the Unidirectional Temporary Associative Memory (UTAM) technique of neural network and fuzzy and genetic algorithms. In the third part of this chapter, two different case studies are considered for proper biometrical authentication and analysis. The analysis has been carried out both in progressive and regressive modes – the progressive mode of analysis meaning in an incremental way and the regressive in a decremental way. This chapter presents two case studies for progressive and regressive nature. In one case, the step length of gait has been considered – in pixels from each frame, whereby the subject is moving from left to right – and in another case, the face step angle – measured in degrees from each frame, whereby the subject's face is analysed from the side-view, parallel to the x-axis switched by five degrees. Prior to the analysis being carried out on the above case studies, an appropriate and desired analysis was carried out on the acquisition, enhancement, segmentation and pre-processing stages. In the acquisition stage, the original image was captured through a high-density web camera or a digital camera at random – meaning, the image was captured blindly using the image-warping technique. The image-warping technique is the combination of image registration and rectification. When the image of any subject has been captured blindly, the desired region of interest, along with the object of interest, are detected and selected. Image data is registered and rectified for the selected region, and object, of interest. 2D-transformation techniques such as translation, scaling and shearing were applied for registration and rectification. After the rectification of selected image data, proper and enhanced images were restored. Hence the background and foreground of the images were distinguished using proper image subtraction methods. In this chapter, the foreground part of the image (ROI and OOI) is discussed. This part was used for further processing such as; obtaining silhouette images using proper segmentation techniques, distinguishing the upper part (human face) and the lower part (human gait) of the object and computing the connected components of the upper and lower parts of the object. Considering these two portions of the object, relevant features were extracted, resulting in two knowledge-based models or corpuses.

For the biometrical authentication, a test image of the subject was captured. After proper enhancement, registration, rectification and segmentation of the test images, relevant features

were extracted and stored in the template. Using LSWT, the upper and lower portion of the test image was separated, forming two sub-templates: the Slave Human Gait Model (SHGM) and the Slave Human Face Model (SHFM). The data that was stored in the above two sub-templates was used for restoring the original image after employing the merging mechanism using the ILSWT. The later technique was applied for the verification of data that had been separated earlier using the LSWT method. After proper verification, authentication was carried out using soft-computing techniques and their hybrid approaches. Neuro-genetic and neuro-fuzzy approaches were applied as hybrid methods. Other methods for further processing were: Fisher's linear discriminant analysis (FLDA), discrete cosine transform, DWT and principal component analysis (PCA).

This chapter discusses an algorithm developed for the formation of noise-free corpuses, using relevant geometrical parameters which aid the authentication of a subject using human gait and face images. The complexity of the developed algorithm is also discussed using a case study on the change in the subject's getups. The trained data is matched with the test data for the best-fit which involves the application of forward–backward dynamic programming (FBDP), fuzzy set rules and genetic algorithms (GA).

2. Modelling for biometrical authentication

2.1. Brief literature survey on human gait as a biometrical trait

The analysis of human walking movements, or gait, has been an on-going area of research since the advent of the still camera in 1896. Since that time many researchers have investigated the dynamics of human gait in order to fully understand and describe the complicated process of upright bipedal motion as suggested by Boyd et al. [1], and Nixon et al. [2], and Murray et al. [3], and Ben-Abdelkader et al. [4]

Considerable research has been carried out exploiting the analysis of this motion, including: clinical gait analysis, used for rehabilitation purposes, and biometric gait analysis for automatic person identification.

In 2002 Ben-Abdelkader et al. [4] proposed a parametric method to automatically identify people in low-resolution videos by estimating the height and stride parameters of their gait. Later in 2004 Ben-Abdelkader et al. [5] proposed a method of interpreting gait as synchronised, integrated movements of hundreds of muscles and joints in the body. Kale and his colleagues [6] carried out work on an appearance-based approach to gait recognition. In their work the width of the outer contour of the binarized silhouette of a walking person is chosen as the basic image feature. Huang et al. [7] proposed an approach in 1998 which recognised people by their gait from a sequence of images. They proposed a statistical approach, which combined eigen-space transformation with canonical-space transformation for feature transformation of spatial templates. In 1997 Cunado et al. [8 proposed a method for evidencing gathering techniques. The proposed techniques were developed as a moving model, representing the motion of human thighs, providing an automatic gait signature. In 2002 Phillips et al. [9] proposed a

baseline algorithm for the challenge of identifying humans using gait analysis. In the same year Phillips [10] and his colleagues worked on the baseline algorithm, investigating problematic variations of gait identification, such as: view point, footwear, and walking surface. In 2008 Jack M. Wang et al. [11] introduced Gaussian process dynamic models for non-linear time series analysis to develop models of human pose and motion captured from high-dimensional data. The model proposed by Jack M. Wang et.al [11] comprises a low-dimensional latent space with associated dynamics, as well as a map from the latent space to an observation space. In the same year Sina Samangooei and M. S. Nixon [12] proposed a set of semantic traits discernible by humans at a distance, outlining their psychological validity. In 2011 Imed Bouchrika et al. [13] investigated the translation of gait biometrics for forensic use. They used ankle, knee and hip locations to derive a measure of match for image sequences of walking subjects. The match was achieved by instantaneous posture matching which determines the difference between the positions of a set of human vertices. In 2011 Sinha et al. [14] proposed a technique for the detection of abnormal footprints using human gait images. In 2012 Chen Wang et al. [15] proposed a strategy for the formation of a human gait corpus using the temporal information preserving gait template. Until now, a lot of research was dedicated to the recognition of individuals, by finding foot problems through human gait images. However, very little work has been completed on investigating progressive-regressive strategies for biometric authentication using human gait images. Keeping the progressive–regressive strategy, the extraction of features and its recognition for biometric authentication using DWT and soft-computing techniques has been discussed thoroughly using human gait images. In this chapter, biometric authentication through human gait is the topic of the first case study and human face from the side view as the second case study. The literature survey on human face is discussed in Section 2.2 of this chapter.

2.2. Brief literature survey on human face as biometrical trait

For six decades research has been carried out on human face. From the literature, it has been observed that, this work was not only completed by researchers from the field of engineering and technology, but also from the field of medical sciences. Automatic face recognition is one of the prime components for any biometrical study and it has gradually progressed over the past sixty years. A thorough review report was written and the issues for further research in this were investigated.

During the past few decades, a considerable amount of research into human face recognition has dealt with the immensely challenging variability in head pose, lighting intensity and direction, facial expression and aging. A great deal of progress has been made by many researchers in improving the performance of human face recognition. Based on two-dimensional intensity images, a number of human face recognition algorithms have been developed during this time. Trunk et al. [16] suggested a method called Principal component analysis (PCA) as the best method for the distribution of human face images within the entire image space. These vectors define the subspace of a human face image called the face space. Kirby et al. [17] has developed an idea for the extension of PCA, such as modular eigen-spaces. Hu Y. Jiang et al. [18] proposed a strategy using one neutral frontal-view image of human face. They

proposed a strategy of creating synthetic images under different poses and expressions to aid recognition. A similar idea, but a very new approach, was proposed by Lee et al. [19] who presented a combination of an edge model and a colour region model for human face recognition after the synthetic image using a 3D model. In the same year Michal Valstar et al. [20] attempted to measure a large range of facial behaviour by recognising facial action units (generally atomic facial signals) that produce expressions. The proposed system performs action unit recognition using temporal templates as input data. Jolly D. Shah et al. [21] presents a multiple human face detection method, based on skin colour information and a *lines of separability* face model and recognition method, based on principle component analysis and an artificial neural network. The face detection method uses a YCbCr colour model and sigma control limits for variation in its colour components. In 2007, Richa Singh et al. [22] described a human face mosaicking scheme that generates a composite human face image during registration or training, based on the evidence provided by the frontal-view and semi-profile human face image of an individual. In this scheme the side-view profile images are aligned with the frontal image using a hierarchical registration algorithm, which exploits neighbourhood properties to determine the transformation relating the two images together. In 2008, Edward Kao et al., [23] shared the process of automatically tracking people in video sequences, which is currently receiving a great deal of interest within the computer vision research community. In this work they contrasted the performance of the popular mean-shift algorithms gradient descent-based strategy with a more advanced swarm intelligence technique and proposed a practical swarm optimisation algorithm to replace the gradient descent search. They also combined the swarm-based search strategy with a probabilistic data association filter state estimator to perform the track association and maintenance stages. In the same year Xiaozheng Zhang et al. [24] presented a novel-appearance based approach in face recognition using frontal and side-views of human face images to tackle pose variation. This has great potential in forensic and security application, involving the police mugshot database. In 2011 Li Cheng et al. [25] examined the problem of the segmentation of foreground objects in live videos when background subtraction as minimizing a penalized instantaneous risk function-yield a local online discriminative algorithms that can quickly adapt to temporal changes. In the same year, Hossian et al. [26] surveyed several important research works published in this area and proposed new technology to identify a person using multimodal physiology and behavioural biometrics. In 2013, Tilendra Shishir Sinha et al. [27] continued this research using human gait and human faces for the recognition of behavioural and physiological traits of the subject. This research adopted a vast amount of logical concepts of soft-computing techniques for the recognition of behavioural and physiological subject. Geometrical features are defined as functions belonging to one or more quality of objects that are capable of distinguishing objects from each other. Generally the human face image feature vector technique has been considered with geometric parameters of moment, shape, switching and texture features. These parameters are reasonably robust to the varying conditions and are capable enough of describing the quality of subjects. The two basic feature extraction techniques are: the geometric and holistic approaches, as suggested by J-H, Na et al. [28] The geometric approach, selects individual features and characteristics of the human face image, based on geometrical relational parameters. The holistic approach, selects complete features and characteristics of

the human face image, based on the calculations of the principal component analysis, Fisher's linear discriminant analysis, the independent component analysis, soft-computing techniques and the forward-backward dynamic programming method. As per the methods proposed by Mohammad et al., [29] and Heng et al. [30] both approaches have been applied because of some acceptable benefits to the research work with respect to fast recognition. The main advantage of using such methods is the calculations over features with reduced dimensionality by projections and original data onto the basic vectors. As a matter of fact, during the initial start of switching of the frame of the human-face image considering side-view of the face of the subject, the neuron fires and hence the human-face muscle activates. Stefanos et al. [31] analyzed further by considering frame by frame data of the human-face, in the year 2013. These frames of data have been fed as input for the computation of more additional parameters in steps: first the real-valued, second the neutral, third the normalized and finally the optimized and normalized parameter is computed.

From the above literature discussed so far it has been observed that very few researchers' have adopted DWT, soft-computing tools and their hybrid approaches, for the recognition of a human face from side-view (parallel to image plane). Also it has been found that in the last six decades, research in automatic face recognition has been intensively carried out worldwide in the field of biometrical studies, and has been summarized by the following changes:

- From template-matching approach to knowledge-based approach.

- From distance-based to likelihood-based methods.

- From maximum likelihood to discriminative approach (genetic algorithm method).

- From no commercial biometrical applications to commercial biometrical applications.

The literature has also evidenced that knowledge-based models are still playing a vital role in any biometrical research work. There continues to be a scope for automatic human-face recognition, using the innovative approach of DWT, soft-computing tools and their hybrid approaches. Thorough mathematical formulations have been done in Section 2.3 of this chapter, considering both human gait and human face images.

2.3. Mathematical formulation for biometrical authentication

Biometrical authentication on human gait and human face has been investigated using the progressive-regressive strategy and the implementation of DWT and the soft-computing technique. The soft-computing technique involves artificial neural network, genetic algorithm and the fuzzy set theory. For the computation of human gait and human face features, the firing concepts of artificial neural network have been incorporated. As per the literature and through experimental setup, it has been found that, a neuron is fired with a sigmoid function when the output is more than its threshold value. As a matter of fact, each neuron has input and output characteristics and performs a computation or function of the form, given in equation (1):

$$O_i = f(S_i) \text{ and } S_i = W^T X \tag{1}$$

where $X = (x_1, x_2, x_3, ..., x_m)$ is the vector input to the neuron, W is the weight matrix with w_{ij} being the weight (connection strength) of the connection between the jth element of the input vector and i^{th} neuron, W^T means the transpose of the weight matrix, the f(.) is an activation or nonlinear function (usually a sigmoid), O_i is the output of the ith neuron and S_i is the weighted sum of the inputs.
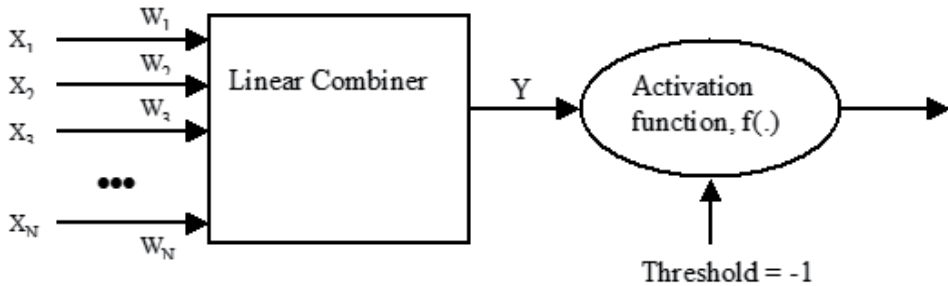
Figure 1. A simple artificial neuron.

The real power comes when a single neuron is combined into a multi-layer structure called artificial neural networks. The neuron has a set of nodes which connect it to the inputs, output or other neurons called synapses. A linear combiner is a function that takes all inputs and produces a single value. Let the input sequence be $\{X_1, X_2, ..., X_N\}$ and the synaptic weight be $\{W_1, W_2, W_3, ..., W_N\}$, so the output of the linear combiner, Y, yields to equation (2),

$$Y = \sum_{i=1}^{N} X_i W_i \tag{2}$$

An activation function will take any input from minus infinity to infinity and squeeze it into the range −1 to +1 or between 0 to 1 intervals. Usually an activation function is treated as a sigmoid function which relates as given in the below equation (3):

$$f(Y) = \frac{1}{1 + e^{-Y}} \tag{3}$$

The threshold defines the internal activity of the neuron, which is fixed to −1. In general, for the neuron to fire or activate, the sum should be greater than the threshold value. This has been analysed further by considering frame by frame data of human walking.

The human gait images have been fed as input for the computation of more additional parameters. The additional parameters are firstly the real-valued, secondly the neutral, thirdly the normalised and finally the optimised and normalised parameters.

Mathematically, this is discussed below:

Consider that 'Z' numbers of frames have been read. Each frame has been read as $FRAME_1$, $FRAME_2$, $FRAME_3$, $FRAME_4$, $FRAME_{Z-2}$, $FRAME_{Z-1}$, $FRAME_Z$. The whole process has been carried out adhering to the following guidelines:

- Read the first frame from left to right.

- Extract the step-length parameter, P_{1L}.

- Similarly read the first Frame from right to left.

- Similarly extract the step-length parameter, P_{1R}.

- Compute an average step-length parameter $F_{1avg} = (P_{1L} + P_{1R}) / 2$.

Where P_{1L} signifies step length of first frame with left-to-right direction and

- P_{1R} signifies step length of first frame with right-to-left direction and

- F_{1avg} signifies average step length of the first frame with both directions.

Repeat the above process for the next frames. Hence it yields to the average step-length measures as real-valued parameters, such as: $F_{2avg} = (P_{2L} + P_{2R}) / 2$, $F_{3avg} = (P_{3L} + P_{3R}) / 2$, $F_{4avg} = (P_{4L} + P_{4R}) / 2$, $F_{5avg} = (P_{5L} + P_{5R}) / 2$,..............,$F_{(Z-1)avg} = (P_{(Z-1)L} + P_{(Z-1)R}) / 2$,

$$F_{Zavg} = \left(P_{ZL} + P_{ZR}\right) / 2 \tag{4}$$

Next, to compute the neutral parameter, consider the 'even' and 'odd' frames separately. Let 'N_{odd}' and 'N_{even}' be the number of odd and even frames respectively. Hence, the neutral parameter yields to:

$$F_{Oddavg} = \left(F_{1avg} + F_{3avg} + \ldots\ldots + F_{(2Z-1)avg}\right) / N_{odd} \tag{5}$$

$$F_{Evenavg} = \left(F_{2avg} + F_{4avg} + \ldots\ldots + F_{(2Z)avg}\right) / N_{even} \tag{6}$$

The normalised parameters for each frame have been computed further. The solution yields for 'odd' frames:

$$F_{Norm1} = \frac{F_{1avg} - F_{Oddavg}}{F_{Oddavg}}, F_{Norm3} = \frac{F_{2avg} - F_{Oddavg}}{F_{Oddavg}}, F_{Norm5} = \frac{F_{3avg} - F_{Oddavg}}{F_{Oddavg}},$$

$$F_{Norm(2Z-1)} = \frac{F_{(2Z-1)avg} - F_{Oddavg}}{F_{Oddavg}} \tag{7}$$

Similarly for 'even' frames:

$$F_{Norm2} = \frac{F_{2avg} - F_{Evenavg}}{F_{Evenavg}}, F_{Norm4} = \frac{F_{4avg} - F_{Evenavg}}{F_{Evenavg}}, F_{Norm6} = \frac{F_{6avg} - F_{Evenavg}}{F_{Evenavg}},$$

$$F_{Norm2Z} = \frac{F_{(2Z-1)avg} - F_{Evenavg}}{F_{Evenavg}}$$

(8)

Further computing the average neutral and normalised parameters (NNP) for 'odd' and 'even' components, the solution yields to:

$$F_{NormOddavg} = \left(F_{Norm1} + F_{Norm3} + ... + F_{Norm(2Z-1)} \right) / N_{odd}$$

(9)

$$F_{NormEvenavg} = \left(F_{Norm2} + F_{Norm4} + ... + F_{Norm(2Z)} \right) / N_{even}$$

(10)

The next step is to compute the average NNP for each frame of the dataset, the solution yields to:

$$F_{NNP1} = \frac{F_{Norm1} - F_{NormOddavg}}{F_{NormOddavg}}, F_{NNP3} = \frac{F_{Norm3} - F_{NormOddavg}}{F_{NormOddavg}}$$

$$F_{NNP5} = \frac{F_{Norm5} - F_{NormOddavg}}{F_{NormOddavg}}, F_{NNP(2Z-1)} = \frac{F_{Norm1(2Z-1)} - F_{NormOddavg}}{F_{NormOddavg}}.$$

(11)

Similarly for 'even' frames:

$$F_{NNP2} = \frac{F_{Norm2} - F_{NormEvenavg}}{F_{NormEvenavg}}, F_{NNP4} = \frac{F_{Norm4} - F_{NormEvenavg}}{F_{NormEvenavg}}$$

$$F_{NNP6} = \frac{F_{6avg} - F_{Evenavg}}{F_{Evenavg}}, F_{NNP(2Z)} = \frac{F_{Norm1(2Z)} - F_{NormEvenavg}}{F_{NormEvenavg}}.$$

(12)

In general the dimensions of the feature vectors are of higher dimensions. In the present work, for better results during the classification and recognition process, the dimensions of these feature vectors have been reduced to lower dimensions, using the forward–backward dynamic programming method. To illustrate this method mathematically, the following initial conditions were set:

- Limit the area over which the search has to be performed.

- Searching must be performed using constraints for the computation of best dynamic characteristics of human gait.

Assume two distinguished human gait walking patterns, say $x(t_i)$ and $x(t_j)$ are defined, each with its own time base, t_i and t_j. Also assume that the beginning and end of the walking pattern are known, denoted as (t_{is}, t_{if}) and (t_{js}, t_{jf}) respectively. If both the patterns are sampled at the same rate, then both patterns begin 't' sample $i = j = 1$, that occurs without any loss of generality. Thus, the mapping function, $i = j$. (I / J), is linearly related. As the human gait patterns appear non-linear, so non-linear time warping functions are calculated, with several assumptions. Let the warping function, $w(k)$, be defined as a sequence of points: $c(1)$, $c(2)$,.....,$c(k)$, where $c(k) = (I(k), j(k))$ is the matching of the point $i(k)$ on the first time base and the point $j(k)$ on the second time base.

Further illustration has shown that humangait can be distinguished into five possible directions:

- Horizontally left to right movement and horizontally right to left movement (parallel to x-axis).

- Diagonally left to right and diagonally right to left (45 degree to x-axis).

- Diagonally right to left and diagonally left to right (135 degree to x-axis).

- Vertically (parallel to y-axis).

- Circularly clockwise direction and circularly anti-clockwise direction.

Setting the initial conditions let the search window be restricted to the limit:

$|i - j.(I / J)| \leq \gamma$, where γ is some constant.

From Figure 2, the warping, $w(k)$, only allows us to compare the appropriate parts of $x(t_i)$ with that of $x(t_j)$. Setting the monotonic and continuity conditions on the warping function, it restricts to the relations between four consecutive warping points, $c(k)$, $c(k-1)$ $c(k+1)$ and $c(kk)$, where kk signifies +/- or -/+.

Thus from Figure 2, there are eight ways to get to the point $c(i,j)$, which has been given in equations (13), (14), (15) and (16), below:

$$c(k) = c(i,j) \tag{13}$$

$$c(k\text{-}1) = \begin{cases} (i(k), j(k) - 1) \\ (i(k) - 1, j(k) - 1) \\ (i(k) - 1, j(k)) \end{cases} \tag{14}$$

$$c\left(k+1\right)=\begin{cases}(i(k),j(k)+1)\\(i(k)+1,j(k)+1)\\(i(k)+1,j(k))\end{cases} \tag{15}$$

$$c\left(kk\right)=\begin{cases}(i(k)-1,j(k)+1)\\(i(k)+1,j(k)-1)\end{cases} \tag{16}$$

And the boundary condition or circular movements yields to:

$$c\left(k\right)=\left(I,J\right) \tag{17}$$

By the boundary condition, the matching of the beginning and the end of the walking pattern and the tracing of the optimal route for normal walking have been analysed using the forward-backward dynamic programming method. To formulise this method for the tracing of the best match, the walking patterns have been represented at each point, by their feature vectors, $\beta_i(k)$ and $\beta_j(k)$, where $\beta_i(k)$ denotes the feature vector of the walking pattern $x(t_i)$ and $\beta_j(k)$ denotes the feature vector of the walking pattern $x(t_j)$. The distance between the two feature vectors is defined by:

$$d\left(c\left(k\right)\right)=d\left(i\left(k\right),j\left(k\right)\right)=\left|\beta_i(k) \ - \ \beta_j(k)\right| \tag{18}$$

The warping function is then assessed, so that the performance index $D(x(t_i),x(t_j))$ gets minimised. The performance index is the normalised average weighted distance, which has been related as:

$$D\left(x\left(t_i\right),x\left(t_j\right)\right)=\underset{w}{Min}\left[\frac{\sum_{k=1}^{k}d(c(k))\rho(k)}{\sum_{k=1}^{k}\rho(k)}\right] \tag{19}$$

where $\rho(k)$ are the weights, that yields to $I + J$, thus the equation (19) results to:

$$D\left(x\left(t_i\right),x\left(t_j\right)\right)=\frac{1}{I+J}\underset{w}{Min}\left[\sum_{k=1}^{k}d(c(k))\rho(k)\right] \tag{20}$$

On substituting the values of equations (13), (14), (15) and (16) in equation (20), each point in the search window has been attached with information for an optimal match up to its destination point (I, J). This approach to searching is said to be a forward technique of dynamic programming. After scanning is terminated, the construction of an optimal match is carried

out by going backward from the (I,J) to (0,0) or (1,1) point. This approach is said to be a backward technique of dynamic programming and the reversal process is a forward technique of dynamic programming. The combination of this two-way searching technique results in a forward-backward dynamic programming searching method. For an optimal solution, a minimum number of divergence values must be found. Thus, to compute the divergence values for an optimal solution, let the probability of getting a feature vector, β, given that it belongs to some class w_i, yields, $p(β/w_i)$, similarly for the class w_j, yields $p(β/w_j)$. The sum of the average logarithmic ratio between these two conditional probabilities yields information concerning the separability between the two classes and shows that there is no loss to the concept. This gives the divergence values of the features. Thus the mathematical formulation yields:

$$D_{i,j} = (\mu_i - \mu_j)(\mu_i - \mu_j)^T \Sigma^{-1} \tag{21}$$

where $\mu = \mu_i = \mu_j$ means the expectations and Σ mean the covariance.

From the equation (21) divergence values have been calculated up to 19 feature vectors.

The mathematical analysis for the detection of behavioural trait through human gait image has been formulated using two features: step length and walking speed.

Let the source be 'S' and the destination be 'D'. Also assume that normally this distance is to achieve in 'T' steps. So 'T' frames or samples of images are required. Considering the first frame, with left foot (F_L) at the back and right foot (F_R) at the front, the coordinates with (x,y) for the first frame, such that $F_L(x_1,y_1)$ and $F_R(x_2,y_2)$. Thus applying Manhattan distance measures, the step length has been computed and it yields to:

$$|step-length| = |x_2 - x_1| + |y_2 - y_1| \tag{22}$$

Normally, T_{act} steps are required to achieve the destination. From equation (22), T_1 has to be calculated for the first frame. Similarly, for 'nth' frame, T_n has to be calculated. Thus the total steps, calculated are:

$$T_{calc} = T_1 + T_2 + T_3 + ... + T_n \tag{23}$$

Thus walking speed or walking rate has been calculated and it yields to:

$$walking-speed = \begin{cases} norm & ,if \quad T_{act} = T_{calc} \\ fast & ,if \quad T_{act} < T_{calc} \\ slow & ,if \quad T_{act} > T_{calc} \end{cases} \tag{24}$$

Two measures, one of accuracy and the other of precision, have been derived to access the performance of the overall system, which has been formulated as:

$$accuracy = \frac{Correctly\,\mathrm{Re}\,cognized\quad feature}{Total\,number\,of\,\,features}$$
(25)

$$precision = \frac{TPD}{TPD+FPD}$$
(26)

where TPD = true positive detection and FPD = false positive detection.

Further analysis has been carried out for the classification of behavioural traits with two target classes (normal and abnormal). It has been further illustrated that the corpus developed in the present work has various states, each of which corresponds to a segmental feature vector. In one state, the segmental feature vector is characterised by nineteen parameters. Considering only three parameters of the step length: distance, mean, and standard deviation, the model yields to the equation :

$$AHGM_1 = \{D_{s1}, \mu_{s1}, \sigma_{s1}\}$$
(27)

where $AHGM_1$ means an artificial human gait model of the first feature vector, D_{s1} means the distance, μ_{s1} means the mean and σ_{s1} means the standard deviation based on step length. Let w_{norm} and w_{abnorm} be the two target classes representing 'normal behaviour' and 'abnormal behaviour' respectively. The clusters of features have been estimated by taking the probability distribution of these features. This has been achieved by employing Bayes' decision theorem. Let $P(w_i)$ be the probabilities of the classes, such that: i = 1,2,....M also let $p(\beta/w_i)$ be the conditional probability density. Assume a test human gait image represented by the features, β. So, the conditional probability $p(w_j/\beta)$, which belongs to j^{th} class, is given by Bayes' rule as:

$$P\left(w_j/\beta\right) = \frac{p(\beta/w_j)P(w_j)}{p(\beta)}$$
(28)

So, for the class j = 1 to 2 the probability density function $p(\beta)$, yields:

$$P\left(\beta\right) = \sum_{j=1}^{2} p(\beta\,/\,w_j)P(w_j)$$
(29)

Equation (28) gives a posteriori probability in terms of a priori probability $P(w_j)$. Hence it is quite logical to classify the signal, β, as follows:

If $P(w_{positive}/\beta) > P(w_{negative}/\beta)$, then the decision yields $\beta \in w_{positive}$ meaning 'positive biometric authentication' else the decision yields $\beta \in w_{negative}$ meaning 'negative biometric authentication'. If $P(w_{positive}/\beta) = P(w_{negative}/\beta)$, then it remains undecided or there may be 50% chance of being right when making a decision. During this situation further analysis was conducted using the fuzzy c-means clustering technique.

Similarly, the relevant physiological traits have to be extracted from the frontal human face images and template matching has to be employed for the recognition of behavioural traits. Little work has been completed in the area of human face recognition by extracting features from the side-view of the human face. When frontal images are tested for recognition with minimum orientation of the face or the image boundaries, the performance of the recognition system degrades. A path between pixels 'pix$_1$' and 'pix$_n$' is a sequence of pixels pix$_1$, pix$_2$, pix$_3$,....,pix$_{n-1}$,pix$_n$, such that pix$_k$ is adjacent to p_{k+1}, for $1 \le k < n$. Thus a connected component has to be obtained from the path, defined from a set of pixels, which in return depends upon the adjacent position of the pixel in that path. In order to compute the orientation using the reducing strategy, the phase angle must initially be calculated for an original image.

Let I_k be the side-view of an image with the orientation 'k'. If k = 90, then I_{90} is the image with an actual side-view. If the real and imaginary component of this oriented image is R_k and A_k. For k = 90 degree orientation:

$$\Rightarrow |I_k| = [R_k^2 + A_k^2]^{1/2} \tag{30}$$

For k = 90 ^{0}, orientation:

$$\Rightarrow |I_{90}| = [R_{90}^2 + A_{90}^2]^{1/2} \tag{31}$$

Thus the phase angle of an image with k = 90 orientations is:

$$\phi_k = \tan^{-1}\left[\frac{A_k}{R_k}\right] \tag{32}$$

If k = k-5, (applying the reducing strategy), equation (32) yields:

$$\phi_{k-5} \tan^{-1}\left[\frac{A_{k-5}}{R_{k-5}}\right] \tag{33}$$

There will be a lot of variety in the output between the equations (32) and (33). Hence these must be normalised, by imposing logarithmic to both equations:

$$\varphi_{normalize} = \log\left(1 + \left(\phi_k - \phi_{k-5}\right)\right) \tag{34}$$

Taking the covariance of (34), it yields perfect orientation between two side-views of the images, that is, I_{90} and $I\,85$:

$$I_{perfect-orientation} = \mathrm{Cov}\left(\phi_{normalize}\right) \tag{35}$$

The distances between the connected components have to be computed using the Euclidean distance method. A perfect matching has to be undertaken with best-fit measures using genetic algorithm. If the matching fails, then the orientation is to be reduced further by 5^0, that is k = k-5 and the process repeated till k = 45^0. The combination of this two-way searching technique results in the forward–backward dynamic programming–searching method. For optimal solution, a minimum number of divergence values results. Thus, to compute the divergence values for an optimal solution, let the probability of getting a feature vector, β, given that it belongs to some class w_i, yields: $p(\beta/w_i)$, similarly for the class w_j, yields: $p(\beta/w_j)$. The sum of the average logarithmic ratio between the two conditional probabilities, results in information concerning the separability between the two classes. It has also been discovered that there is no loss to the concept. This gives the divergence values of the features. Thus the mathematical formulation yields:

$$D_{i,j} = (\mu_i - \mu_j)\,(\mu_i - \mu_j)^{\mathrm{T}}\Sigma^{-1} \tag{36}$$

where $\mu = \mu_i = \mu_j$ means the expectations and Σ mean the covariance.

From equation (18) divergence values have been calculated up to nineteen feature vectors. These divergence values have been categorised into basic metrics: *true positive (TP), true negative (TN), false positive (FP)* and *false negative (FN)*. These metric values are useful for further analysis. In the present work, five assessments have been analysed: the *false positive rate (FPR)*, the *false negative rate (FNR), sensitivity (SV), specificity (SC)* and *accuracy (AC)*. The assessment, *false positive rate (FPR)*, is the segmentation of the object on a test image resulting in incomplete correct data. Mathematically, it yields to:

$$FPR = \frac{FP}{FP+TN} \tag{37}$$

The assessment, *false negative rate (FNR)*, is the segmentation of the object of interest of a test image resulting in complete incorrect data.

Mathematically, it yields to:

$$FNR = \frac{FN}{FN+TP}$$

(38)

The *sensitivity (SV)* assessment involves positive values of the object of interest on the test image being proportioned properly and being recognised with full capacity.

Mathematically, it yields to:

$$Sensitivity = \frac{Number\ of\ true\ positives}{Number\ of\ true\ positives + Number\ of\ false\ negatives} \times 100$$

(39)

The *specificity (SC)* assessment involves negative values of the object of interest being proportioned properly and being recognised with full capacity.

Mathematical, it yields to:

$$Specificity = \frac{Number\ of\ true\ negatives}{Number\ of\ true\ negatives + Number\ of\ false\ positives} \times 100$$

(40)

The *accuracy (AC)* assessment involves the measured and weighted values of the object of interest being classified properly resulting in linearity.

Mathematically, it yields to:

$$Accuracy = \frac{TP+TN}{TP+FP+TN+FN} \times 100$$

(41)

3. Solution methodology for the progressive–regressive strategy

The investigation of biometrical authentication on human gait and human face has been undertaken using the progressive-regressive strategy, implementing wavelet transform and soft-computing techniques. Initially, the analysis was carried out using wavelet transform. Hence soft-computing techniques like artificial neural network, genetic algorithm and fuzzy set theory were applied. Here in this chapter, the solution methodology for biometrical authentication is carried out based on the progressive–regressive strategy. The algorithms for the formation of corpus (for both human gait and human face), the progressive strategy, the regressive strategy and for the final authentication of biometrics are given below.

a.   **Algorithm for the formation of corpus using human face images:**

   1.   Read the front-view of human face image and convert it into a grayscale image.

2. Perform filtering for the removal of noise from the image and select a region of interest and also an object of interest.

3. Perform morphological image processing for the thinning and thickening of the objects.

4. Crop the image and extract features along with relevant parameters.

5. Employ statistical methods of computing like cross-correlation and auto-correlation with deviation of neighboring pixels using 4-pair and 8-pair concepts of pixel pairing.

6. Employ the fuzzy c-means clustering method for the computation of normal behaviour patterns. Hence compute the mean of the clusters.

7. Plot the results and store the extracted parameters in the form of corpus as a trained data set.

b. **Algorithm for the progressive strategy for biometrical authentication:**

1. Read the side-view of the human face image (test image) and convert into a grayscale image.

2. Initialise a progressive-switching angle, say theta_pro = zero.

3. Perform filtering for the removal of noise from the image and select a region of interest and also an object of interest.

4. Perform morphological image processing for the thinning and thickening of the objects.

5. Crop the image and extract features along with relevant parameters

6. Employ statistical methods of computing like cross-correlation and auto-correlation with deviation of neighboring pixels using 4-pair and 8-pair concepts of pixel pairing.

7. Employ the fuzzy c-means clustering method for the computation of behavioural patterns. Hence compute the mean of the clusters.

8. Compute the distance measure of the extracted features of the test image and the parameters that are stored in the corpus (formed through trained image).

9. Compare the patterns for the best fit using the forward-backward dynamic programming of artificial neural network and validate the whole process using genetic algorithm. If the best fit testing fails, then increment the progressive switching angle, theta_pro by five degrees and repeat Step 3. For fast processing increment by ten degrees.

10. Perform classification and characterisation using the support vector machine and hence a decision is made for recognition.

11. Compute the divergence values of metrics. Hence plot the results.

c.   Algorithm for the regressive strategy for biometrical authentication:

1. Read the side-view of the human face image (test image) and convert into a grayscale image.

2. Initialise a regressive-switching angle, say theta_reg = 90.

3. Perform filtering for the removal of noise from the image and select a region of interest and also an object of interest.

4. Perform morphological image processing for the thinning and thickening of the objects.

5. Crop the image and extract features along with relevant parameters.

6. Employ statistical methods of computing, such as cross-correlation and auto-correlation with deviation of neighboring pixels using 4-pair and 8-pair concepts of pixel pairing.

7. Employ the fuzzy c-means clustering method for the computation of behavioural patterns. Hence compute the mean of the clusters.

8. Compute the distance measure of the extracted features of the test image and the parameters that are stored in the corpus (formed through trained image).

9. Compare the patterns for the best fit using forward-backward dynamic programming of artificial neural network and validate the whole process using genetic algorithm. If the best fit testing fails, then increment the regressive-switching angle, theta_reg by five degrees and repeat Step 3. For fast processing decrement by ten degrees.

10. Perform classification and characterisation using a support vector machine and hence a decision is made for recognition.

11. Compute the divergence values of metrics. Hence plot the results.

d.   Algorithm for the validation of biometric authentication:

1. Read the original image, convert the RGB image into a grayscale image.

2. Perform filtering for the removal of noise from the grayscale image.

3. Employ morphological components for obtaining the thinning and thickening image.

4. Crop the image after the extraction of features and relevant parameters.

5. Employ Radon transform normalisation technique for computing muscle activation.

6. Set the angle value for the parallel projection of data, say theta1, theta2, theta3 and theta4.

7. Set four counter values for parallel projections as 12, 18, 36 and 90.

8. Employ the inverse Radon transform method for the regeneration of cropped images with parallel projections.

9. Select the best-fit parameters for the matching, using the forward backward dynamic–programming method.

10. Validate the above process using genetic algorithm.

11. Employ classification process using Bayes' theorem. If the classification value is 50% then employ fuzzy c-means clustering technique and check for the biometric code using Unidirectional Temporary Associative Memory (UTAM) technique of artificial neural network.

12. Employ the decision making process and finally plot the results.

4. Experimental results and discussions of case studies

First a human gait image is captured through eight digital cameras placed at a known fixed distance and fed as input for the investigation. The image is then enhanced and the loss-less compression technique, discrete cosine transform, is applied for the removal of distortions. Further it is segmented for contour detection and the relevant physiological features are extracted. All the features of the human gait image are stored in a corpus called the automatic human gait model. Relevant biometrical features with covariant mode (wearing no footwear) are extracted in the initial investigation. The relevant physiological feature, that is, step length and knee-to-ankle distance are also extracted.

After the extraction of relevant features, a limited number of parameters are utilized for the formation of a corpus. For this the Radon transform method and its inverse mechanism are applied and the relevant output of the algorithm is obtained which is shown in Figure 2, Figure 3 and Figure 4.

From Figure 2 and Figure 3, it is observed that the projection at 90 degrees has a wider profile than at a 0 degree projection. This means the energy and intensity value of muscle activation and contraction appears at a maximum when the angle for parallel projection of extracted data is at 90 degrees. The behavioural pattern matching of test datasets stored in a corpus called automatic human gait model (AHGM) for one subject is shown in Figure 4.

From Figure 4, it can be observed that three traits or moods of behaviour are analysed: over act, normal act and under act. The behaviour is normal, when there is no presence of perturbations in the behavioural characteristic curve. When a large number of perturbations is available in the behavioural characteristic curve, then it is under act behaviour. When a smaller number of perturbations is available in the behavioural characteristic curve; then it is under over act behaviour. This is further illustrated for both trained datasets and tests datasets and is shown in Figure 5.

This is also illustrated for both trained and test datasets, considering two different subjects shown in Figure 6.

This is also illustrated for both trained and test datasets, considering both the frames of walking cycle, that is odd and even cycle, which is shown in Figure 7.
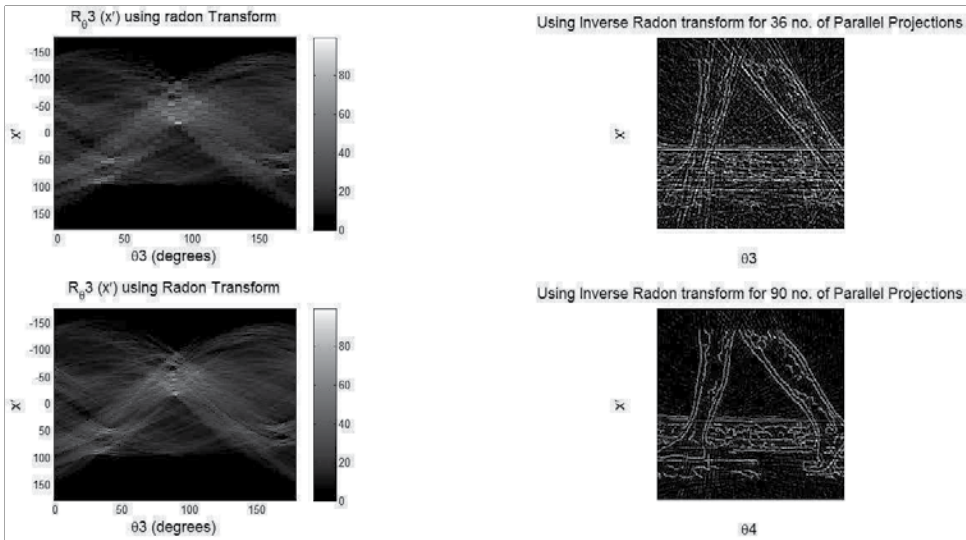
Figure 2. Muscle activation and contraction with projection count 36 and 90.
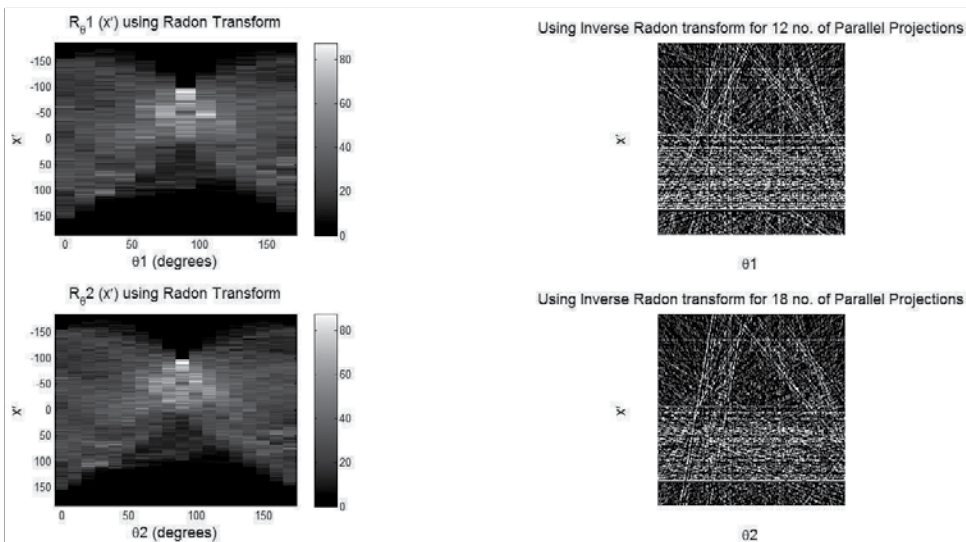
Figure 3. Muscle activation and contraction with projection count 12 and 18.

The clusters of features for the detection of the behavioural pattern or trait of human gait is plotted using fuzzy c-means clustering method, and the result is shown in Figure 8.

A boundary is formed, as shown in Figure 9, for the detection of gait code using UTAM technique of artificial neural network.

The overall behavioural pattern for trained and test datasets is shown in Figure 10.
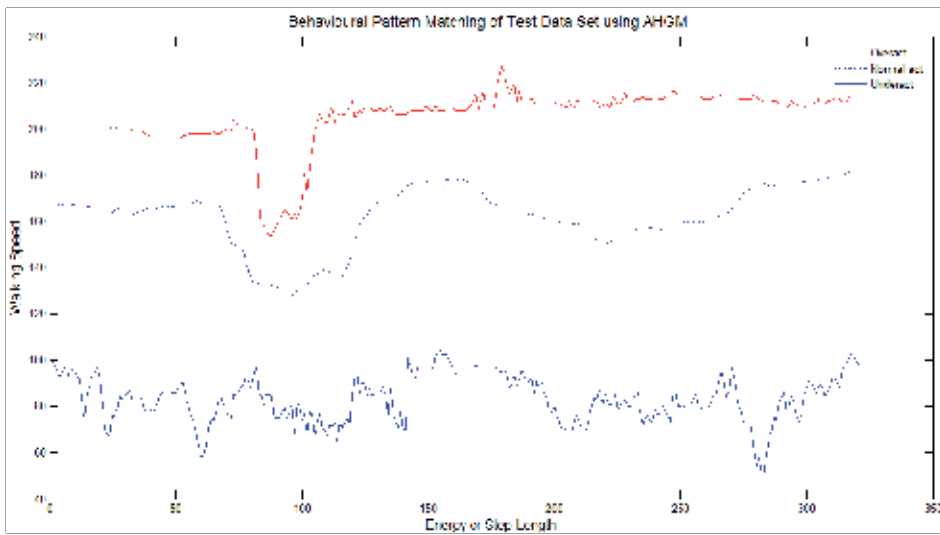
Figure 4. Behaviour pattern matching of test data set using AHGM of a subject gait (ten- second walk) with overact, normal act and underact moods.
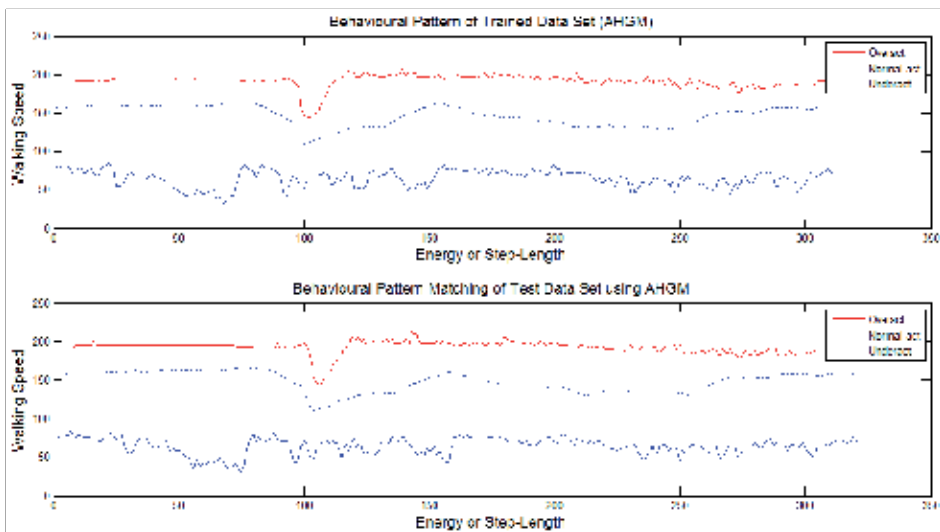
Figure 5. Behavioural pattern matching of the same subject gait (one-second walk) with over act, normal act and under act moods.

Similarly, for human face images, an observation is made for different distance measures. The distance measures along with the number of wrinkles or edges, texture of the human face and the normal behavioural pattern are calculated and is depicted in Table 1.

From Table 1 it is observed that the number of wrinkles or edges (NOW) ranges between 2 and 3. These values are extracted for male and female subjects whose age lies between 35 to
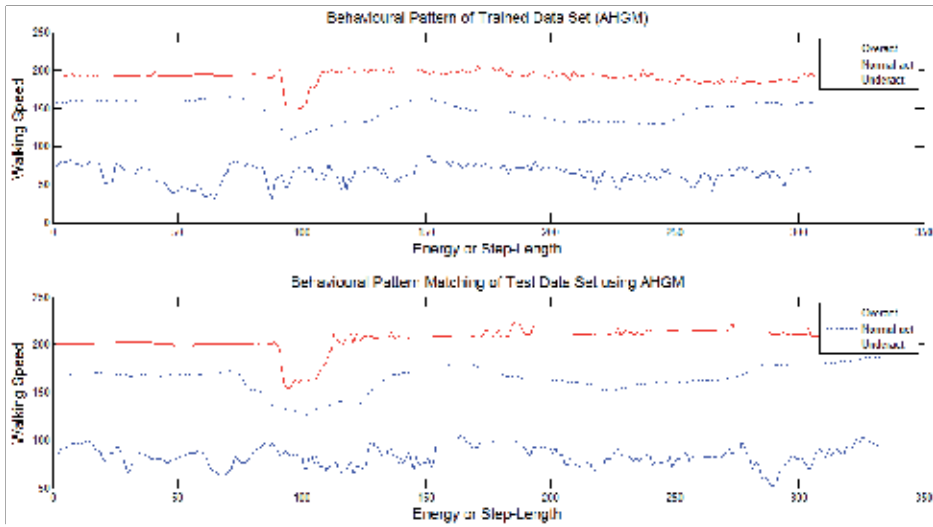
Figure 6. Behavioural pattern matching of two different subjects' gait (one-second walk) with over act, normal act and under act moods.
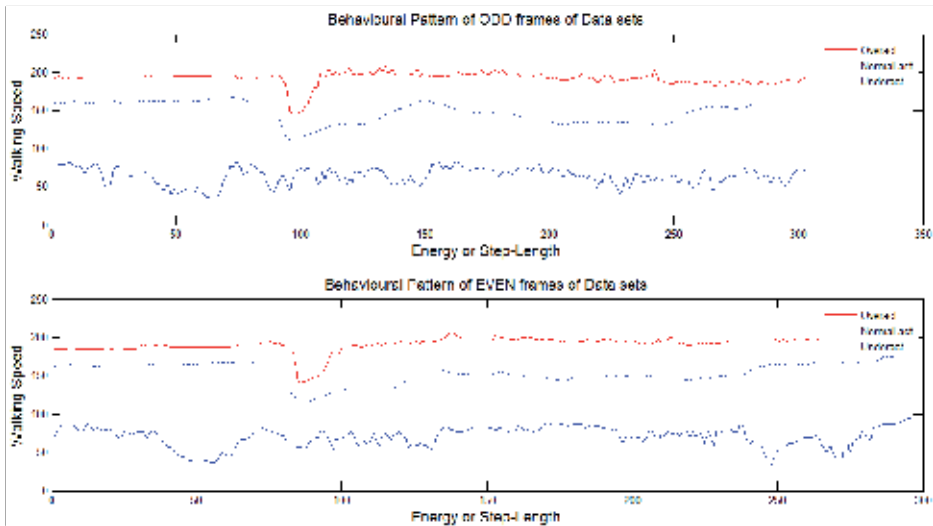
Figure 7. Behavioural pattern of odd and even frames of the same female subject gait (ten-second walk) with over act, normal act and under act moods.

50. The method that is applied, for the extraction of wrinkles or edges is the morphological components of digital image processing through Canny and Sobel properties. Similarly, the values of the texture of the human face is calculated as a unity. A texture is calculated using statistical methods of computation through cross-correleation and auto-correlation. Also the deviation of neighbouring pixels for texture analysis are also done using 4-pair and 8-pair computations of neighbouring pixels. The final conclusion on the texture calculation is made
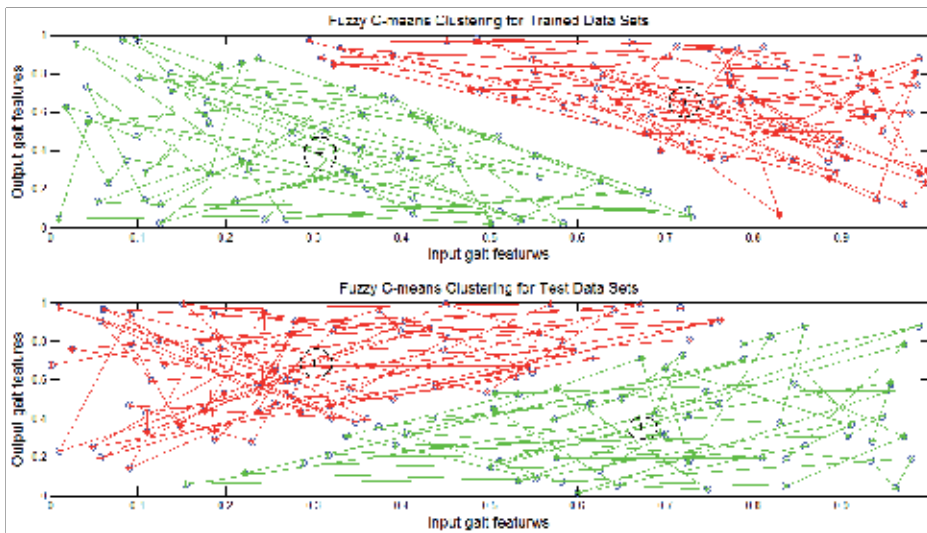
Figure 8. Clusters of features for the detection of the behavioural pattern using fuzzy c-means algorithm of a subject gait (ten-second walk).
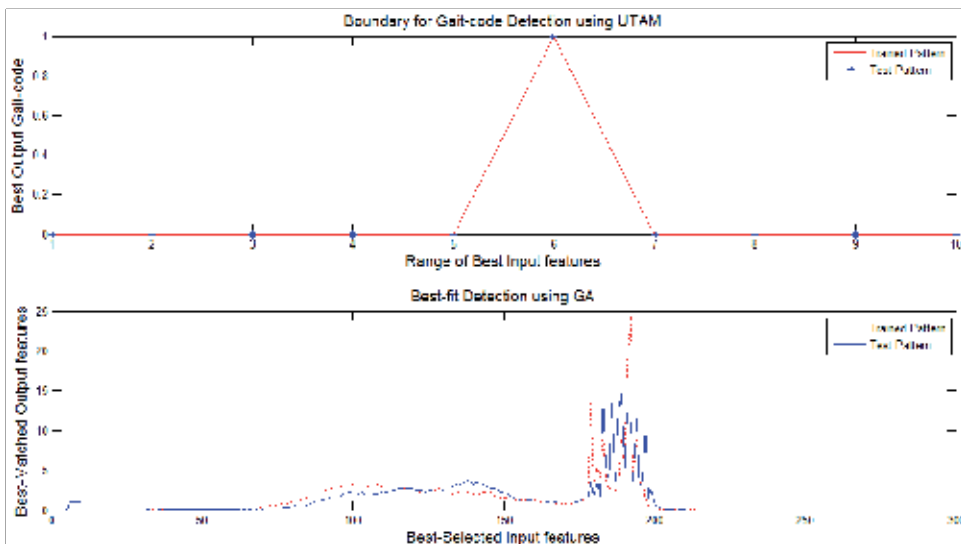
Figure 9. Boundary for gait code detection using UTAM and best fit detection using genetic algorithm of a subject gait (ten-second walk).

using the forward backward dynamic–programming method of soft-computing techniques. Further from Table 1 it is observed that the normal behavioural pattern (NBP) ranges from 10 to 15. These values are extracted using the fuzzy c-means clustering method with a mean value of the clusters for the normal behavioural pattern. The graphical representation of the parameters extracted from the frontal part of the human face image is shown in Figure 11.
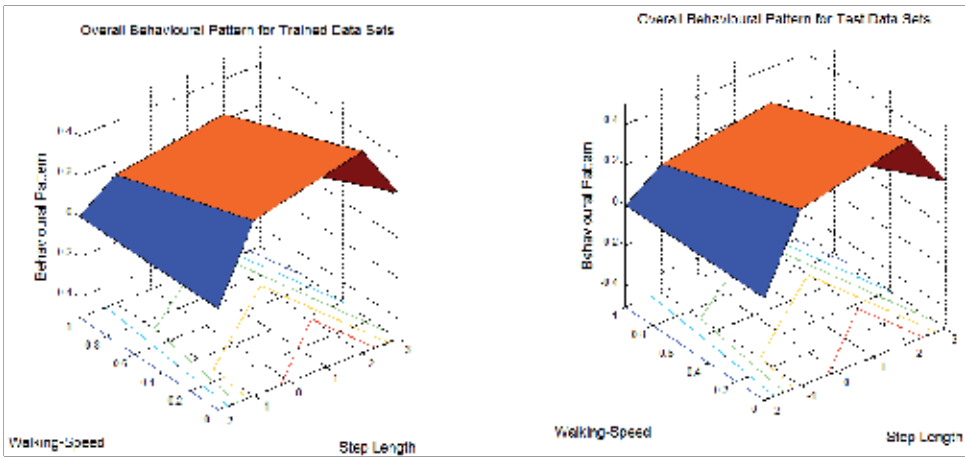
Figure 10. Overall behavioural pattern of a subject gait (ten-second walk) for both trained and test datasets.

Data source	FHW	ELD	LCD	ECD	END	NOW	TOF	NBP
Img1	40.26	50.23	6.07	56.30	46.96	2.00	1.00	10.00
Img2	40.23	50.26	6.05	56.31	46.95	3.00	1.00	11.00
Img3	40.05	50.29	6.00	56.29	46.98	2.00	1.00	10.50
Img4	40.15	50.19	6.06	56.25	46.99	2.00	1.00	12.00
Img5	40.28	50.18	6.10	56.28	47.02	2.00	1.00	12.05
Img6	40.27	50.16	6.09	56.25	47.01	3.00	1.00	13.50
Img7	40.24	50.21	6.08	56.29	47.03	2.00	1.00	12.50
Img8	40.12	50.22	6.01	56.23	47.04	2.00	1.00	13.60
Img9	40.09	50.27	6.04	56.31	46.94	2.00	1.00	12.06
Img10	40.19	50.09	6.03	56.12	46.89	3.00	1.00	13.75

Table 1. Distance measures of parameters and features of the human face of ten subjects.

For recognition of the human face, the side-view of the image is considered as a test data sample. Initiallly, a side-view of the human face which is parallel to the x-axis with zero degree orientation is fed as a test data sample. Hence preprocessing techniques of digital image processing are applied and a result is obtained. The techniques applied are: the loss-less compression technique, DWT for obtaining detail and coarser components of the switching pattern, statistical methods of computation for the computation of the mean covariance of transformed vectors and the principal component analysis for the computation of eigen vectors and eigen values. The results obtained from the human face test image with a side-view is shown in Figure 12, Figure 13 and Figure 14, along with brief discussions and observations.
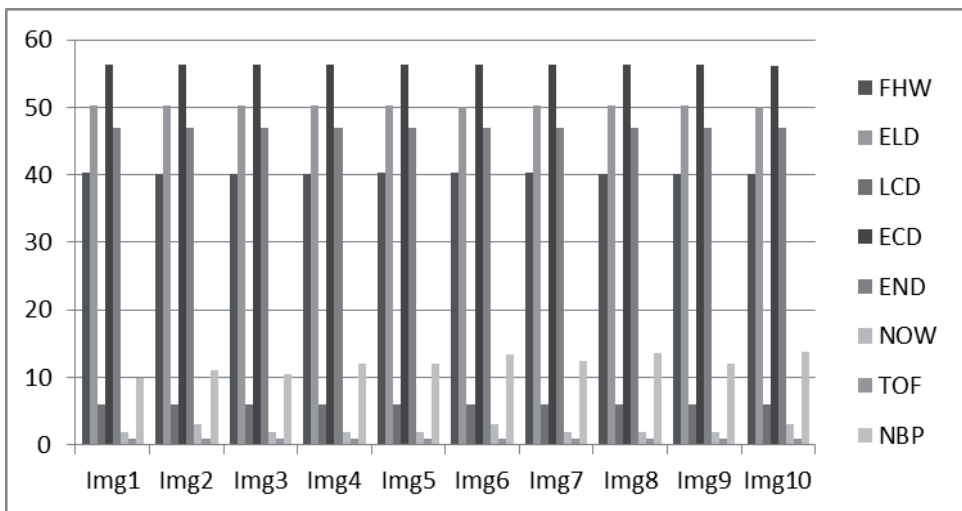
Figure 11. Graphical representation of the parameters extracted from the human face image.
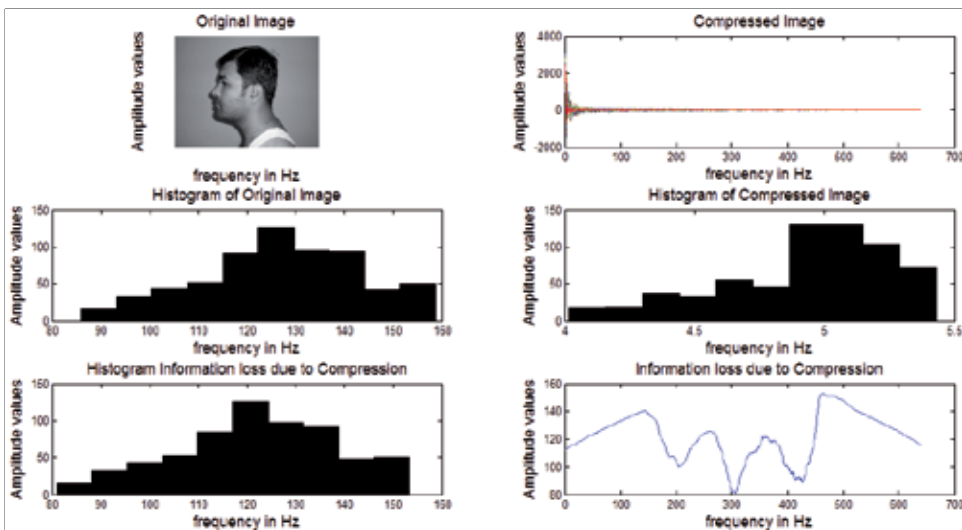
Figure 12. The loss-less compression of a human face test image captured from a side-view.

After performing the loss-less compression on the test image, further calculations are carried out such as coarser and detail components of the switching pattern using DWT and the results are plotted in Figure 13.

Figure 13 shows the calculation of detail and coarser components, which are then utilised for further calculation of odd and even components of the human face image. In the present work, this is achieved by employing the lifting and inverse-lifting schemes of DWT. Further analysis and outcomes are plotted in Figure 14.
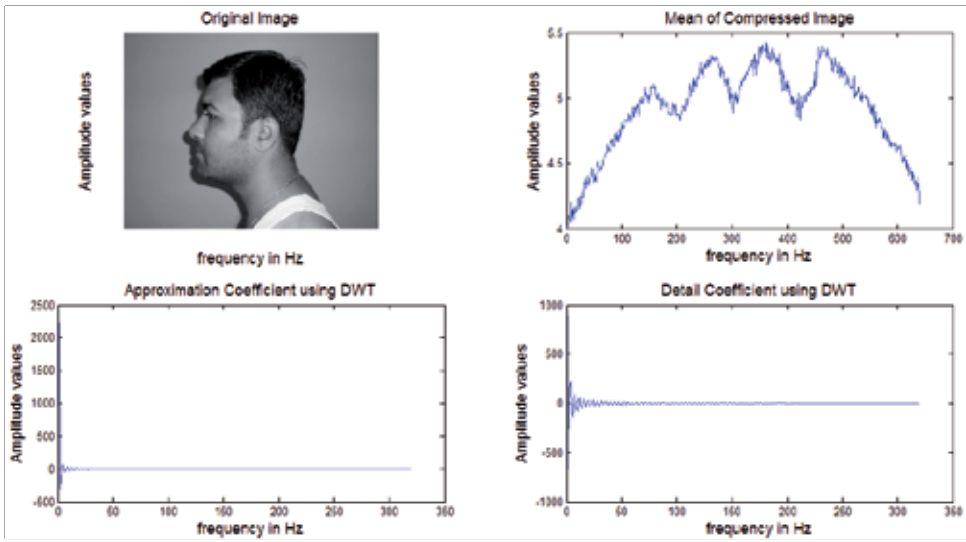
Figure 13. DWT of the test image captured from the side-view of the human face.
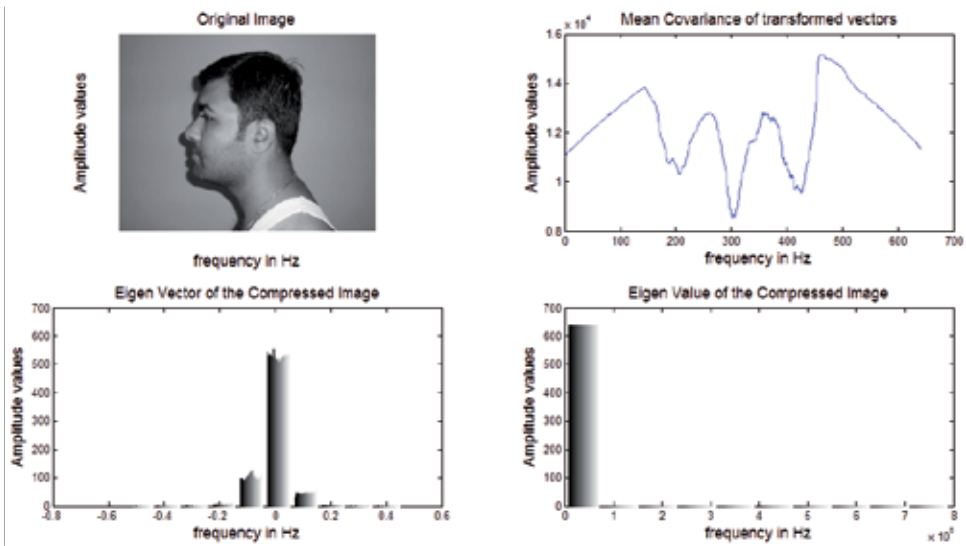
Figure 14. Principal component analysis of the test image captured from the side-view of a human face.

From Figure 14, it is observed that transformed eigen vectors and their corresponding eigen value are extracted for analysing the switching pattern. The switching angle is gradually increased. Initial analysis is carried out on five degree progressive displacement. Later the same is done with a ten degree increment. The comparison of the progressive switching patterns for odd multiples of frames of human face images is computed and shown in Figure 15.
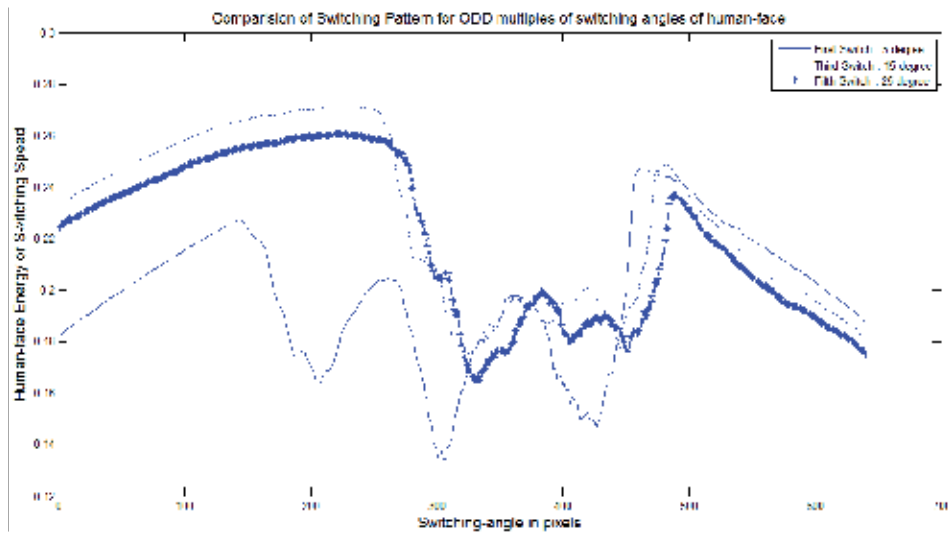
Figure 15. Comparison of the switching pattern for odd frames of the test image.
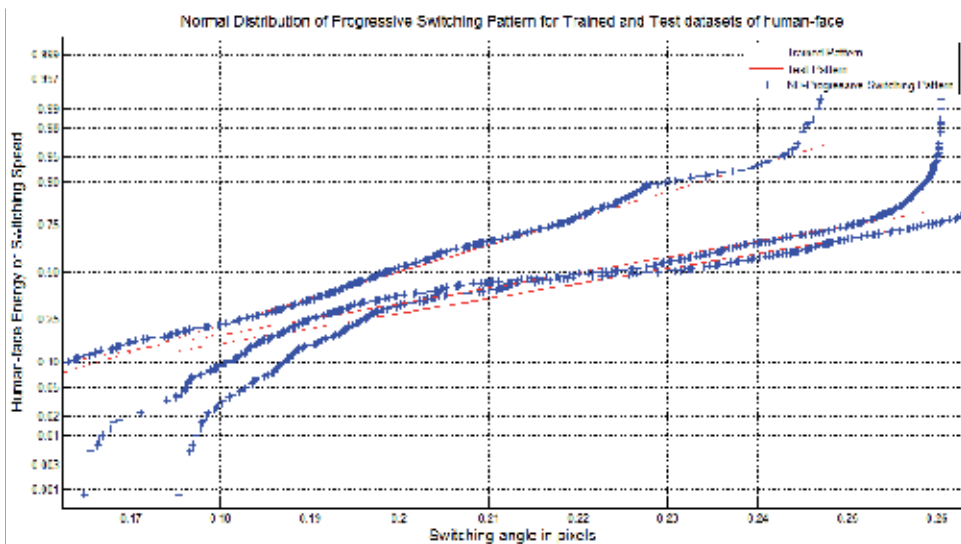
Figure 16. Normal distribution of progressive switching pattern for odd frames of the test image.

From Figure 15 it is observed that for the first frame, with a five degree orientation, the extracted parameters are matched. However the fitness test failed. Hence further analysis is carried out for availing th the best-fitness test. This is achieved using progressive switching of the human face with a ten degree displacement. Finally, it is found that most parameters follow the normal pattern of the trained data set stored in a corpus. Hence the best fit measures are carried out and further analysis for the classification and recognition is performed, using the

genetic algorithm of soft-computing techniques. Further, the normal and cumulative distribution of progressive switching patterns of the test image is shown in Figure 16 and Figure 17.
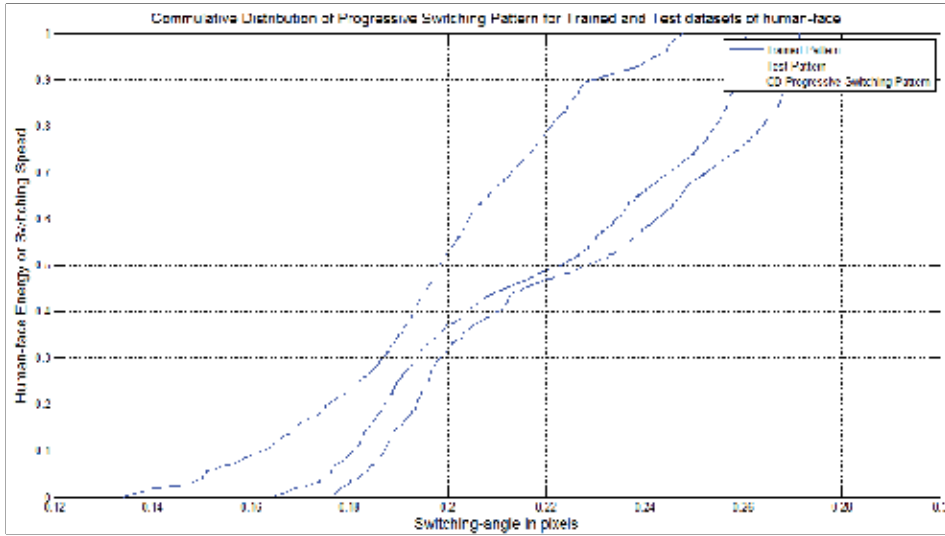
Figure 17. Cumulative distribution of progressive switching pattern for odd frames of the test image.

The classification and characterisation process of the progressive switching pattern of the human face test image captured from the side-view is carried out using the support vector machine of artificial neural network. The results found are very remarkable and the plotting is shown in Figure 18.
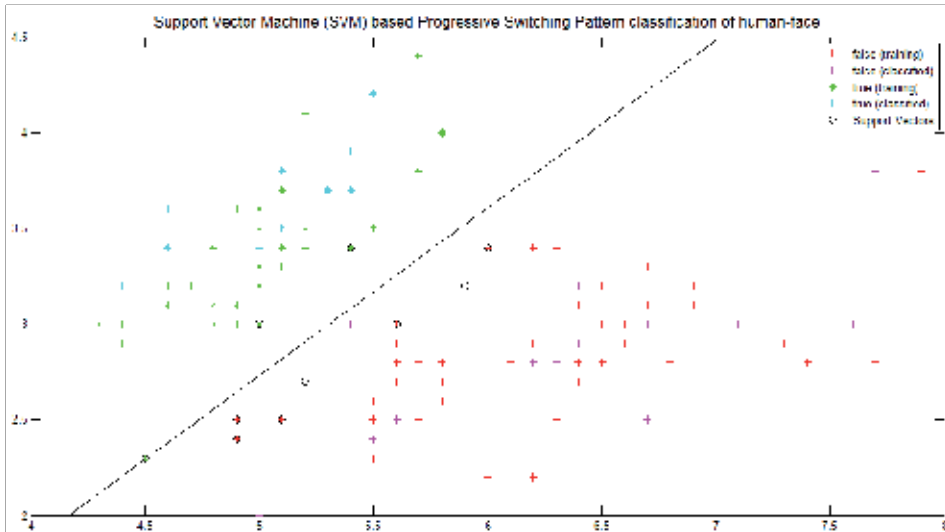
Figure 18. Classification of progressive switching pattern using the support vector machine of artificial neural network.

The different divergence value of metrics for the test image captured from the side-view of the human face is shown in Table 2 and the plot in Figure 19.

Data source	FPR	FNR	Sensitivity (%)	Specificity (%)	Accuracy (%)
Img1	5.9411	4.9112	95.0888	94.0589	94.1757
Img2	9.5504	30.0836	69.9164	90.4496	88.2385
Img3	9.4283	32.6887	67.3113	90.5717	87.9105
Img4	7.1306	11.9463	88.0537	92.8694	92.3386
Img5	9.9959	33.171	66.829	90.0041	91.5351
Img6	9.0173	37.9402	62.0598	90.9827	89.1475
Img7	8.5589	77.2401	22.7599	91.4411	85.2078
Img8	10.9437	78.8765	21.1235	89.0563	94.9759
Img9	13.2179	80.6998	19.3002	86.7821	95.3528
Img10	12.5232	79.2356	18.2003	88.4252	93.9536

Table 2. Divergence values of metrics for the human face captured from the side-view of ten subjects.
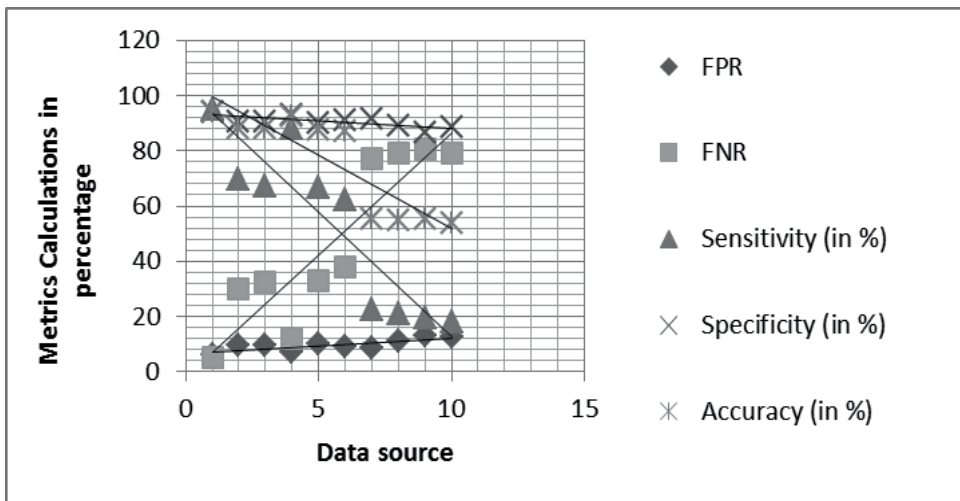
Figure 19. Graphical representation of divergence values of metrics of the test image of the human face, captured from the side-view for ten different subjects.

5. Conclusion and further scope

The results gained so far must be further analysed using the fan-beam projection method in order to obtain more accurate values required for biometric authentication through human gait and human face images. The volume of the corpus must also be increased and further analysis carried out with the developed algorithm. Statistical and high-end computing

measures must also be taken using known algorithms from the literature. The analysis will be also based on performance measures with an optimal number of parameters for the validation of biometric authentication.

Furthermore an appropriate amount of results has been obtained and analysis carried out with an acceptable value of recognition of human face captured from the side-view. Still there are scopes for carrying out the research work on the obtained results. The algorithm developed for the recognition of human face from the side-view must be analysed further with complexity under a worst-case condition. To achieve such goals, high-end computing measures have to be carried out using advanced mathematical formulations and known algorithms from the literature. The performance measures with an optimal number of parameters required for the recognition of the human face from the side-view must also be analysed.

Author details

Tilendra Shishir Sinha[1*], Raj Kumar Patra[2], Rohit Raja[2], Devanshu Chakravarty[2] and Ravi Prakash Dubey[3]

*Address all correspondence to: tssinha1968@gmail.com

1 School of Engineering and Information Technology, MATS University, Raipur, Chhattisgarh State, India

2 Computer Science and Engineering Department, Dr. C.V. Raman University, Bilaspur, Chhattisgarh State, India

3 Dr. C. V. Raman University, Bilaspur, Chhattisgarh State, India

References

[1] Boyd J. E., and Little J. J., *Biometric gait recognition*, Springer-Verlag Berlin Heidelberg, LNCS 3161, pp 19-42, 2005.

[2] Nixon M. S., Carter J. N., Cunado D., Huang P. S., and Stevenage S. V., *Automatic gait recognition*, Eds. Biometrics: personal identification in networked society, pp 231-250, 1999.

[3] Murray M. P., Drought A. B., and Kory R. C., *Walking patterns of normal men*, Journal of bone and joint surgery, vol. 46-A(2), pp 335-360, 1964

[4] Ben-Abdelkader C., Cutler R., and Davis L., *Gait recognition using image self-similarity*, EURASIP Journal on applied signal processing, vol. 4, pp 572-585, 2004.

[5]   Ben-Abdelkader C., Cutler R., and Davis L., *Person identification using automatic height and stride estimation*, In 16th International conference on pattern recognition, Quebec, Canada, pp 377-380, August, 2002.

[6]   Kale A., Cuntoor N., Yegnanarayana B., Rajagopalan A. N., and Chellappa R., *Gait analysis for human identification*, LNCS 2688, pp 706-714, 2003.

[7]   Huang P. S., Harris J. C., and Nixon M. S., *Comparing different template features for recognizing people by their gait*, In British machine vision conference, Southampton, UK, pp 639-648, September – October, 1998.

[8]   Cunado D., Nixon M. S., and Carter J. N., *Using gait as a biometric, via phase-weighted magnitude spectra*, In the proceedings of first international conference, AVBPA'97, Crans-Montana, Switzerland, pp 95-102, March, 1997.

[9]   Phillips P. J., Sarkar S., Robledo I., Grother P., and Bowyer K., *Baseline results for the challenge problem of human id using gait analysis*, In the proceedings of fifth IEEE international conference on face and gesture recognition, Washington DC, USA, pp 137-142, May, 2002.

[10] Phillips P. J., Sarkar S., Robledo I., Grother P., and Bowyer K., *The gait identification challenge problem: datasets and baseline algorithm*, In the sixteenth IEEE international conference on pattern recognition, Quebec, Canada, vol. 1, pp 10385-10388, August, 2002.

[11] Jack M. Wang, David J. Fleet and Aaron Hertzmann, *Gaussian process dynamical models for human motion*, IEEE transactions on pattern analysis and machine intelligence, vol. 30, no.2, pp 283-298, 2011.

[12] Sina Samangooei and Mark S. Nixon, *Performing content-based retrieval of humans using gait biometrics*, LNCS 5392, Springer-Verlag Berlin Heidelberg, pp. 105-120, 2008.

[13] Imed Bouchrika, Michaela Goffredo, John Carter and Mark S. Nixon, *On using gait in forensic biometrics*, Journal of forensic sciences, vol. 56, no. 4, pp 882-889, 2011.

[14] Sinha Tilendra Shishir, Patra Raj Kumar, and Raja Rohit, *A comprehensive analysis of human gait for abnormal foot recognition using neuro-genetic approach*, International Journal of tomography and statistics, vol. 16, no. w11, pp 56-73, 2011.

[15] Chen Wang, Junping Zhang, and Liang Wang, *Human identification using temporal information preserving gait template*, IEEE transactions on pattern analysis and machine intelligence, vol. 34, no. 11, 2012.

[16] Trunk M. and Pentland A. *Eigenfaces for recognition*, Journal of cognitive Neuroscience, vol. 3, no. 1, pp. 71-86, 1991.

[17] Kirby M. and Sirovich L. *Application of the Karhunen-Loeve procedure for the characterization of human face*, IEEE transactions on Pattern Analysis and Machine Intelligence, vol. 12, no. 1, pp.103- 108, 1990.

[18] Hu. Y., Jiang, D., Yan, S., Zhang, H., *Automatic 3D reconstruction for face recognition*, in the proceeding of the IEEE International Conference on automatic face and gesture recognition. pp. 843- 850, 2000.

[19] Lee, C.H., Park, S.W., Chang, W., Park, J.W: *Improving the performance of multi-class SVMs in the face recognition with nearest neighbour rule*, in the proceeding of the IEEE International Conference on Tools with Artificial Intelligence, pp. 411-415, 2003.

[20] Michal Valstar, Loannis Patras and Maja Pantic, *Facial action unit recognition using temporal templates*, in the proceeding of the IEEE International Workshop on Robot and Human Interactive Communication, Okayama Japan, September 20-22, 2004.

[21] Jolly D. Shah and S.H. Patil, *Biometric authentication based on detection and recognition of multiple face in image*, in the proceeding of IC-3, 2008.

[22] Richa Singh, Mayank Vasta Arun Ross and Afzel, *A mosaicing scheme for pose - invariant face recognition*, in IEEE Transactions on Systems, MAN and CYBERNETICS, vol. 37, no. 5, 2007.

[23] Edward Kao, Peter VanMaasdam, John Sheppard, *Image-based tackling with particle swarms and probabilistic data association*, in IEEE Swarn Intelligence Symposium, St. Louis MO USA, September 21-23, 2008.

[24] Xiaozheng Zhang, Yongsheng Gao, Maylor K. H. Leung *Recognizing rotated faces from frontal and side views: an approach toward effective use of mugshot databases*, in IEEE Transactions on Information Forensics and Security, vol. 3, no. 4, 2008.

[25] Li Cheng, Minglun Gong, Dale Schurmans and Terry Calli, *Real-time discriminative background subtraction*, in IEEE Transaction on image processing, vol. 20, no. 5, 2011.

[26] Hossain S.M.E and Chetty G. *Human identity verification by using physiology and behavioral biometric traits*, in the International Journal of Bioscience and Bioinformatics, vol. 1, no. 3, 2011.

[27] Tilendra Shishir Sinha, Devanshu Chakravarty, Raj Kumar Patra and Rohit Raja, *Modelling and simulation for the recognition of physiological and behavioral traits through human gait and face images*, published as a book chapter in a book entitled "Discrete Wavelet Transforms – a compendium of new approaches and recent applications", InTech Open, ISBN 978-953-51-0940-2, pp. 95-125, 2013, edited by Dr. Awad Kh. Al-Asmari. DOI:105772/52565.

[28] J.-H., Na, M.-S, Park, and J.-Y,Choi, *Pre-clustered principal component analysis for fast training of new face databases*, International conference control, automation system, pp. 1144-1149, 2007.

[29] Mohammad Said El-Bashir, *Face recognition using multi-classifier*, Applied sciences journal, vol. 6, no. 45, pp. 2235-2244, 2012.

[30] Heng Fui Liau and Dino Isa, *New illumination compensation method for face recognition*, International journal of computer and network security, vol. 2, no. 45, pp. 5-12, 2010.

[31] Stefanos Zafeiriou, Gary A. Atkinson, Mark F. Hansen, William A. P. Smith, Vasileios Argyriou, Maria Petrou, Melvyn L. Smith and Lyndon N. Smith, *Face recognition and verification using photometric stereo: the photo-face database and a comprehensive evaluation*, IEEE transactions on information forensics and security, vol. 8, no. 1, 2013.

Resolutıon Enhancement Based Image Compression Technique using Singular Value Decomposition and Wavelet Transforms

Gholamreza Anbarjafari, Pejman Rasti, Morteza Daneshmand and Cagri Ozcinar

Additional information is available at the end of the chapter

Abstract

In this chapter, we propose a new lossy image compression technique that uses singular value decomposition (SVD) and wavelet difference reduction (WDR) technique followed by resolution enhancement using discrete wavelet transform (DWT) and stationary wavelet transform (SWT). The input image is decomposed into four different frequency subbands by using DWT. The low-frequency sub-band is the being compressed by using DWR and in parallel the high-frequency subbands are being compressed by using SVD which reduces the rank by ignoring small singular values. The compression ratio is obtained by dividing the total number of bits required to represent the input image over the total bit numbers obtain by WDR and SVD. Reconstruction is carried out by using inverse of WDR to obtained low-frequency subband and reconstructing the high-frequency subbands by using matrix multiplications. The high-frequency subbands are being enhanced by incorporating the high-frequency subbands obtained by applying SWT on the reconstructed low-frequency subband. The reconstructed low-frequency subband and enhanced high-frequency subbands are being used to generate the reconstructed image by using inverse DWT. The visual and quantitative experimental results of the proposed image compression technique are shown and also compared with those of the WDR with arithmetic coding technique and JPEG2000. From the results of the comparison, the proposed image compression technique outperforms the WDR-AC and JPEG2000 techniques.

Keywords: Lossy Image compression, Singular Value Decomposition, Wavelet Difference Reduction, Stationary Wavelet Transform, Discrete Wavelet Transform, Image Super Resolution

1. Introduction

With the growing demand for multimedia applications, especially high-definition images, efficient storage and transmission of images have been issues of great concern [1, 2, 3, 4]. Image processing deals with the reduction of the amount of bits used to represent an image. Not only that but also resolution of an image plays an important role in many image processing applications, such as video resolution enhancement [5], feature extraction [6], and satellite image resolution enhancement [7]. In general, there are two types of super resolution approaches, multi-image super resolution and single image. Multiple-image super-resolution algorithms, like [8], [9], [10] to name a few, receive a couple of low-resolution images of the same scene as input and usually employ a registration algorithm to find the transformation between them. This transformation information is then used along with the estimated blurring parameters of the input low-resolution images, to combine them into a higher-scale framework to produce a super-resolved output image. For multiple-image super-resolution algorithms to work properly there should be subpixels displacements between input low-resolution images. Furthermore, these subpixels displacements should be estimated properly by the registration algorithm, which is usually a challenging task, especially when complicated motion of nonrigid objects, like human body, needs to be modeled. These algorithms are guaranteed to produce proper higher-resolution details; however, their improvement factors are usually limited by factors close to 2 [11].

Single-image super-resolution algorithms, like [12, 13, 14], to name a few, do not have the possibility of utilizing subpixel displacements, because they only have a single input. Instead, they employ a kind of training algorithm to learn the relationship between a set of high-resolution images and their low-resolution counterparts. This learned relationship is then used to predict the missing high-resolution details of the input low-resolution images. Depending on the relationship between the training low- and high-resolution images, these algorithms can produce high-resolution images that are far better than their inputs, by improvement factors that are much larger than 2 [15]. Hence, compression of an image and yet reconstructing the image with good resolution is important. Information theory is playing an important role in image compression. Information theory can be used in order to reduce the dimensionality of data such as histogram [16, 17]

There are two categories of image compression techniques, namely lossless and lossy image compression techniques [18, 19]. In lossless image compression, the original image can be perfectly recovered from the compressed image while in lossy compression the original image cannot be perfectively recovered from the compressed image because some information is lost as a result of compression. Lossless compression is used in applications with high requirements such as medical imaging. Lossy compression techniques are very popular because they offer higher compression ratio. The objective of image compression is to achieve as much compression as possible with little loss of information [20, 21].

Wavelets are also playing significant role in many image processing applications [12, 22, 23, 24]. The two-dimensional wavelet decomposition of an image is performed by applying the one-dimensional DWT along the rows of the image first, and then the results are decomposed

along the columns. This operation results in four decomposed subband images referred to Low-Low (LL), Low-High (LH), High-Low (HL), and High-High (HH). The frequency components of those subbands cover the full frequency spectrum of the original image. Figure 1 shows different subband images of Lena image where the top-left image is the LL subband and the bottom-right image is the HH subband.

Figure 1. LL, LH, HL, and HH subbands of Lena image obtained by using DWT.

In this research work, a new lossy compression technique which employs singular value decomposition (SVD) and wavelet difference reduction (WDR) is presented. SVD is a lossy image compression technique which can be regarded as a quantization process where it

reduces the physcovisual redundancies of the image [25, 26]. In order to enhance the resolution of the decompressed image, stationary wavelet transform (SWT) is used. WDR is one of the state-of-the-art techniques in image compression which uses wavelet transform. It is a lossy image compression technique which achieves compression by first taking the wavelet transform of the input image and then applying the difference reduction method on the transform values [27, 28, 29, 30].

Wavelet transform based techniques also play a significant role in many image processing applications, in particular in resolution enhancement, and recently, many novel resolution enhancement by using wavelet transforms have been proposed. Demirel and Anbarjafari [31] proposed an image resolution enhancement technique based on the input image and interpolation of the high-frequency subband images obtained by DWT. In their technique, an SWT technique is used in order to enhance the edges. Then, at the same time input image is decomposed into four frequency subbands image by using DWT. After that the input image, as well as the high-frequency subbands are interpolated. The high-frequency subbands of SWT are used to modify the estimated high-frequency subbands. Finally, inverse DWT (IDWT) is applied to combine all frequency subbands in order to generate a high-resolution image. Figure 2 shows the block diagram of the proposed method in [31].
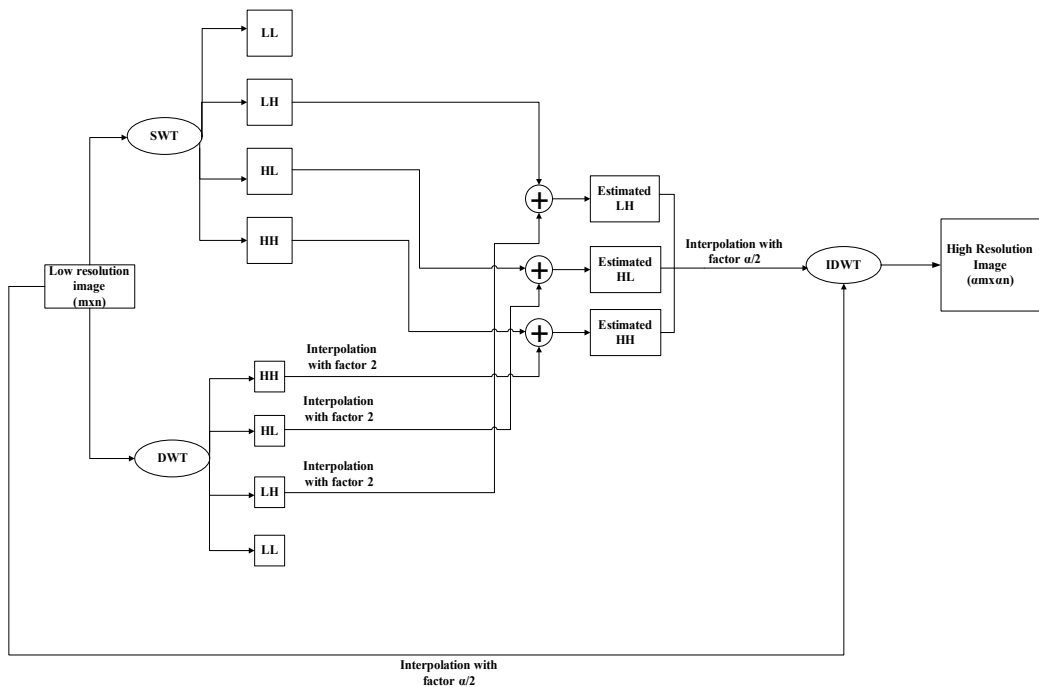
Figure 2. Block diagram of the proposed method in [31].

The authors in [32] proposed a learning-based super-resolution algorithm. In their proposed algorithm, a multi-resolution wavelet approach was adopted to perform the synthesis of local

high-frequency features. Two frequency subbands, LH and HL, were estimated based on wavelet frame in order to get a high-resolution image. The LH and HL frequency subbands were used to prepare their training sets. Then, they used the training set in order to estimate wavelet coefficients for both LH and HL frequency subbands. Finally, the IDWT was used in order to reconstruct a high-resolution image.

In [33], the authors used a complex wavelet-domain image resolution enhancement algorithm based on the estimation of wavelet coefficients. Their method uses a dual-tree complex wavelet transform (DT-CWT) in order to generate a high-resolution image. First, they estimate a set of wavelet coefficients from the DT-CWT decomposition of the rough estimation of the high-resolution image. Then, the inverse DT-CWT is used to combine the wavelet coefficients and the low-resolution input image in order to reconstruct a high-resolution image. Figure 3 shows the block diagram of the proposed method in [33].
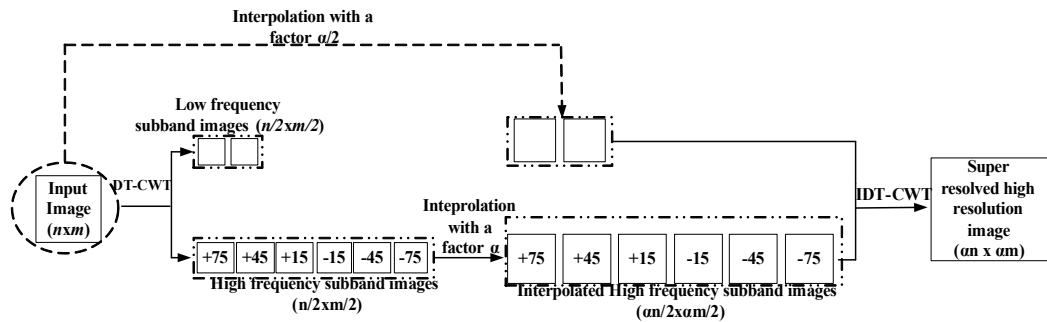
Figure 3. Block diagram of the proposed method in [33].

Patel and Joshi [34] proposed a new learning-based approach for super resolution using DWT. The novelty of their method lies in designing application-specific wavelet basis (filter coefficients). First the filter coefficients and learning the high-frequency details in the wavelet domain is used to initial estimate of super-resolution image. Then, they used a sparsely based regularization framework, in which image there was degradation. Finally, the super-resolution image is estimated by the initial super-resolution estimate and the estimated wavelet filter coefficients. Their algorithm has some advantages such as avoiding the use of registered images while learning the initial estimate, use of sparsity prior to preserving neighborhood dependencies in super-resolution image and use of estimated wavelet filter coefficients to represent an optimal point spread function to model image acquisition process. Figure 4 illustrates the block diagram of the proposed method in [34].

In [35], similar to the proposed method in [30], the authors used wavelet domain in order to generate super-resolution image from a single low-resolution image. They proposed an intermediate stage with the aim of estimating high-frequency subbands. The intermediate stage consists of an edge preservation procedure and mutual interpolation between the input low-resolution image and the HF subband images. Sparse mixing weights are calculated over blocks of coefficients in an image, which provides a sparse signal representation in the low-
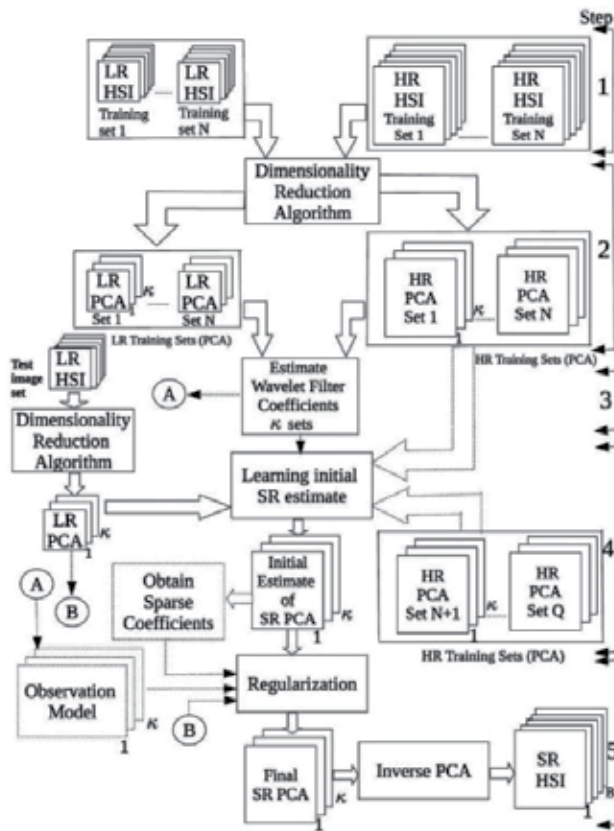
Figure 4. Block diagram of the proposed method in [34].

resolution image. Finally, they used IDWT to combine all frequency subbands in order to reconstruct a high-resolution image. The block diagram of their proposed method is shown in Fig. 5.

In [36], they proposed a learning-based approach for super-resolving an image captured at low spatial resolution. They used a low resolution and a database of high- and low-resolution images as inputs to the proposed method. First, they used DWT in order to obtain high-frequency details of database images. Then, an initial high-resolution image was decimated by using the high-frequency details. In their observation model, they modelled a low-resolution image as an aliased and noisy version of the corresponding high-resolution image and then the initial high-resolution and test image estimated the aliasing matrix entries. After that, the prior model for the super-resolved image was chosen as an Inhomogeneous Gaussian Markov random field (IGMRF) and the model parameters were estimated using the same initial high-resolution estimate. They used a maximum a posteriori (MAP) estimation in order to arrive at the cost function minimized using a simple gradient descent approach. Figure 6 shows the block diagram of the proposed method in [36].

Figure 5. Block diagram of the proposed method in [35].

Figure 6. Block diagram of the proposed method in [36].

In the proposed compression technique, the input image is firstly decomposed into its different frequency subbands by using 1 level DWT. The LL subband is then being compressed by using DWR and the high-frequency subbands, i.e., LH, HL, and HH, are being compressed by using SVD. The proposed technique has been tested on several well-known images such as, Lena, Peppers, Boat, and Airfield. The results of this technique have been compared with those of JPEG2000 and WDR with arithmetic coding techniques. The quantitative experimental results based on PSNR show that the proposed technique overcomes the aforementioned techniques. The SVD and WDR image compression techniques are discussed in the next section.

2. Review of singular value decomposition and wavelet difference reduction

2.1. Singular value decomposition

From a mathematical point of view, an image can be represented by a matrix, which consists of one or three layers in the case the image is grayscale or RGB, respectively. The results of the implementation of SVD on a grayscale image, which is represented by the single-layer image A, are three matrices U, Σ, and V, where U and V are orthogonal, and Σ is a diagonal matrix containing the singular values of A. In what follows, the SVD procedure is briefly reviewed. The relation between the matrix A, and the decomposed components, U, Σ, and V, can be mathematically presented through the formulation provided in Eqn. (1), where the dimensions of all the matrices are shown, given that the dimensions of the matrix A has been $m{\times}n$ [37, 38, 39]:

$$A_{m\times n} = U_{m\times m}\Sigma_{m\times n}\left(V_{n\times n}\right)^{T} \tag{1}$$

Eqn. (2) shows how a matrix $\bar{\Sigma}_{p\times q}$ with smaller dimensions $p{\leq}m$ and $q{\leq}n$ can be used to approximate the diagonal matrix with the dimensions m and n:

$$\Sigma_{m\times n} = \begin{bmatrix} \bar{\Sigma}_{p\times q} & 0 \\ 0 & \ddots \end{bmatrix} \qquad p \leq m \text{ and } q \leq n \tag{2}$$

Some columns of U and rows of V are then reduced in order to reconstruct the compressed image by multiplication. This is shown in Eqn. (3):

$$U_{m\times m} = \left[\bar{U}_{m\times p} \quad \widetilde{U}_{m\times(m-p)}\right] \quad \text{and} \quad V_{n\times n} = \left[\bar{V}_{n\times q} \quad \widetilde{V}_{n\times(n-q)}\right] \tag{3}$$

The compressed image is then obtained as shown in Eqn. (4):

$$A_{m\times n} = \bar{U}_{m\times p}\bar{\Sigma}_{p\times q}\left(\bar{V}_{n\times q}\right)^{T} \tag{4}$$

Because the singular matrix has sorted singular values (in descending order), by using the physcovisual concept, ignoring low singular value will not significantly reduce the visual quality of the image. Figure 7 shows Lena's picture being reconstructed by using different amount of singular values. This characteristic that an image can be reconstructed by fewer

amounts of singular values makes SVD suitable for compression. Because after reconstruction of the image the ignored singular values cannot be recovered, the compression by SVD is lossy [33].

Figure 7. Lena's image of size 256x256 reconstructed by Eq. (4) (a) original Lena image; (b) reconstructed using128 σ; (c) reconstructed using 64 σ; (d) reconstructed using32 σ.

2.2. Wavelet difference reduction

The WDR is a compression technique, which is based on the difference reduction method. The wavelet transform of the input image is first made; bit plane encoding is then applied to the

transform values. The bit plane encoding procedure starts with the initialization stage, where a threshold T_o is chosen such that T_o is greater than all the transform values, and at least, one of the transform values has a magnitude of $T_o/2$. The next stage is the initialization, where the threshold $T = T_{k-1}$ is updated to $T = Tk$, where $T_k = T_{k-1/2}$. New significant transform values ($w(i)$) which are satisfying $T \leq |w(i)| \leq 2T$ are then identified at the significant pass stage. The transform values of these significant transform values are then encoded using the difference reduction method. At the significant pass stage, already quantized values (w_Q) which satisfy $|w_Q| \geq 2T$ are then refined in order to reduce error [27, 29, 30].

3. The proposed lossy image compression technique

The proposed image compression technique is a lossy compression technique. Firstly, the image is decomposed into its frequency subbands by using DWT. Among these subbands, LL subband is being compressed by using WDR. The high-frequency subband images are being compressed by using SVD. The number of singular values that are being used in order to reconstruct the high-frequency subbands can be reduced into 1, i.e., the highest singular value is enough to reconstruct the high-frequency subbands. If only one singular value is being used in order to reconstruct a matrix, this means that only one column of U and V matrices are being used. The qualitative loss is not psychovisually noticeable up to some point. In order to obtain the compression ratio of the proposed technique, the total number of bits required to represent the original image is divided by the total of number of bits which is obtained by adding the number of bit streams of WDR for LL and that of the SVD compression for LH, HL, and HH.

Decompression is carried out by taking the inverse WDR (IWDR) of the bit streams in order to reconstruct the LL subband and in parallel the matrix multiplications are conducted in order to reconstruct LH, HL, and HH subbands. Due to the losses by ignoring low-valued singular values, high-frequency subbands need to be enhanced. For this purpose, stationary wavelet transform (SWT) is applied to the LL subband image which results in new low- and high-frequency subbands. These high-frequency subbands will have the same direction as the ones obtained by DWT (e.g., horizontal, vertical, and diagonal), so they will be added to the respective ones reconstructed by matrix multiplications. Now, the LL subband image obtained by IWDR and the enhanced LH, HL, and HH subbands are combined by using inverse DWT (IDWT) in order to reconstruct the decompressed image. The enhancement of high-frequency subbands by using SWT results in more sharpened decompressed image. The block diagram of the proposed lossy image compression technique is shown in Fig. 8. The experimental qualitative and quantitative results are represented and discussed in the next section.

4. Experimental results and discussion

As it was mentioned in the Introduction, for comparison purposes, the proposed lossy image compression was tested on many benchmark images, namely, Lena, Pepper, Boats, Airfield,
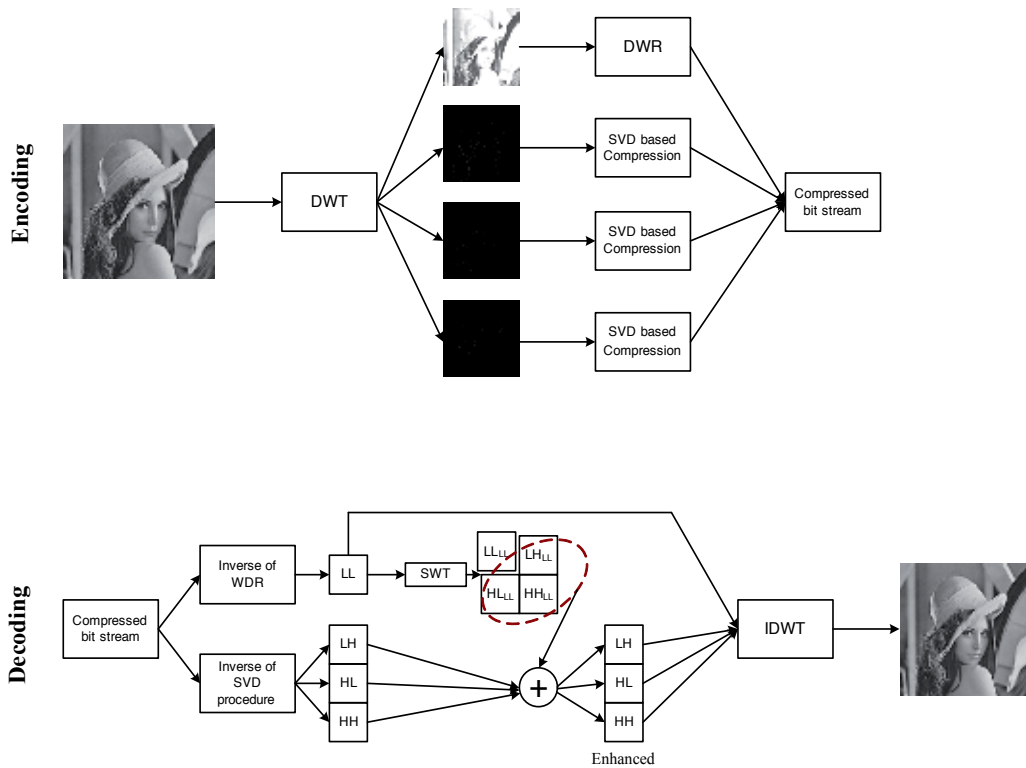
Figure 8. Block diagram of the proposed blocked based lossy image compression technique.

and Goldhill. All the input images were of resolutions *256* x *256* pixels, 8-bit grayscale. Tables 1, 2, and 3 provide a quantitative comparison between the proposed technique, JPEG2000, and WDR [40, 41] based on PSNR values, in dB, for compression ratios 20:1, 40:1, and 80:1, respectively.

The foregoing tables illustrate the superiority of the proposed method in terms of its capability in leading to significantly higher PSNR values compared to the other techniques proposed, previously, in the literature. It is worth noticing that the improvement in the PSNR values brought about by considering the proposed method might better show its impact while keeping in mind the fact that they are calculated in dB, meaning that a logarithmic function determines them, which clarifies how considerable the difference between the actual values has been. To be more clear, if one calculates the difference between the PSNR values obtained using WDR and JPEG2000, and subsequently, that of JPEG2000 and the proposed method, it can be seen that the latter is much higher than the former, although JPEG2000 has always been deemed of significantly better performance than WDR. Thus, it can be concluded that the proposed method makes an enormous enhancement to the PSNR values compared to the ones obtained upon employing WDR or JPEG2000.

Image	Techniques		
	WDR	JPEG2000	Proposed
Lena	35.72	35.99	**39.14**
Pepper	34.21	35.07	**40.07**
Boats	32.42	33.18	**35.97**
Airfield	27.02	27.32	**31.43**
Goldhill	31.76	32.18	**38.05**

Table 1. PSNR values in dB for 20:1 compression

Image	Techniques		
	WDR	JPEG2000	Proposed
Lena	32.44	32.75	**35.98**
Pepper	31.67	32.40	**36.45**
Boats	29.32	29.76	**32.03**
Airfield	24.72	24.88	**29.62**
Goldhill	29.43	29.72	**34.19**

Table 2. PSNR values in dB for 40:1 compression

Image	Techniques		
	WDR	JPEG2000	Proposed
Lena	29.71	29.62	**32.46**
Pepper	28.93	29.54	**33.07**
Boats	26.96	26.76	**30.19**
Airfield	22.71	22.64	**27.32**
Goldhill	27.72	27.69	**32.64**

Table 3. PSNR values in dB for 80:1 compression

In order to ensure the quality of the output of the proposed technique, and for visual illustration, the images resulting from the implementation of the foregoing approach were obtained, along with that of JPEG2000 and WDR. Figure 9 shows a part of the magnified Lena image having been compressed using the foregoing approaches, separately, with compression ratio 40:1. As sought from the outset, the proposed method is competent enough to maintain the quality of the image while compressing it, and at the same time, result in better PSNR, which shows its capability in correctly deciding on a reasonable trade-off between the amount of data needed to be transferred, or kept, and the visibility and authenticity of the details in the image

blocks, which is, probably, the most tricky criterion in devising image compression algorithms. As Fig. 9 illustrates, the overall quality of the Lena image being compressed by the proposed method is satisfactory despite possessing much higher PSNR value compared to the JPEG2000 and WDR techniques, and the details are clear and visible, even better than the output of the WDR.

(a)

(b)

(c)

(d)
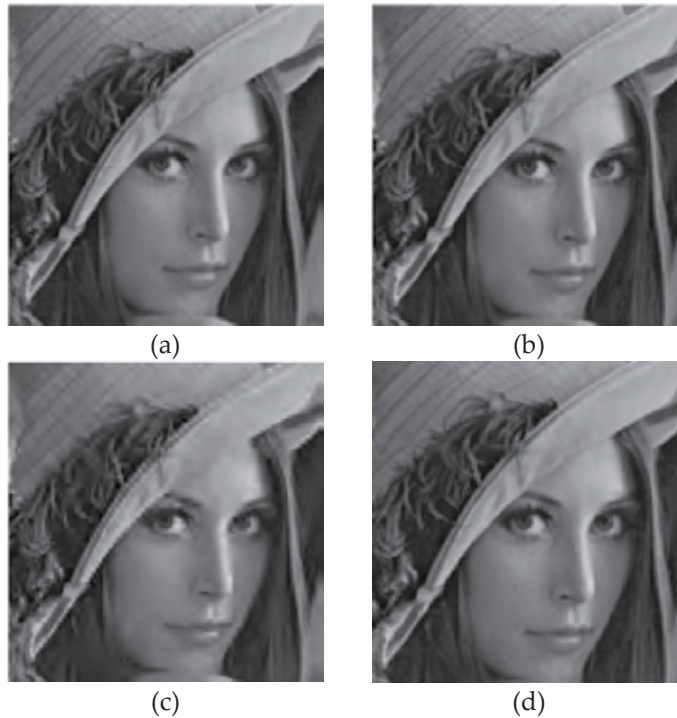
Figure 9. Zoomed (a) original Lena image, and compressed images by using (b) JPEG2000, (c) WDR, and (d) the proposed image compression technique at 40:1 compression ratio.

5. Conclusion

In this research work, a new lossy image compression technique which uses singular value decomposition and wavelet difference reduction techniques, followed by resolution enhancement, using discrete wavelet transform and stationary wavelet transform was proposed.

As the first step in the proposed image compression technique, the input image was decomposed into four different frequency subbands using discrete wavelet transform. The low-frequency subband was compressed using wavelet difference reduction, and in parallel, the high-frequency subbands were compressed using singular value decomposition. The compression ratio was obtained by dividing the total number of bits required to represent the input

image over the total bit numbers obtained by wavelet difference reduction and singular value decomposition.

Reconstruction was carried out using inverse wavelet difference reduction to obtain low-frequency subband and reconstructing the high-frequency subbands using matrix multiplications. The high-frequency subbands were enhanced using high frequency obtained by stationary wavelet transform. The reconstructed low-frequency subband and enhanced high-frequency subbands were used to generate the reconstructed image using inverse discrete wavelet transform.

The visual and quantitative experimental results of the proposed image compression technique showed that the proposed image compression technique outperformed the wavelet difference reduction and JPEG2000 techniques.

Acknowledgements

Author details

Gholamreza Anbarjafari[1,3*], Pejman Rasti[1], Morteza Daneshmand[1] and Cagri Ozcinar[2]

*Address all correspondence to: sjafari@ut.ee

1 iCV Group, IMS Lab, Institute of Technology, University of Tartu, Tartu, Estonia

2 Centre for Vision, Speech and Signal Processing, University of Surrey, Guildford, United Kingdom

3 Dept. of Electrical and Electronic, Faculty of Engineering, Hasan Kalynocu University, Gaziantep, Turkey

References

[1] T. Fujii, D. Shirai, Y. Tonomura, M. Kitamura, T. Nakachi, T. Sawabe, M. Ogawara, T. Yamaguchi, M. Nomura and K. Shirakawa, "Digital cinema and super-high-definition content distribution on optical high-speed networks," in *Proceedings of the IEEE*, pp. 140-153, 2013.

[2] A. Qian, C. Rongguan, N. a. G. S. Ning, Z. Xiaochen, Z. Jie and K. Deyu, "High-Definition Image Processing Algorithm and Digital Platform Design," in *Computer and Information Technology (CIT), 2012 IEEE 12th International Conference on*, 2012.

[3] K. Ishimaru, T. Fujii, T. Sawabe, J. Suzuki and S. Ono, "Transmission Characteristics of MPEG2 encoded super high definition images," in *Global Telecommunications Conference, 1996. GLOBECOM'96.'Communications: The Key to Global Prosperity*, pp. 289-293 1996.

[4] T.-J. Chen, H. Chiueh, C.-C. Hsieh, C. Yin, W.-H. Chang, H.-H. Tsai and C.-F. Chiu, "High Definition Image Pre-Processing System for Multi-Stripe Satellites' Image Sensors," *Sensors Journal, IEEE,* vol. 12, no. 9, pp. 2859-2865, 2012.

[5] G. Anbarjafari, S. Izadpanahi and H. Demirel, "Video resolution enhancement by using discrete and stationary wavelet transforms with illumination compensation," *Signal, Image and Video Processing,* vol. 9, no. 1, pp. 87-92, 2015.

[6] T. Celik, C. Direkoglu, H. Ozkaramanli, H. Demirel and M. Uyguroglu, "Region-based super-resolution aided facial feature extraction from low-resolution video sequences," in *Acoustics, Speech, and Signal Processing, 2005. Proceedings.(ICASSP'05). IEEE International Conference on*, pp. 785-789 2005.

[7] H. Demirel and G. Anbarjafari, "Discrete wavelet transform based satellite image resolution enhancement," *Geoscience and Remote Sensing, IEEE Transactions on,* vol. 49, no. 6, pp. 1997-2004, 2011.

[8] C. Liu and D. Sun, "On Bayesian Adaptive Video Super Resolution," *Pattern Analysis and Machine Intelligence, IEEE Transactions on,* vol. 36, no. 2, pp. 346-360, 2014.

[9] G. Polatkan, M. Zhou, L. Carin, D. Blei and I. Daubechies, "A Bayesian Nonparametric Approach to Image Super-Resolution," *Pattern Analysis and Machine Intelligence, IEEE Transactions on,* vol. 37, no. 2, pp. 346-358, 2015.

[10] P. Rasti, H. Demirel and G. Anbarjafari, "Image resolution enhancement by using interpolation followed by iterative back projection," in *Signal Processing and Communications Applications Conference (SIU), 2013 21st*, pp. 1-4, 2013.

[11] D. Glasner, S. Bagon and M. Irani, "Super-resolution from a single image," in *Computer Vision, 2009 IEEE 12th International Conference on*, pp. 349-356, 2009.

[12] G. Anbarjafari and H. Demirel, "Image Super Resolution Based on Interpolation of Wavelet Domain High Frequency Sub-bands and the Spatial Domain Input Image," *ETRI journal,* vol. 32, no. 3, pp. 390-394, 2010.

[13] C. Dong, C. Loy, K. He and X. Tang, "Learning a Deep Convolutional Network for Image Super-Resolution," in *European Conference on Computer Vision (ECCV), 2014 Springer Conference on*, pp. 184-199, 2014.

[14] Y. Zhu, Y. Zhang and A. Yuille, "Single Image Super-resolution Using Deformable Patches," in *Computer Vision and Pattern Recognition (CVPR), 2014 IEEE Conference on*, pp. 2917-2924 2014.

[15] K. Nasrollahi and T. Moeslund, "Super-resolution: a comprehensive survey," *Machine Vision and Applications,* vol. 25, no. 6, pp. 1423-1468, 2014.

[16] H. Demirel and G. Anbarjafari, "Data fusion boosted face recognition based on probability distribution functions in different colour channels," *EURASIP Journal on Advances in Signal Processing,* vol. 2009, p. 25, 2009.

[17] H. Demirel and G. Anbarjafari, "Iris recognition system using combined colour statistics.," in *Signal Processing and Information Technology, pp. 175-179, 2008.*

[18] X. Zhang, "Lossy compression and iterative reconstruction for encrypted image," *Information Forensics and Security, IEEE Transactions on,* vol. 16, no. 1, pp. 53-58, 2011.

[19] F. Hussain and J. Jeong, "Efficient Deep Neural Network for Digital Image Compression Employing Rectified Linear Neurons," *Journal of Sensors,* 2015.

[20] M. Boliek, "Beyond compression: a survey of functionality derived from still image coding," in *Signals, Systems and Computers, 2004. Conference Record of the Thirty-Seventh Asilomar Conference on*, pp. 1971-1974, 2003.

[21] R. C. Gonzalez and R. E. Woods, Digital Image Processing, Prentice Hall Upper Saddle River, NJ, 2002.

[22] A. Karami, M. Yazdi and G. Mercier, "Compression of Hyperspectral Images Using Discerete Wavelet Transform and Tucker Decomposition," *Selected Topics in Applied Earth Observations and Remote Sensing, IEEE Journal of,* vol. 5, no. 2, pp. 444-450, 2012.

[23] H. a. A. G. Demirel, C. Ozcinar and S. Izadpanahi, "Video Resolution Enhancement By Using Complex Wavelet Transform," in *Image Processing (ICIP), 2011 18th IEEE International Conference on*, pp. 2093-2096, 2011.

[24] M. Ghazel, G. H. Freeman and E. R. Vrscay, "Fractal-wavelet image denoising revisited," *{Image Processing, IEEE Transactions on,* vol. 15, no. 9, pp. 2669-2675, 2006.

[25] J.-F. Yang and C.-L. Lu, "Combined Techniques of Singular Value Decomposition and Vector Quantization for Image Coding," *IEEE Transactions on Image Processing,* vol. 4, no. 8, pp. 1141-1146, 1995.

[26] M. D. Greenberg, Differential equations & Linear algebra, Prentice Hall, 2001.

[27] J. Tian and R. O. Wells Jr, "Embedded image coding using wavelet difference reduction," in *Wavelet image and video compression*, pp. 289-301, 2002.

[28] J. Tian and R. O. Wells Jr, "A lossy image codec based on index coding," in *IEEE Data Compression Conference,*p. 456, 1996.

[29] J. Tian and R. O. Wells Jr, "Image data processing in the compressed wavelet domain," in *Signal Processing, 1996., 3rd International Conference on*, pp. 978-981 1996.

[30] S. Raja and A. Suruliandi, "Image Compression Using WDR and ASWDR Techniques With Different Wavelet Codecs," *ACEEE Int. J. Inform. Technol. v01*, pp. 23-26, 2011.

[31] H. Demirel and G. Anbarjafari, "Image resolution enhancement by using discrete and stationary wavelet decomposition.," *Image Processing, IEEE Transactions on*, vol. 20, no. 5, pp. 1458-1460, 2011.

[32] C. Kim, K. Choi, K. Hwang and J. B. Ra, "Learning-based superresolution using a multi-resolution wavelet approach," in *Iternational workshop on Advance Image Technology (IWAIT)*, 2009.

[33] H. Demirel and G. Anbarjafari, "Satellite image resolution enhancement using complex wavelet transform.," *Geoscience and Remote Sensing Letters, IEEE*, vol. 7, no. 1, pp. 123-126, 2010.

[34] R. C. Patel and M. V. Joshi, "Super-Resolution of Hyperspectral Images: Use of Optimum Wavelet Filter Coefficients and Sparsity Regularization," *Geoscience and Remote Sensing, IEEE Transactions on*, vol. 53, no. 4, pp. 1728 - 1736, 2015.

[35] H. Chavez-Roman and V. Ponomaryov, "Super resolution image generation using wavelet domain interpolation with edge extraction via a sparse representation," *Geoscience and Remote Sensing Letters, IEEE*, vol. 11, no. 10, pp. 1777-1781, 2014.

[36] P. P. Gajjar and M. V. Joshi, "New learning based super-resolution: use of DWT and IGMRF prior," *Image Processing, IEEE Transactions on*, vol. 19, no. 5, pp. 1201-1213, 2010.

[37] D. Kaiman, "A Singularly Valuable Decomposition," *College Mathematics Journal*, vol. 27, no. 1, pp. 2-23, 1996.

[38] L. Knockaert, B. De Backer and D. De Zutter, "SVD compression, unitary transforms, and computational complexity," *Signal Processing, IEEE Transactions on*, vol. 47, no. 10, pp. 2724-2729, 1999.

[39] S. J. Nivedita, "Performance Analysis of SVD and SPIHT Algorithm for Image Compression Application," *International Journal of Advanced Research in Computer Science and Software Engineering*, vol. 2, no. 2, 2012.

[40] J. S. Walker, T. Q. Nguyen and Y.-J. Chen, "A low-power, low-memory system for wavelet-based image compression," *Optical Engineering, Research Signposts*, vol. 5, pp. 111-125, 2003.

[41] J. S. Walker and T. Q. Nguyen, "Wavelet-based image compression," in Transforms and Data Compression, CRC Press, 2001.

Adaptive Wavelet Packet Transform

Zuofeng Zhou and Jianzhong Cao

Additional information is available at the end of the chapter

Abstract

Two-dimensional over-complete wavelet packet transform can better represent the texture and long oscillatory patterns in natural images.

In this chapter, combining the doubly Wiener filtering algorithm and Wiener cost function, a new best wavelet packet decomposition scheme for image denoising applications is proposed. The experiment results for the test image database show the effectiveness of the proposed image denoising algorithm compared to some existing image denoising methods.

Keywords: Adaptive wavelet packet transform, Wiener cost function, image denoising

1. Introduction

Wavelet with vanishing moments are very effective for representing piecewise smooth images [1]. However, two-dimensional separable wavelets are ill-suited to represent long oscillatory patterns in images with abundant textures, partly owing to their poor directional selectivity in frequency domain. These oscillatory variations of intensity can only be represented by small-scale wavelet coefficients. In some image-processing applications, such as image denoising or image compression, those small-scale coefficients are quantized to zero in the low bit rate image compression and are thresholded or shrunken to zero in image denoising, which degrades compression and denoising performance significantly. To overcome this circumstance, one way is to find the more suitable image representation techniques such as curvelet, contourlet [2], and ridgelet [3]. But these methods need the researchers to design the new directional compact filter or multichannel filter banks, which is also challenging in filter design area. Another way is to improve the idea of wavelet design method to accommodate the new requirement where the over-complete wavelet packet decomposition is proposed.

Over-complete wavelet packet contains a mass of libraries of waveforms, from which the best wavelet packet base can be selected to efficiently represent long oscillatory patterns given the corresponding criterion. For example, in image compression application, the best wavelet packet base is usually found by pruning the full wavelet packet decomposition given a user predefined cost function. Recently, a large variety of cost function have been proposed, such as Shannon's entropy cost function and vector entropy cost function, which are used in the rate distortion control strategy. On the other hand, different from finding the best tree structure of the wavelet packet decomposition, some researchers devoted themselves for finding the best wavelet packet decomposition base [4] which is equivalent to find the best filter banks of wavelet packet decomposition.

In image denoising application, due to unknown noiseless image as well as a great diversity of filtering methods in the transform domain, selecting the best wavelet packet base is always a difficult problem. Enlightened by the idea of doubly local Wiener filtering method [5] and spatially adaptive wavelet domain shrinkage image denoising algorithms, the best wavelet packet bases selection method using the local Wiener cost function and its application in image denoising is proposed. In this chapter, we will first give the detail of the best wavelet packet-based selection algorithm and then discuss its application in image denoising.

2. Best wavelet packet base selection

Let $\psi^0(x)$, $\psi^1(x)$ be the wavelet function and scaling functions, the basic idea of wavelet packet function can be defined as:

$$
\begin{aligned}
\psi^{2n}(x) &= \sqrt{2}\sum_k h(k)\psi^n(2x-k), \\
\psi^{2n+1}(x) &= \sqrt{2}\sum_k g(k)\psi^n(2x-k), \quad \text{for } n \geq 1
\end{aligned}
\tag{1}
$$

where $h(k)$, $g(k)$ are the orthonormal filters, respectively. Given a signal $s(n)$ which is satisfied the Nyquist sampling criterion, subspace $V_0 \equiv \text{span}\{\psi^0(x-l):l\in\mathbb{Z}\}$ is usually assumed to be the first-level subspace of signal $s(n)$. The subspace with depth j is defined as $V_j^n \equiv \text{span}\{\psi_{j,l}^n(x)=2^{-j/2}\psi^n(2^{-j}x-l), l\in\mathbb{Z}\}$. To understand this subspace easily, the dynamic interval $[2^{-j}n, 2^{-j}(n+1))$ can be associated with the subspace V_j^n. For example, the interval $[0, 1)$ is equivalent to V_0.

2.1. Two-dimensional wavelet packet bases

The two-dimensional separable wavelet packet functions are defined as the tensor products of two one-dimensional wavelet packet functions, that are,

$$
\begin{aligned}
V_0 &= \text{span}\{\psi^0(x-l)\psi^0(y-p):(l, p)\in\mathbb{Z}^2\} \\
\psi^{m,n}(x, y) &= \psi^m(x)\psi^n(y), \quad m, n \in 0, 1, \ldots
\end{aligned}
\tag{2}
$$

Similar to the one-dimensional case, the subspace

$$V_j^{m,n} \equiv \text{span}\left\{\psi_{j;l,p}^{m,n}(x) = 2^{-j}\psi^m(2^{-j}x-l)\psi^n(2^{-j}y-p),\ (l,\ p) \in \mathbb{Z}^2\right\} \tag{3}$$

is referred to as the subspace with depth j and a wavelet packet function $\psi^{m,n}(x,y)$. Figure 1 gives the subspace of 2D wavelet packet base diagram. It can be seen that each node is divided into two branches. Let us associate the dyadic square $[2^{-j}m,\ 2^j(m+1)) \times [2^{-j}n,\ 2^{-j}(n+1))$ with the subspace $V_j^{m,n}$, for example, V_0 associates with the square $[0,\ 1)^2$, $V_1^{1,0}$ associates with the rectangle $[1/2,\ 1) \times [0,\ 1/2)$, and $V_1^{1,1}$ associates with the square $[1/2,\ 1)^2$. It has been proved that: if the squares $[2^{-j}m,\ 2^{-j}(m+1)) \times [2^{-j}n,\ 2^{-j}(n+1))$, $(m,\ n,\ j) \in \Omega$ are a partition of the unit square $[0,\ 1)^2$, then the family of functions $\left\{\Psi_{j;l,p}^{m,n}(x,\ y):(l,\ p) \in \mathbb{Z}^2,\ (m,\ n,\ j) \in \Omega\right\}$ constitutes an orthogonal wavelet packet base of V_0.
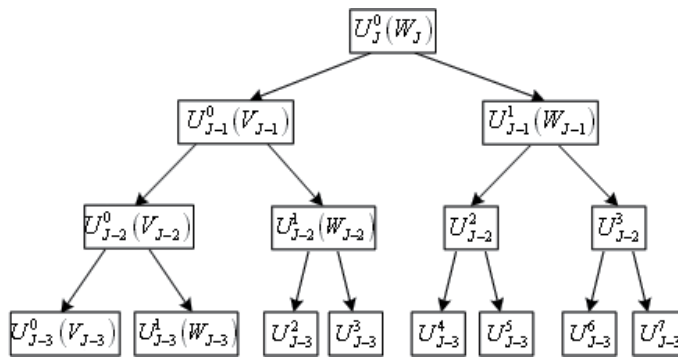
Figure 1. The subspace of 2D wavelet packet base

2.2. Best wavelet packet base selection under wiener cost function

Similar to the tree structure illustrated in Fig. 1, 2D wavelet packet decomposition can be easily expressed by the quad-tree structure with the root node $\{0, 0, 0\}$. Each node (m, n, j) (except the last level node) has four child nodes $(2m, 2n; j+1)$, $(2m, 2n+1, j+1)$, $(2m+1, 2n, j)$ and $(2m+1, 2n+1, j+1)$. This quad-tree structure facilitates the best wavelet packet decomposition procedure. Given the image and the noise level σ (if unknown, the noise level can be estimated by the MAD estimator in the wavelet domain), the wavelet packet coefficient at the node (m, n, j) under J-level wavelet packet decomposition is represented as $y_j^{m,n}(p, q)$, $m, n = 0, 1, \ldots, 2^j - 1$; $j = 0, 1, \ldots, J$. For each node, its Wiener cost function is computed by

$$J(m,n;j) = \sigma^2 \sum_p \sum_q \frac{\left[y_j^{m,n}(p,q)\right]^2}{\left[y_j^{m,n}(p,q)\right]^2 + \sigma^2},\quad m,n = 0,1,\ldots,2^j - 1;\ j = 0,1,\ldots,J. \tag{4}$$

Assuming all the node in the quad-tree decomposition forms a set Class $(\mathbf{A})=\{\Omega=\{(m,\ n,\ j)\}$, our task is to find a subset Ω^* from set Ω which have the smallest total cost function (the summation of the Wiener cost function at all wavelet packet decomposition node).

Similar to most of the search algorithms of the best wavelet packet base, the best wavelet packet base under Wiener cost function is obtained by pruning a J-level full quad-tree from bottom to top. The searching algorithm can be described as follows:

i.   Let $S(m,\ n,\ J)=\{(m,\ n,\ J)\}$, m, $n=0,\ 1,\ \cdots,\ 2^J-1$ represent 2^{2J} leaf nodes in the J-level full quad-tree.

ii.   For $0\le j<J$ and each node $(m,\ n,\ j)$ in the j-th level, calculate the corresponding Wiener cost function

$$J\left(m,n;j\right)=\sigma^2\sum_p\sum_q\frac{\left[y_j^{m,n}(p,q)\right]^2}{\left[y_j^{m,n}\left(p,q\right)\right]^2+\sigma^2} \tag{5}$$

as well as the summation of the Wiener cost functions of its four child nodes by

$$\tilde{J}(m,n,j)=J(S(2m,2n,j+1))+J(S(2m,2n+1,j+1))+$$
$$+J(S(2m+1,2n,j+1))+J(S(2m+1,2n+1,j+1))$$

iii. If $\tilde{J}(m,\ n,\ j)<J(m,\ n,\ j)$, then

$$S(m,n,j)=S(2m,2n,j+1)\bigcup S(2m,2n+1,j+1)\bigcup S(2m+1,2n,j+1)\bigcup S(2m+1,2n+1,j+1)$$

otherwise, $S(m,\ n,\ j)=\{(m,\ n,\ j)\}$.

iv.   Calculate the Wiener cost function of each set $S(m,\ n,\ j)$ by

$$J\left(S\left(m,n,j\right)\right)\equiv\sum_{(u,v,r)\in S(m,n,j)}J\left(u,v,r\right),\quad m,n=0,1,\ldots,2^j-1, \tag{6}$$

v.   If $j>0$, set $j\leftarrow j-1$ and return the step (ii); otherwise, output $\Omega^*=S(0,\ 0,\ 0)$.

The set Ω^* is composed of all leaf nodes of the best quad-tree decomposition structure. In this way, given the input noisy image and the noise level, the optimal orthogonal wavelet packet decomposition structure and the minimal total Wiener cost function can be obtained. Figure 2 shows a demo of best wavelet packet decomposition where Fig. 2(a) is its square representation and Fig. 2 (b) is the corresponding tree structure of this best wavelet packet decomposition.
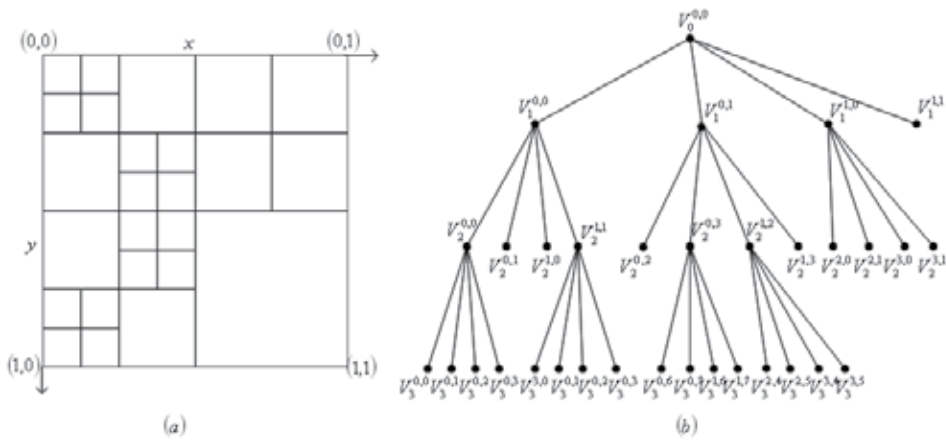
Figure 2. A demo of best wavelet packet decomposition

3. Image denoising algorithms based on best wavelet packet decomposition

This section gives two image denoising algorithms based on the best wavelet packet decomposition. In the above section, the optimal wavelet packet decomposition structure is obtained under the Wiener cost function. When computing the Wiener function, the noiseless image and the noise level are assumed as known. In practice, this assumption is unreasonable. It is well known that the noise level can be accurately estimated by the MAD estimator from the input noisy image. The key problem is how to estimate the noiseless image. Enlightened by the empirical Wiener filtering and the doubly local Wiener filtering image denoising algorithms, we first filter the noisy image to get the pilot image, and then the pilot image is used to get the best wavelet packet decomposition structure.

It is well known that undecimated wavelet packet decomposition can achieve better image denoising performance than the decimated wavelet packet decomposition. This is owing to the property that they are shift invariance and robustness. So, the undecimated wavelet packet decomposition can ameliorate some unpleasant phenomenon that appears in the maximally decimated wavelet packet decomposition, such as Gibbs-like ringing around edges and specks in smooth region.

In what follows, we will give the detail of the image denoising algorithm using the undecimated wavelet decomposition. Let $x(p, q)$ be a input noisy image of size $2^N \times 2^N$, the operator $\text{Shift}_{k,l}(x)$ denotes circularly shifting the input image $x(p, q)$ by k indices in the vertical direction and l indices in the horizontal direction, and the operator $\text{Unshift}_{k,l}(x)$ is a similar operation but in the opposite direction. In the proposed algorithm, we first use the decimated best wavelet packet decomposition algorithm to denoise all possible shift versions of the noisy image to get a set of denoised images and then unshifting these denoised images and average

them to get the final denoised image. The new algorithm is referred to as the local Wiener filtering using the best undecimated wavelet packet decomposition (LWF-BUWPD), which can be summarized as follows:

i.   Using the local Wiener filtering image denoising algorithm to each shift of input noisy image shift $(x(p, q))$ to get a pilot image $\hat{s}(p, q)$;

ii.   Given the pilot image and noise level, the best wavelet packet decomposition structure can be obtained by using the searching algorithm in section 2.

iii.   Given the best wavelet packet decomposition structure, the empirical energy distribution of the pilot image can be estimated by

$$E_j^{m,n}(p,q) = \left\{ \frac{1}{\#W} \sum_{(s,t)\in W} \hat{s}_{j,m,n}^2(p+s,q+t) \right\}_+, (m,n,j)\in\Omega^* \tag{7}$$

where W and $\hat{s}_{j,m,n}(p, q)$ represent the directional window and the pilot image's best wavelet packet decomposition coefficients, respectively.

iv.   Using the estimated energy distributions and noise level, the local Wiener filtering is operated on the base wavelet packet decomposition coefficients of the noisy image, that is,

$$\tilde{s}_j^{m,n}(p,q) = \frac{E_j^{m,n}(p,q)}{E_j^{m,n}(p,q)+\sigma^2} y_j^{m,n}(p,q), (m,n,j)\in\Omega^* \tag{8}$$

where $y_j^{m,n}(p, q)$ are the best wavelet packet decomposition coefficients of the noisy image in the subspace $V_j^{m,n}$.

v.   Unshift all the shifted denoised images and average them to obtain the final denoised image $\tilde{s}(p, q)$

$$\tilde{s}(p,q) = \frac{1}{2^{2J}} \sum_{k=0}^{2^J-1} \sum_{l=0}^{2^J-1} Unshift_{k,l}(\tilde{s}_{k,l})(p,q) \tag{9}$$

4. Experimental results

We choose the 8-bit 512 × 512 grayscale images "Lena" and "Barbara," and a 256 × 256 texture image, as the test images. In the proposed image denoising algorithm, the best wavelet packet decomposition structure is varied with different shift noisy images and different noise level. For better illustration, the best wavelet packet decomposition structure for different noise level is shown in Fig. 3 for "Barbara" image.
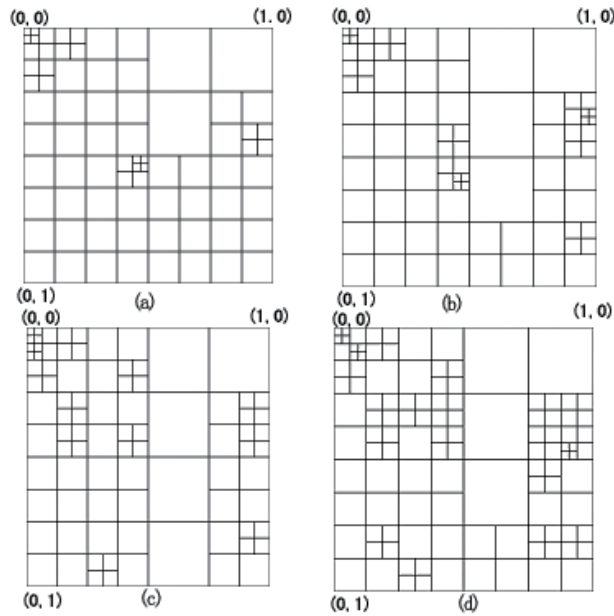
Figure 3. The best wavelet packet trees for the "Barbara" image with different noise levels: (a) $\sigma = 10$; (b) $\sigma = 15$; (c) $\sigma = 20$; (d) $\sigma = 25$.

In Table 1 and Fig. 4, we give the denoising performance of the image denoising algorithms using the undecimated best wavelet packet decomposition. The experimental results show that for images of structural textures, for example, "Barbara" and texture images, the proposed algorithm greatly improves denoising performance as compared with the existing state-of-the-art algorithms.

Test image	Boat				Fingerprint				House			
Noise level	10	15	20	25	10	15	20	25	10	15	20	25
DLWFDW	33.43	31.47	30.10	29.09	32.21	30.01	28.51	27.34	35.14	33.21	31.91	30.92
DFB-GSM	**33.58**	**31.70**	**30.37**	**29.13**	32.45	30.14	28.60	27.45	35.35	33.64	32.39	31.40
LWF–BUWPD	**33.58**	31.69	30.36	29.36	**32.51**	**30.22**	**28.66**	**27.56**	**35.37**	**33.65**	**32.42**	**31.42**
Test Images	Lena				Barbara				Texture			
Noise level	10	15	20	25	10	15	20	25	10	15	20	25
DLWFDW	35.3	33.5	32.2	31.2	33.9	31.5	29.9	28.6	33.92	31.68	30.11	29.03
DFB-GSM	**35.61**	**33.90**	**32.66**	**31.69**	34.03	31.86	30.32	29.13	34.83	32.61	30.95	29.71
LWF–BUWPD	35.60	33.87	32.65	31.66	**34.35**	**32.28**	**30.80**	**29.63**	**34.97**	**32.92**	31.72	30.65

Table 1. The performance comparison of the LWF-BUWPD and several state-of-the-art image denoising algorithms

(a)   (b)
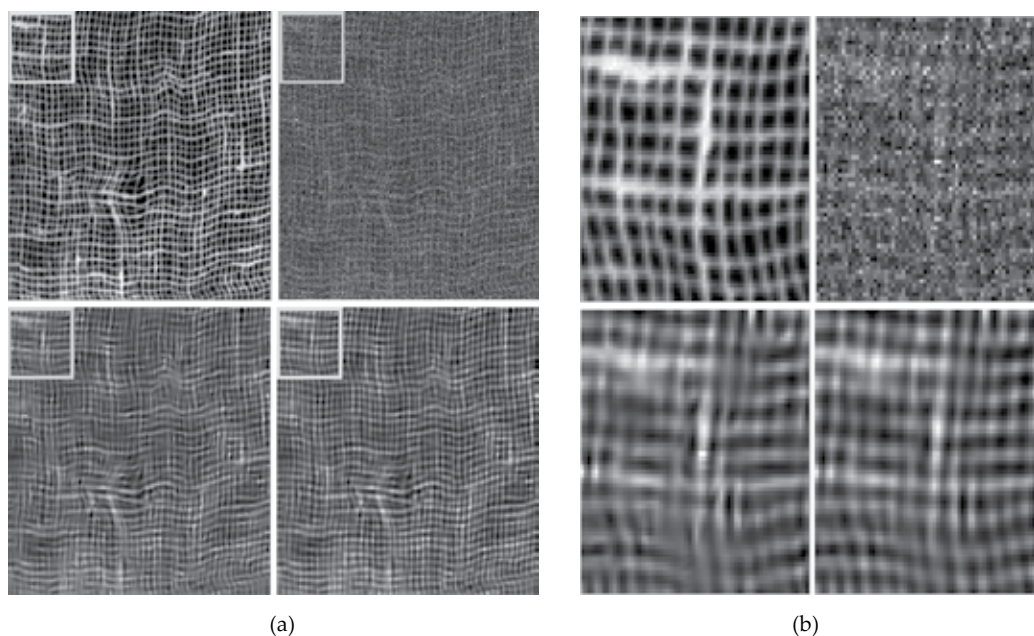
Figure 4. (a) The noiseless image (the left top corner), the noisy image (the right top corner, noise level 20), the denoised image by the DFB-GSM algorithm (the left bottom corner, PSNR = 30.93 dB), and the denoised image by the LWF-BUWPD algorithm (the right bottom corner, PSNR = 31.70 dB); (b). Zoomed local regions of the four images in (a).

Author details

Zuofeng Zhou[*] and Jianzhong Cao

*Address all correspondence to: zfzhou@opt.ac.cn

Xi'an Institute of Optics and Precision Mechanics of Chinese Academy of Sciences, Xi'an, Peoples Republic of China

References

[1] Shui, P.-L., Zhou, Z.-F., and Li, J.-X., "Image denoising based on adaptive wavelet packets using wiener cost function," IET Image Processing, 2007, 1(3), pp: 311–318.

[2] Minh, D., and Martin. V., "The contourlet transform: an efficient directional multiresolution image representation," IEEE Transactions on Image Processing, Dec. 2005, 14(12), pp: 2091–2106.

[3] Zhang, B., Jalal M.F., and Starck J.-L., "Wavelets, ridgelets, and curvelets for poisson noise removal," IEEE Transactions on Image Processing, 2008, 17(7), pp: 1093–2009.

[4] Mahalakshmi, B.V., and Anand, M.J., "Adaptive wavelet packet decomposition for efficient image denoising by using neighsure shrink method," International Journal of Computer Science & Information Technology 2014, 5(4), pp: 5003–5007.

[5] Shui, P.-L., "Image denoising algorithm via doubly local Wiener filtering with directional windows in wavelet domain," IEEE Signal Processing Letters, 2005, 12(10), pp: 681–684.

Scaling Factor Threshold Estimator in Different Color Models Using a Discrete Wavelet Transform for Steganographic Algorithm

Blanca Esther Carvajal-Gámez, Erika Hernández Rubio and
Amilcar Meneses Viveros

Additional information is available at the end of the chapter

Abstract

Two of the main problems with steganographic algorithms are insertion capability and minimization of distortion in the digital files where the hidden information is the information is inserted to hiding Digital filters are generally used as noise detectors, and they also suppress information outside the original information contained in the file. There are different types of filtering, one in the spatial domain and the other in the frequency domain or sometimes a combination of both domains to propose adaptive filters. One of the filters with greater application is the discrete wavelet transform (DWT) because it is easy to implement and has low computational complexity. The DWT computationally implemented in an image can be represented as a quadrature mirror filter, separating the frequency components: so high-high, high-low, low-high and low-low levels obtain different resolutions.

Using the scaling factor the DWT, adjusting the distortion of the image filtered help for noise detection, and eases the insertion of the data to hide. The DWT is applied to each new sub-image for does not generate a pattern of data distribution because each time an image is processed, it is often statistically and spatially changed.

Therefore, the steganographic algorithm can go through a stego-analyzer without data detection problem because the color palette is not affected. For this case study, the best result is when variable j = 10.

Keywords: Steganographic algorithm, digital filters, frequencial domain, spatial domain, discrete wavelet transform

1. Introduction

Hiding information concerns the process of integrating information or data elements into music, video, and images [1]. The concept of information hiding had also been proposed to solve problems related to intellectual property protection that depends directly on a team of background work for its realization, and its distribution must be controlled, or even protection of personal information with a high degree of confidentiality such as agreements, contracts, or other information that should be secured. To send information to a file imperceptibly seems totally innocent, at first, and such a file is known as a carrier file or host file (known as a host image or cover image).These files are carriers of embedded information; they can be any digital files such as audio files, video files or image files. For intellectual property protection and for secure delivery of information on unprotected media, various techniques have been implemented that have given rise to the emergence of the science of encryption, watermarking, and steganography. For the first technique, the message will not make any sense unless acquired by the intended recipient or to whom the message is addressed, as this will be the interpretation of each of the written symbols within the message. For watermarking, this is related to protecting the authenticity of media messages exposed, susceptible to cloning or replication. With watermarks, its authenticity is guaranteed. Finally, we have steganography, which is the technique used to hide information in a seemingly innocent means to be sent over an unsecured medium or channel. A common example is the wireless medium, which is fully exposed and for anyone with enough malice to access information, it can be done without any problem. For the goals of steganography to be met, there are three considerations: (i) high capacity for integration, (ii) high quality of stego-image and (iii) full recovery of the inserted information. The images with the inserted information are called stego-image; the information must be inserted in areas that are statistically and perceptually not easy to locate on demand and stego-tools such as analyzers. The stego-image should be, in theory and in practice, identical to the host image. The embedded information in the stego-image can only be removed by the receiver that has the primary key, otherwise, the information cannot be extracted. The stego-image is then sent to the intended recipient. The information contained in the host image is just a distraction to the receiver, so this is not so much of an interest in its full recovery, but the host image must have the minimum quality because any edge, contour,, color or misplaced pixels can cause some suspicion and is susceptible to the extraction of the hidden information without authorization from the transmitter. Most importantly, the hidden information must be fully recoverable. In today's advanced and modern world, steganography is vital because it is a support tool to copyright protection, for which the authentication processes allow distribution and legal use of different materials. A steganographic technique is usually evaluated in terms of the visual quality and the embedding capacity; in other words, an ideal steganographic scheme should have a large embedding capacity and excellent stego-object visual quality.

One of the main objectives of steganography is not sacrifice image quality as the carrier to be inserted to this data. And likewise keeping track information retrieved data. Because any disturbance visual may cause some reason for inspection of its content through histograms or specialized software.

The more reasonable way to deal with this trade-off situation is probably to strike a balance between the two [2, 3, 4].

The techniques implemented in steganography have evolved as needs related to security level and insertion capability have also increased, due to the growing trend in the digital distribution of files over public networks. There are several proposed techniques applied to steganography, including the space where the most representative method algorithm is the modification of the least significant bit (LSB) of the pixel, and from this algorithm, optimizations have emerged such as the LSBO, among others [5].

Subsequently, frequency techniques for image processing such as the discrete Fourier transform (DFT), discrete cosine transform of (DCT), and the discrete wavelet transform (DWT) have also emerged.

More recently, adaptive methods, take the qualities of the spatial domain and the frequency domain. These latest adjustments have yielded good results; however, few authors consider the three criteria for steganographic algorithms. In adaptive methods, statistical variations are considered image through variance, standard deviation, covariance, etc.

These statistics variations detected in images in conjunction with filtering images using the DWT techniques are useful and important to execute noise detectors within the image. These noisy areas are imperceptible to the human eye, so the eye does not see that some information have been inserted outside the original image. The human eye is less sensitive to detect certain imperfections contained in the processed images, these characteristics are due to the textures contained in the images that are shown as changes in intensity. These abrupt changes in intensity are contained in the high frequency band, which are obtained from the image processing by DWT [6].

In applications where the frequency domain is involved, depending on the nature of the image used as host, this image can be altered significantly when the digital filters applied act as noise detectors. Judging by whether the human vision sensitivity is considered in the design of the embedding algorithm, we can categorize the schemes into three types: (1) high embedding capacity schemes with acceptable image quality [2-4], (2) high image quality schemes with a moderate embedding capacity [2-4], and (3) high embedding efficiency schemes with a slight distortion [7,8]. This chapter explains how to reduce the effects of the filters on images using the scale factor proposed in this research. This scale factor will be working in the wavelet domain. Applying the scaling factor, the energy generated by the host image is preserved to approximate the original image, eliminating any visual disturbance. This chapter is divided into the following sections: Section 2. Materials and methods, Section 3. Theory and calculations, Section 4. Discussion and Section 5. Conclusions.

2. Materials and methods

To analyze structures within images of different sizes, shifting the window in Fourier transform (Gabor Transform [9]) is not suitable because it is subject to a fixed size value. Moreover,

the calculation is complicated, because the DFT, obtains complex numbers, unlike the DWT [9], which operates only with real numbers. For analysis of images, it is necessary to use time-frequency windows with different times. Instead of choosing a fixed window (Gabor transform), with an analysis window g (t-u) constant size, a resizable window is chosen, that is, a wavelet, a $\Psi \in L^2$function (IR), with an average equal to zero:

$$\int_{\infty}^{\infty} \psi(t)dt = 0 \qquad (1)$$

The DWT can decompose an image in different resolutions, each of which progressively decreases the size. This presents a certain analogy with the human eye, which draws, at each level, the information that it finds interesting. For example, consider a brick wall. If we observe it from a considerably large distance, we will see a global structure. As we approach the wall, we can look at the successive characteristic details: the divisions between bricks, each brick structure that define and detail the whole structure, losing resolution. Similarly, the DWT extracts information between successive resolutions. Consider the function checks $|| \Psi || = 1$, and is focused on a neighborhood of t = 0. If the value of u and s in the function moves, a movement of the sampling window time-frequency is obtained:

$$\psi_{u,s}(t) = \frac{1}{\sqrt{2}} \psi\left(\frac{t-u}{s}\right). \qquad (2)$$

The DWT can be written as a convolution product:

$$Wf(x,s) = \int_{\infty}^{\infty} f(t)\frac{1}{\sqrt{2}} \psi\left(\frac{t-x}{s}\right) ds = f\bar{\psi}_s(x). \qquad (3)$$

where $\bar{\psi}_s(t) = \frac{1}{\sqrt{2}} \psi^*\left(-\frac{t}{s}\right)$.

The DWT can find localized and structured images with an amplification procedure that progressively reduces the scale parameter. Generally, singularities and irregular structures often contain essential information about the image and refer to places that can be substituted for values, but at first glance, are not identifiable. In an image, intensity discontinuities indicate the presence of edges. It can be proven that the local regularity of a signal is characterized by the decay of the amplitude of the DWT over scales. Thus, the singularities and the edges are detected following the local maximum values of the DWT to finer scales detail. This image of singularities will become detailed as it moves [10]. To characterize the unique structures, it is necessary to quantify the local regularity of the image. For example, an image of n × m pixels generates additional images successively in blocks. All contours, large and small, are present in the original image and do not require any change of resolution to locate them. The issue is in identifying broad contours using conventional operators. It could be escalated to the operator, but what is more efficient is to scale the image because the use of an operator for

large contours on a high-resolution image is very complicated from the point of view of computational efficiency. Therefore, it uses coding frequency sub-bands. Coding performs sub-band decomposition of an image or a signal band-limited components (band-pass filter), which gives a redundancy-free representation of an image; this makes it possible to reconstruct the original image without error. Give a band-limited image $x(n,m)$ which satisfies [11]:

$$F\{x(n,m)\} = X(f) = 0, |f| \geq f_{max}. \tag{4}$$

It is possible to split the image to make a uniform sampling

$$x(i\Delta_{n,m}), i = 0,2,\ldots,N = 1 \quad f_{max} \leq f_N = \frac{1}{2\Delta_{n,m}}. \tag{5}$$

where f_N is the Nyquist frequency. For the analysis of the frequency division at intervals within the DWT; you can use a range of frequencies, for this particular case; We employ the value of N / 2 x M / 2, where N and M represent the length and width of the image as shown in Figure 1.
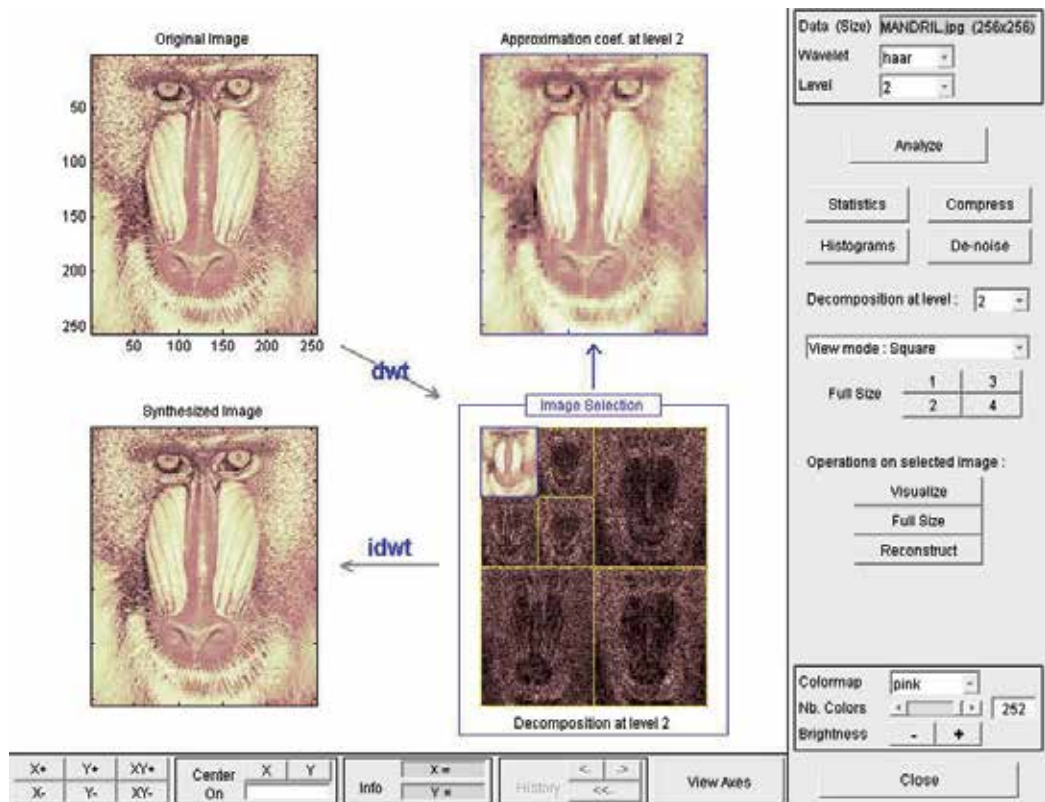
Figure 1. Double wavelet decomposition applied in an image.

The coding of two channels per sub-band filtering $x(\Delta x_{n,m})$ required by the impulse response for a low-pass filter $h_0(i\Delta_{n,m})$ and $h_1(i\Delta_{n,m})$ followed by sub-sampling (decimation 2), every output. The filtering functions given in Eq. 4 and 5 apply to the rows and columns of the image.

$$g_0\left(k\Delta_{n,m}\right) = \sum_i x\left(\Delta i(n,m)\right)h_0\left[\left(\Delta i + 2k\right)\Delta_{n,m}\right] \tag{6}$$

$$g_1\left(k\Delta_{n,m}\right) = \sum_i x\left(\Delta i(n,m)\right)h_1\left[\left(\Delta i + 2k\right)\Delta_{n,m}\right] \tag{7}$$

This results to obtaining the four sub-images at the output of the processing. The image resolution applying DWT is divided into four frequency sub-bands called Low-Low (LL), Low-High (LH), High-Low (HL), and High-High (HH), see Figure 2. The names given were based on the type of filtering applied to the rows and columns; they are obtained from Eqs. 6 and 7.
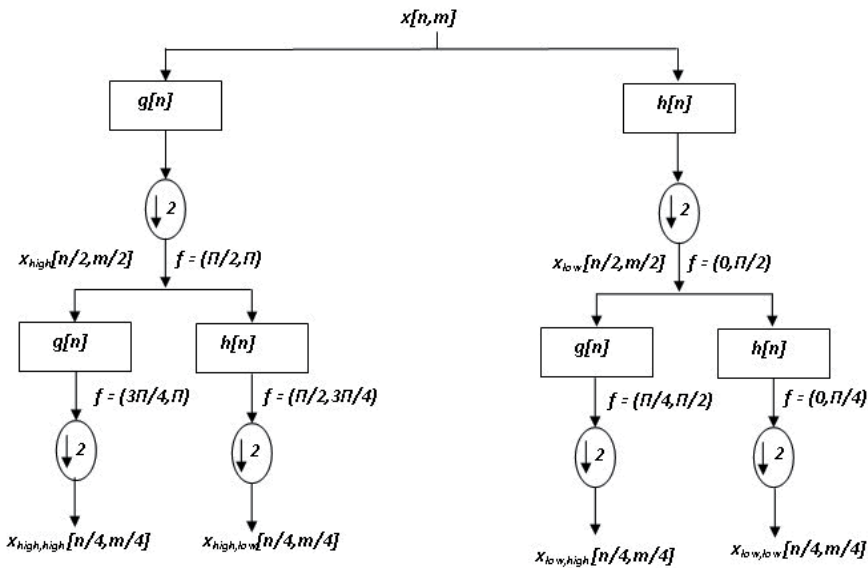
Figure 2. Sub-band coding for an image.

Each sub-band is a copy of the original image but in different frequency level, which provides a certain amount of energy [8, 9] (Figure 1). To describe a DWT, it is enough to define a discrete impulse response for a low-pass filter, $h_0(k)$, which satisfies the requirements $h_1[(N-1)\Delta x] = (-1)^i h_0(i\Delta x)$. Where from $h_0(k)$, we can generate the function $f(x)$ called scaling function. We can also generate, $h_1(k)$, with this last and with $f(x)$, calculate the mother wavelet $y(x)$. If the scaling vector has a finite number of nonzero terms, then $f(x)$ and $y(x)$ generate wavelets with compact support. Scaling a vector such that [11],

$$\sum_k h_0(k) = \sqrt{2}, \quad and \quad \sum_k h_0(k) h_0(k+2l) = \delta(l) \tag{8}$$

where *2l* represents the displacement of the sample image every 2 pixels. There exists a scaling function for which,

$$\phi(x) = \sum_k h_0(k) \phi(2n - k) \tag{9}$$

which can be constructed as a sum, from Eq. 11, that is half copy of the image, using $h_0(k)$ as the weighting factor. The scaling function is a continuous function whose general form is the same as the impulse response of discrete low-pass filter, $h_0(k)$. If instead the calculation begins from the scaling function *f(x)*, it must be an orthonormal unit in terms of translations [11],

$$\langle \phi(x - m), \phi(x - n) \rangle = \delta_{m,n} \tag{10}$$

and $h_0(k)$ can be calculated,

$$h_0(k) = \langle \phi_{1,0}(0), \phi_{0,k}(x) \rangle \tag{11}$$

where

$$\phi_{j,k}(n) = 2^{j/2} \phi(2^j n - k), \quad j = 0,1\ldots \quad k = 0,1,\ldots,2^j \quad 1 \tag{12}$$

Determined *f(x)* and $h_0(k)$, we can define a discrete impulse response for the high-pass filter called wavelet vector,

$$h_1(k) = (-1)^k h_0(-k + 1) \tag{13}$$

and from this, we obtain the mother wavelet,

$$\psi(n) = \sum_k h_1(k) \phi(2n - k) \tag{14}$$

where the set of orthonormal wavelets is derived, and the scaling factor obtained for setting the pixel with the new value obtained from the low-pass and band-pass filtering from [11],

$$\psi_{j,k}\left(n\right) = 2^{j/2}\psi\left(2^{j}n \cdot k\right) \tag{15}$$

It is restricted to case basis functions obtained by means of changing the type of binary scale 2^j, and dyadic translations of the mother wavelet, where a dyadic translation corresponds to a shift, k / 2j; value that is equal to a scale factor which is a multiple of a binary value (2,4,8,...) and therefore, the size of the wavelet, thereby obtaining the image adjustment. When working with images, the most important features for pattern recognition are the edges of the structures. A border can be defined as the set of points where the image has sharp transitions in intensity. However, not all variations of intensity can be defined as edges. Several variations of detection algorithms on images, such as the Canny algorithm [13] are equivalent to detecting a maximum DWT module dyadic bidimensional. For detecting image edges or irregularities, applies irregularities detector based on the exponents of Lipschitz [12].Thus, if f has a singularity at a point v, this means that it is not differentiable at v, and Lipschitz exponent at this point characterizes the singular behavior.

The Lipschitz regularity of edge points is derived from the maximum decrease of along DWT scales. In addition, approaches the image can be reconstructed from these high module without visual degradation. In two dimensions, we try to detect contours. For detection, the problem is the presence of noise. So, if we define the boundary from turning points, they will appear across the surface, due to noise. The application of the values for Lipschitz exponents can find and ratifying the highlighted areas like the edges obtained in step filtering Lipschitz regularity defines the upper limit with non-integer exponents. Thus, the DWT is a powerful tool to measure the minimum local regularity of the tool functions. However, it is not possible to analyze the regularity of f at a particular point v that will decrease from $|\hat{f}(w)|$, for high frequencies of ω. In contrast, as the wavelets are well localized in time, the DWT gives the Lipschitz regularity of intervals and points. The decrease in amplitude along DWT scales relates to Lipschitz regularity. Effective use of Lipschitz exponents can find these discontinuities in the image, which, as mentioned, are sometimes noisy areas, due to the nature of the image. These noisy areas are detected in the right places for concealment of information. Asymptotic decay measurement is equivalent to amplification of the image structures with a scale as it approaches zero. The singularities are detected by locating the maximum line (abscissa) upon which it converges to the maximum fine scales [11]. Finally, the signal $\psi_{j,n}(t)$ can be compressed or expanded in the time. This will have little certainly after effects in the plane of frequencies [2],

$$\psi\left(t\right) compresed \ by \ a \ factor \ 2^{j}\left(s\right)\psi_{s}\left(t\right) = \frac{1}{\sqrt{2^{j}}}\psi\left(\frac{t}{s}\right),$$

$$\hat{\psi}\left(w\right) compresed \ by \ a \ factor \ \frac{1}{2^{j}}\hat{\psi}_{2^{j}}\left(w\right) = \frac{1}{\sqrt{2^{j}}}2^{j}\hat{\psi}\left(2^{j}w\right) = \sqrt{2^{j}}\hat{\psi}\left(2^{j}w\right), \tag{16}$$

where $\hat{\psi}(w)$ represents the reconstruction of $\psi(t)$.

The discrete wavelet reconstruction can be computed by an inverse of the procedure of decomposition beginning at the level of resolution lower in the hierarchy. In applying the proposed steganographic algorithm to the sub-band LH is necessary to use a scaling factor that works with 24-bit RGB color images or Luminance, Chromatic blue, Chromatic red (YcbCr) or Hue, Value, Saturation (HSV) color model [14]; this scaling factor is closely related to energy conservation applied in the theory of wavelets. However, in the RGB color images, we propose the following scaling factor,

$$1 \big/ \sqrt{2^j} \, , \tag{17}$$

where j is directly dependent on the number of bits that integrates the image.

The proposed steganographic method works in the wavelet domain and provides an analysis of the wavelet coefficients in different decomposition scales to estimate the simple variance field to distinguish areas where the pixels are considered noisy [14]. We propose the following criterion: If the standard deviation of the current wavelet coefficient kernel is smaller than the threshold defined for the standard deviation global, then the respective area from the host image is considered noisy and then in such area, the hidden information can be inserted. Otherwise, the pixels from this area are considered free of noise and it is not possible to insert data of the hidden image. The criterion provides good invisibility for the hidden data and edges and results to fine detail preservation of the stego-image [14]. The standard deviation is computed using the following,

$$\sigma_k = \sqrt{\sum_{m=1}^{n} (y_m - \overline{y})^2 / n} \, , \tag{18}$$

where y_m is the m-th element of the host image, $\overline{y} = \sum_{m=1}^{n} y_m / n$ is the mean value of the current kernel, and $n = 9$ is the number of elements in the sample. The proposed steganographic method is depicted in Figure 3. This method is applied in each channel of RGB host image. From Figure 3, the block of redundancy of approaches, uses one level of decomposition with Haar wavelet. This algorithm smoothens the low frequencies of the host image through a double convolution operation (first of decomposition, and after reconstruction) of the coefficients and samples of host image [14], providing more hiding capacity and detail preservation of the proposed method. To hide the image, a double decomposition wavelet daubechies 4 (db4) is applied. To recover the hidden image, the algorithm of Figure 3 is used again but in the block of input changes to RGB stego-image and in the condition $\sigma_k < \sigma_g$ recovers the hidden data. Finally, the use of two levels of decomposition with db4 wavelet, and 3×3 kernel were found after numerous simulations under criteria peak signal noise ratio (PSNR), MAE (Mean Absolute Error), CORR (Correlation), NCD (Normalized Color Deviation), etc. [2,14].This criterion applied to each RGB channel is also applied to each channel for YCbCr color space and HSV, apply each threshold adjustment scale factor for reducing distortions in the image.
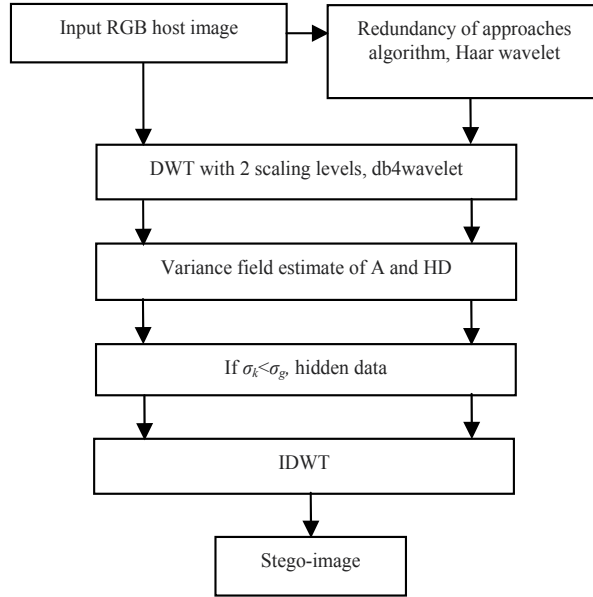
Figure 3. Proposed steganographic algorithm.

The threshold σ_g is used to select the pixel occupying the position where the data are hidden. This is done through [14],

$$\sigma_g = \sqrt{\sum_{m=1}^{N}(x_i - \overline{x})^2 / N} \ , \tag{19}$$

where x_i is the i-th element of the host image, $\overline{x} = \sum_{i=1}^{N} x_i / N$ is the mean value of the current host image, and N is the number of elements in the sample(host image). Adjusting for each expansion and contraction of the wavelet transform using Eq. 19; for each value of the weight function in the host image, pixels in each color space applied for demonstration of this threshold is observed, if the proposal is a valid consideration. The three goals of steganographic algorithms must be achieved: high capacity for integration, high quality of the stego-image and full recovery of the hidden information.

3. Theory/Calculations

In the optimization and evaluation of algorithms in digital image processing, the peak signal to noise relation (PSNR) is the criterion most frequently used to evaluate the quality of the imagery [2],

$$\text{PSNR} = 10 \quad \log_{10}\left[\frac{(255)^2}{\text{MSE}}\right]\text{dB}, \tag{20}$$

where $\text{MSE} = \frac{1}{M_1 M_2}\sum_{l=1}^{M_1}\sum_{m=1}^{M_2}\| y(l, m) - x(l, m)\|_{L_2}^2$ is the mean square error, M_1, M_2 are the image dimensions, l, m are the coordinates of the current position in the image, $y(l, m)$ is the 3D vector value of the pixel in the (l, m) location of the stego-image, $x(l, m)$ is the corresponding pixel in the original cover image, and $\| \cdot \|_{L_2}$ is the L2-vector norm.

The Normalized Color Deviation (NCD) is used for the quantification of the color perceptual error [2],

$$\text{NCD} = \frac{\sum_{l=1}^{M_1}\sum_{m=1}^{M_2}\left\|\Delta E_{Luv}(l,m)\right\|_{L_2}}{\sum_{l=1}^{M_1}\sum_{m=1}^{M_2}\left\|E_{Luv}^*(l,m)\right\|_{L_2}} \tag{21}$$

Here, $\| \Delta E_{Luv}(l, m) \|_{L_2} = [(\Delta L^*(l, m))^2 + (\Delta u^*)^2 + (\Delta v^*)^2]^{1/2}$ is the norm of the color error; ΔL^*, Δu^*, and Δv^* are the differences in the L^*, u^*, and v^* components, between the two color vectors that present the stego and cover image for each pixel (l,m) of an image, and $\| E_{Luv}^*(l, m) \|_{L_2} = [(L^*)^2 + (u^*)^2 + (v^*)^2]^{1/2}$ is the norm of the cover image pixel vector in the $L^* u^* v^*$ space. The quality index (Q) is provided to demonstrate the quality of the stego-images [2, 14], where $\bar{x}$ and $\bar{y}$ are the mean values of the cover and stego-image, respectively; σ_x^2 and σ_y^2 are the variances of the cover and stego-image, respectively, and $\sigma_{xy} = \frac{1}{NM}\sum_{l}^{N}\sum_{m}^{M}((x_{l,m} - \bar{x})(y_{l,m} - \bar{y}))$ is the correlation coefficient between cover image x and hide image y,

$$Q = \frac{4\sigma_{xy}\overline{xy}}{\left(\sigma_x^2 + \sigma_y^2\right)\left(\bar{x}^2 + \bar{y}^2\right)}, \tag{22}$$

The hiding capacity (HC) dictates the number of bits inserted in the host image [2,14],

$$HC = MSE \times \frac{number\ of\ samples\ in\ embedding\ band}{number\ of\ bits\ of\ secure\ data}. \tag{23}$$

We incorporate in the proposed scheme other color spaces such as YCbCr and HSV to ensure that the visual artifacts appearing in the stego-image are imperceptible, and the difference between the cover and stego-image is indistinguishable by HSV by using the proposed scaling factor. To verify and quantify the results obtained in this proposed steganographic algorithm,

the results obtained in conjunction with other spatial domain methods were compared with 4-3 LSB and the optimization of this algorithm.

Table 1 shows the performance results in terms of PSNR, MAE (Mean Absolute Error), CORR (Correlation), Q, NCD, HC, in the case of $j=2^8$ values in the scaling factor by using the 320 × 320 RGB color image "Mandrill" [15] as the host image and "Lena" [15] as the hidden image. In Table 1, we can see that the best result is presented by the steganographic method proposed here by applying the scale factor adjustment in the wavelet transform, the scale factor for this example has a value of $j = 2^8$. In Table 2, we can see the results of the image recovered "Lena" where you can see that the image quality index (Q) is close to 1, indicating that the recovered image is very close to the one inserted originally.

Criteria	Algorithms				
	4LSB	3LSB	4LSBO	3LSBO	Variance Field Simple Estimation
PSNR dB	36.168	36.169	30.111	30.112	37.283
MAE	2.9911	2.9902	9.7307	9.7315	1.2020
CORR	99.78	99.78	99.76	99.76	99.34
Q	0.9976	0.9976	0.9948	0.9948	0.9956
NCD	0.00073	0.00073	0.0022	0.0022	0.00030
HC (Kb)	51,200	38,400	51,200	38,400	76,800

Table 1. Comparative results for the stego-image "Mandrill" with the secret image "Lena"

Criteria	Algorithms				
	4LSB	3LSB	4LSBO	3LSBO	Variance Field Simple Estimation
PSNR dB	36.291	36.291	30.144	30.144	35.391
MAE	2.7479	2.7479	8.1255	8.1255	2.9409
CORR	99.55	99.55	99.54	99.54	99.30
Q	0.9962	0.9962	0.9943	0.9943	0.9950
NCD	0.0020	0.0020	0.0033	0.0033	0.0019

Table 2. Comparative results for the retrieved secret image "Lena"

In Table 3, we show the results obtained from the proposed steganographic algorithm with a scaling factor, with j = 10. We note that PSNR improves by more than 1dB, and conserves the

Q index on the recovered image. The PSNR value is enhanced for each of the cases in color spaces, and so it may be said that the energy distribution (inserted data) within the image is homogeneous, thus wanting to be approached by a stego-analyzer to retain a uniform distribution histogram, removing any suspicion of being a carrier of information. In Table 3, we can see that the model of color HSV offers better quality in the stego-image in contrast to the RGB and YCbCr models; nevertheless, the capacity of insertion is lost. It is possible to observe that the model RGB offers good results and the capacity of insertion does not sacrifice itself.

Host image "Mandrill"	Hidden image "Lena"
RGB color model	
Q=0.9999	Q=0.9962
PSNR=39.1233 dB	PSNR=37.5167 Db
COI=99.34%	COI=99.55%
NCD=6.0486 e-4	NCD=0.0020
MAE=1.7022	MAE=2.7714
HC=25.65Kb	
YCbCr color model	
Host image "Mandrill"	Hidden image "Lena"
Q=0.9888	Q=0.9962
PSNR=30.3913Db	PSNR=36.0827 dB
COI=98.92%	COI=99.54%
NCD=9.5940 e-4	NCD=0.0020
MAE=2.2044	MAE=2.7948
HC=2.18Kb	
HSV color model	
Host image "Mandrill"	Hidden image "Lena"
Q=0.9999	Q=0.9962
PSNR=41.3900 dB	PSNR=36.1233 dB
COI=99.92%	COI=99.55%
NCD=2.8906 e-4	NCD=0.0020
MAE=0.6401	MAE=2.7714
HC=0.068Kb	

Table 3. Performance results in different color models for j=10 in the scaling factor.

We also present the error images in Figure 4 presents the visual results according with Table 3.
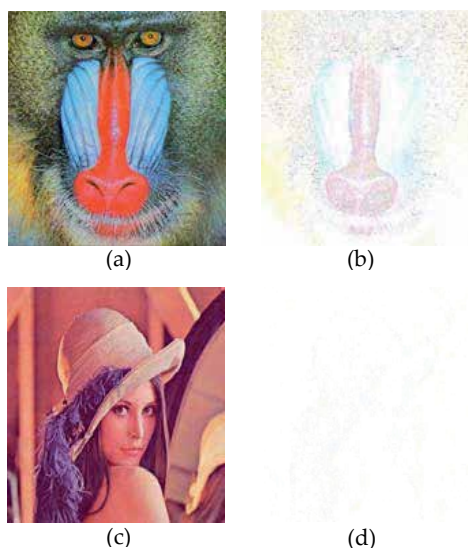
Figure 4. Visual results in the case of j=10, (a) stego-image "Mandrill", (b) error stego-image "Mandrill", (c) hide image "Lena", (d) error hide image "Lena".

4. Discussions

The results only apply steganographic algorithm have shown visual defects, which may cause some suspicion that this is a carrier of information added to this. However, applying the scaling factor, better visual and quantitative results also overcoming the stego-image are obtained. Significantly, a steganographic algorithm must meet the following criteria: Total recovery of the embedded information; good quality of the cover image and the recovered image; and high insertion capability. Finally, in this work, the proposed method yielded better results, with the best result obtained using the scaling factor $j = 10$. The following are the results: PSNR = 41.3900dB, NCD = 2.8906 e-4, MAE = 0.6401, HC = 0,068e3Kb and Q = 99.99% in the cover image. We can also observe that applying the scale factor, the wavelet contraction and expansion is set as close to the original contour of the image, thus, making the data inserted into the noisiest areas of the image; and this is imperceptible to the human eye.

5. Conclusions

The RGB, HSV and YCbCr color model images are altered in their energy contribution in each sub-matrix of the wavelet decomposition when the steganographic algorithm is applied. From equations 5, 6 and 14, we propose the use of the scaling factor for adjusting filtered images with DWT. This adjustment will be made to each pixel of the image to achieve the three

objectives of steganographic algorithms. For steganographic applications, the digital filter helps to locate areas suitable for inserting information without it becoming visible to the human eye. This filter is generally altered in their energy contribution in each sub-matrix of wavelet decomposition when a steganographic algorithm is applied. It is known that the value of $1/\sqrt{2}$ is the key factor in the value adjustment of the wavelets energy, the value adjustment has been applied only in grayscale image tests. To apply the proposed scaling factor $1/\sqrt{2^{\,j}}$ in RGB color images, there is a value adjustment factor for the energy input in each sub-matrix. It is also noted that when changing the value of j, it adjusts the sharpness and image quality providing a visible improvement of the image, as shown in Tables 1, 2 and 3, and in the subjective results. From Table 3, more security options are given for the insertion of information that is highly confidential; each color space provides particular characteristics that can be exploited for sending such information.

Acknowledgements

Author details

Blanca Esther Carvajal-Gámez[1,2*], Erika Hernández Rubio[2*] and Amilcar Meneses Viveros[3]

*Address all correspondence to: becarvajal@ipn.mx; ehernandezru@ipn.mx

1 Instituto Politécnico Nacional, Unidad Profesional Interdisciplinaria de Ingeniería y Tecnologías Avanzadas, México

2 Instituto Politécnico Nacional, Escuela Superior de Computo, Sección de Estudios de Posgrado e Investigación Juan de Dios Batiz s/n Professional U. Adolfo López Mateos,, México

3 Centro de Investigación y de Estudios Avanzados del IPN, Departamento de Computación, San Pedro Zacatenco, México

References

[1] Chia-Chen, L., Wei-Liang, T., Chin-Chen C.: Multilevel reversible data hiding based on histogram modification of difference. Pattern Recognition. 3582- 3591 (2008).

[2] Carvajal-Gámez B. E., Gallegos-Funes F. J., Rosales-Silva A. J. and López-Bonilla J. L., Adjustment of energy with compactly supported orthogonal wavelet for stegano-

graphic algorithms using the scaling function, $1/\sqrt{2}^j$, International Journal of Physical Sciences, 2013, vol. 8(4), 157-166, DOI: 10.5897/IJPS12.516.

[3]   Wang J., Steganography of capacity required using modulo operator for embedding secret image, (2005), Applied Mathematics and Computation.164: 99–116.

[4]   Wu D, Tsai W., A steganographic method for images by pixel value differencing, (2003), Pattern Recognition Letters. 24:1613–1626.

[5]   Chan C. K., Cheng L. M., Hiding data in images by simple LSB substitution, Pattern Recognition, vol. 37(2004), 469-474.

[6]   Reddy, A. A., Chatterji, B. N.: A new wavelet based logo-watermarking scheme, (2005), Pattern Recognition Letters. 1019-1027.

[7]   Mielikainen J., LSB matching revisited, (2006), IEEE Signal Processing Letters. 13: 285–287.

[8]   Zhang X., Wang S., Steganography using multiple-base notational system and human vision sensitivity, (2005), IEEE Signal Processing Letters.12: 67–70.

[9]   Gao R. X.,Yan R., Wavelets: Theory and Applications for Manufacturing, Springer Science+Business Media, (2011), pp:17-34.

[10] Walker J, A primer on wavelets and their scientific applications,(2003), Chapman & Hall/CRC, London.

[11] Vetterli M., Kovacevic J., Wavelets and Subband Coding, (2007), second edition. http://waveletsandsubbandcoding.org/Repository/VetterliKovacevic95_Manuscript.pdf.

[12] Besov O. V., Interpolation, Embedding, and Extension of Spaces of Functions of Variable Smoothness,(2005), Proceedings of the Steklov Institute of Mathematics, Vol. 248, 2005, pp. 47–58.

[13] Canny, J., A Computational Approach To Edge Detection, IEEE Trans. Pattern Analysis and Machine Intelligence, 8(6):679–698, 1986.

[14] Carvajal-Gamez B. E., Gallegos-Funes F. J., Rosales-Silva A. J., Color local complexity estimation based steganographic (CLCES) method, (2013), Expert Systems with Applications 40, (2013), 1132–1142.

[15] Data Base Images of the University of Southern of California, (2012), Signal and Image Processing Institute. USC VITTERBI. http://sipi.usc.edu/database/database.php (2015).

Wavelet-Based Analysis of MCSA for Fault Detection in Electrical Machine

Mohammad Rezazadeh Mehrjou, Norman Mariun, Mahdi Karami,
Samsul Bahari Mohd. Noor, Sahar Zolfaghari, Norhisam Misron,
Mohd Zainal Abidin Ab. Kadir, Mohd. Amran Mohd. Radzi and
Mohammad Hamiruce Marhaban

Additional information is available at the end of the chapter

Abstract

Early detection of irregularity in electrical machines is important because of their diversity of use in different fields. A proper fault detection scheme helps to stop the propagation of failure or limits its escalation to severe degrees, and thus it prevents unscheduled downtimes that cause loss of production and financial income. Among different modes of failures that may occur in the electrical machines, the rotor-related faults are around 20%. Successful detection of any failure in electrical machines is achieved by using a suitable condition monitoring followed by accurate signal processing techniques to extract the fault features. This article aims to present the extraction of features appearing in current signals using wavelet analysis when there is a rotor fault of eccentricity and broken rotor bar. In this respect, a brief explanation on rotor failures and different methods of condition monitoring with the purpose of rotor fault detection is provided. Then, motor current signature analysis, the fault-related features appeared in the current spectrum and wavelet transform analyses of the signal to extract these features are explained. Finally, two case studies involving the wavelet analysis of the current signal for the detection of rotor eccentricity and broken rotor bar are presented.

Keywords: Wavelet transform, Line start permanent magnet motor, Induction motor, Eccentricity, Broken rotor bar

1. Introduction

Electrical machines are widely used for many industrial processes and play a non-substitutable role in a variety of industries [1–2]. In spite of their reliability and robustness, electrical

machines are still prone to failures due to the exposure to a wide diversity of strict conditions and environments, incorrect operations, or even manufacturing defects [3]. These faults, gradual deterioration, and failures can lead to motor interruption, if left undetected, and their resulting unplanned downtime is very expensive. Early detection of irregularity in electrical machines with proper fault diagnosis schemes will help prevent high-cost failures, thereby decreasing the cost of maintenance and preventing unscheduled downtimes. However, stopping the propagation of the fault limits its escalation to severe degrees, which results in loss of production and financial income.

The fault identification schemes are basically based on data collection of electrical machines followed by signal processing. The condition of an electrical machine is examined from data that are acquired through sensors and supportive equipment methods. By using a suitable signal processing technique, each fault can be then detected via a specific feature present in the measured signal of a faulty motor when compared to a fault-free one. Hitherto, a number of data acquisition techniques, which display a certain parameter of the electrical machine, have been established. Essentially, the efficiency of a data acquisition method is characterized by its accuracy, cost, and importantly its capability to quantify the fault. On the contrary, condition monitoring based on data acquisition techniques requires the user to have adequate knowledge and proficiency to differentiate a normal operating condition from a potential failure state. The key step, but a difficult task, in the fault detection of electrical machines is to extract the fault-related features from the acquired signal and identify the condition of motor. Fault-related features are parameters derived from the acquired data that specify the existence of failure in device. The current signal of electrical machine is non-linear and non-stationary with strong noise interference; hence, the energy of early signal is too low to extract fault-related features in time domain [4]. Advanced signal processing methods based on analysis of time–frequency domain have been proposed as effective approaches for fault detection in electrical machines [5].

The focus of this chapter is on the extraction of features present in the current spectrum of electrical machine when one of two important rotor faults, eccentricity and broken rotor bar, exists. To extract features from the current spectrum in the presence of these faults, an advanced signal processing method, wavelet packet analysis, is used. In this regard, the fundamentals related to the detection of these two faults using wavelet packet analysis of current signal are explained in the following sections.

2. Rotor faults

From the investigations on different failure modes in electrical machines, the rotor-related faults are around 20% of failures may happen in the motor [6]. The rotor is exposed to different types of stresses that seriously affect its normal condition and subsequently create faults in it. Bonnett and Soukup explained the stresses that motors are subjected to and their unfavourable causes [7]. Failures in rotor are classified into eccentricity of rotor, crack and/or breakage of rotor cage bars, and crack and/or breakage of end rings and rotor bow [8]. These irregularities

bring specific secondary failures that cause serious faults in electrical machines. Moreover, these types of faults may not show any symptoms during early stage until propagating to the next step and leading to the sudden collapse [9–11]. In recent years, rotor faults have been increasingly studied for developing advanced techniques that permit online early detection and diagnosis of motor faults to avoid any negative consequences of unexpected shutdowns, but this area still needs more research because of the complexity of the motor during the runtime. In this section, a brief description of different rotor faults is provided.

2.1. Rotor eccentricity

In a fault-free machine, the rotor is centre aligned in the stator bore that results in uniform air gap between the stator and rotor. In fault-free electrical machines, the rotation centre of the rotor is the same as the geometric centre of the stator bore. As a result, the rotor symmetrical axis (C_r), stator symmetrical axis (C_s), and rotor rotational axis (C_g) coincide with each other, and thus the magnetic forces are balanced in opposite directions. Rotor eccentricity, displacement of the rotor from its centred position in the stator bore, generates an asymmetric air gap between the stator and rotor [12]. The rotor eccentricity also produces unbalanced magnetic pull (UMP), which is a radial magnetic force on the rotor shaft. The UMP also pulls away the rotor from the stator bore centre, thus causing excessive stress on the electrical machine [13, 14]. Eccentricity commonly presents in rotating electrical machines, and the maximum permissible level of eccentricity is defined, which is 5 or 10% of the air-gap length [15]. If eccentricity exceeds the permissible level, it will increasingly damage the winding, stator core and rotor core in the motor due to rubbing of the stator with the rotor [12, 14]. Three different types of eccentricity occur in an electrical machine: static eccentricity, dynamic eccentricity, and mix eccentricity. As an example, static eccentricity is explained next.

Static eccentricity in electrical machines occurs when the rotor symmetrical axis is concentric with the rotor rotational axis; however, they are dislocated with respect to the stator symmetrical axis; hence, the position of minimum radial air-gap length is fixed. In this state, the mutual inductances across the stator and rotor as well as the self- and mutual inductances among the rotor phases are related to the angular position of the rotor [16]. The implication of static eccentricity fault in motor is depicted in Figure 1.

Static eccentricity can be due to numerous motives such as elliptical stator core, wrong placement of the rotor or stator at the setup or subsequent of maintenance, incorrect bearing positioning, bearing deterioration, shaft deflection, housing imperfection, end-shield misalignment, excessive tolerance, and rotor weight or pressure of interlocking ribbon [17–19]. Static eccentricity leads to second failures which cause drastic harm to the rotor, stator core and windings. The radial forces in the static eccentricity condition produce a steady UMP in the radial route across the motor because the reluctance of the magnetic flux path decreases with the transmission of flux on the side of tiny air gap [20]. Albeit, the winding current induces more magnetic flux that causes a stronger pull and leads to the expansion of the air gap on the opposite side where the reluctance increases, thereby decreasing the flux and magnetic side pull. Therefore, the UMP compels the rotor to move toward the area of the narrowest air-gap length. During abrasion, the stator core subsequently generates abnormal vibration and

severely damages the rotor, windings and the stator [7]. Consequently, the static eccentricity causes acoustic noise, premature failure in the bearing, rotor deflection and bent rotor shaft.
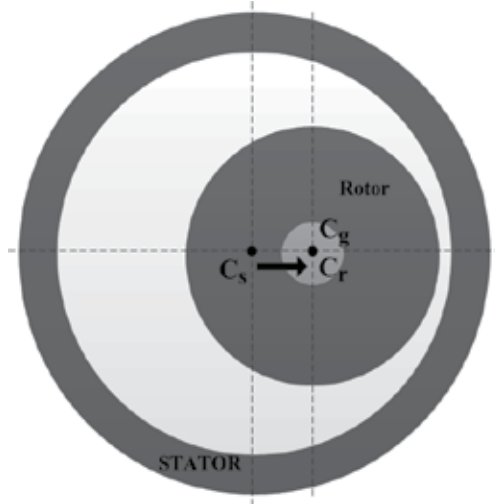
Figure 1. Cross section of motor under static eccentricity fault

The degree of static eccentricity is calculated by the equation based on Figure 2 [16]:

$$D_{SE} = \frac{\left| \overrightarrow{C_s C_g} \right|}{g} \tag{1}$$

where $\overrightarrow{C_s C_g}$ is the vector of static transfer which is invariant for rotor angular positions and g is the uniform air-gap length.
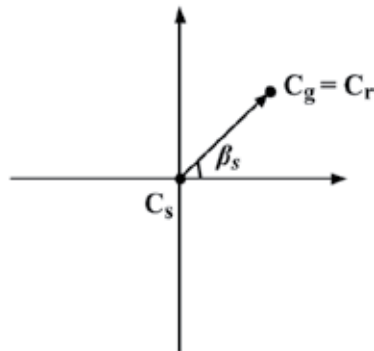
Figure 2. Location of stator and rotor under static eccentricity condition

2.2. Rotor bar breakage

The breakage of rotor bars is one of the important failures in the rotor cage of electrical machines. During the operation of electrical machines, rotor bars may be broken partially or completely. The main reasons for bar breakage include electrical, mechanical, and environmental stresses during the operation of electrical machines and/or improper design of rotor geometry. Once a bar breaks, the stress increases and deteriorates the condition of the neighbouring bars progressively. Such a destructive process can be prevented, if any crack in the bar is detected early [21]. Typical causes of rotor bar breakage are referred as follows [22]: high thermal and mechanical stresses, direct online starting duty cycles for which the rotor cage was not well designed to endure against the stresses, imperfections in design and fabrication process of the rotor cage bars. Any failure in rotor bars itself causes unbalanced currents and torque pulsation and, therefore, decreases the average torque [23].

The rotor bars are short-circuited on both sides of the rotor by end rings. Depending on the type of squirrel cage in the motor, the source of failures in the end ring differs, in die-cast aluminium rotors caused by porosity of casting and in fabricated rotor cages caused by poor end-ring joints during manufacturing. Once the preliminary failure occurs, localized heat may extend to the rotor cage excessively. Therefore, the fault propagation is continued by multiple start-ups similar to load variations, which create high centrifugal forces. Accordingly, end-ring faults cause a drastic increase in the current and speed fluctuation [21].

2.3. Rotor bow

Any irregular thermal variation (heating or cooling) and unfavourable thermal distribution of the rotor during operation of electrical machines may bow the rotor [24]. The bow created in the rotor prevents sufficient alignment in the motor and generally produces a preload on the bearings. Bend locations in the rotor cause major failures in other parts of the motor [25]. The bow in the rotor is classified as local and extended [24]. When an asymmetrical heating is confined to a part of the rotor, a local bow is generated. For example, rotor-to-stator rubbing can generate a local asymmetric thermal distribution, which causes the local bow. When an asymmetrical heating extends along the rotor, an extended bow is generated. Long-lasting gravity effects on off-line machines generate rotor bow classified as an extended bow, when unsuitable rotor straightening turning system is not used [24]. Since the rotor is limited by two bearings, extended bow commonly causes a shaft bow [24].

3. Condition monitoring techniques for rotor fault detection

Condition monitoring programme which can predict a failure in electrical machines has received considerable attention for many years [2, 8]. Successful detection of any failure in electrical machines is achieved by using suitable condition monitoring. When a failure occurs, some machine parameters are exposed to changes that depend upon the fault degree. Any irregularity in the rotor of electrical machines presents with variation distributed in the rotor currents. The feedback of these currents to the air-gap field produces specific signatures of fault in the spectrum of speed, torque, current, and power. Reliable condition monitoring

techniques depend on the best understanding of the mechanical and electrical characteristics of the electrical machines in both fault-free and faulty situations. Researchers have used different condition monitoring techniques that can be categorized as follows [8]:

- Acoustic emission

- Air-gap torque

- Current

- Electromagnetic field monitoring

- Induced voltage

- Instantaneous angular speed

- Motor circuit analysis

- Power

- Surge testing

- Vibration

- Voltage

3.1. Motor current signature analysis

The drowned current signal by an electrical machine contains a single component. Any magnetic or mechanical asymmetries in the machine generate other frequency components in the stator current spectrum. These frequency components are diverse according to each specific fault in the machine.

Motor current signature analysis (MCSA) analyses the stator current signal to identify the presence of any failure in electrical machines. This analysis method has been introduced as an effective way for monitoring electrical machines for many years [8]. From all these methods suggested in the literature, MCSA is a forerunner because of its advantages [10, 13, 26–28]:

- Online monitoring characteristics

- Remote monitoring ability

- Non-invasive feature

- Inexpensive equipment and easy measurement

- Different fault detection capability (such as broken rotor bars, air-gap eccentricity, stator faults, etc.)

- Early-stage fault detection

- Highly sensitive

- Selective

When a failure is generated in the electrical machine, depending on the severity of this fault, some of the machine parameters change. For instance, the current spectrum of an ideal electrical machine contains a single component corresponding to the supply frequency. Any asymmetry in electrical machine causes other components to appear in a spectrum of stator current. When a rotor bar breaks, current does not flow through it, and hence no magnetic flux is created around the breakage bar. Therefore, there is no non-zero backward rotating field that rotates at the slip frequency speed with respect to the rotor. This asymmetry in the magnetic field of rotor induces harmonics in stator windings, which are superimposed on it. These superimposed harmonics appear at frequency spectrums as described in

$$f_{\text{BRB}} = \begin{bmatrix} 1 \pm 2\text{KS} \end{bmatrix} f_{\text{S}} \qquad (2)$$

where f_{BRB} is the harmonic component due to broken rotor bar, S is the slip, f_{S} is the fundamental frequency, and $k = 1, 2,...$ [29].

Any asymmetry caused by static eccentricity produced other components that appear in the spectrum of stator current. The characteristic frequency component associated with static eccentricity is located according to Eq. (3) [16]:

$$f_{\text{static}} = \begin{bmatrix} 1 \pm \dfrac{m}{p} \end{bmatrix} f \qquad (3)$$

where f_{static} is the harmonic component due to static eccentricity in line start permanent magnet synchronous motor (LSPMSM), m is an odd integer value, p is the number of pole pair, and f is the line frequency.

4. Wavelet

Frequency domain analysis is not reliable for fault detection because some outside parameters can affect the location and amplitude of fault-related feature. This parameter can be classified as follows: first, the fault frequency components depend on the slip of the motor; second, the fault feature amplitude is load dependent; third, the frequencies of the fault components are affected by voltage fluctuations; and fourth, long sampling interval is needed for a high-resolution frequency. Therefore, in general, frequency domain analyses are suitable for the steady-state situation. The problem involved in the analysis of non-stationary signals can be shunned by time–frequency analysis of the signal, which illustrates the signal in three-dimensional axis as time, frequency, and amplitude. The most popular time–frequency representations include Wigner–Ville distribution, short-time Fourier transform, and wavelet transform.

Wavelet transform expresses a signal in oscillatory function series at different frequencies and time. Wavelet transform divides the original signal into time-scale space, where the dimension of windows at time and scale (frequency) is not rigid [30]. Therefore, in fault diagnostics domain, wavelet transform has been used to extract the dominant features from original signals [31]. Various types of wavelet transforms have been widely used in the condition monitoring of electrical machine. Among all these techniques, discrete wavelet transform and wavelet packet transform (WPT) are the most common ones, explained in the following.

4.1. The principle of discrete wavelet decomposition

Discrete wavelet transform is based on signal analyses using a minor set of scales and specific number of translations at each scale. Mallat (1989) introduced a practical version of discrete wavelet transform called wavelet multi-resolution analysis [32]. This algorithm is based on the fact that one signal is disintegrated into a series of minor waves belonging to a wavelet family.

A discrete signal $f[t]$ could be decomposed as

$$f\left[t\right] = \sum_{k} A_{m0,n} \phi_{m0.n}\left[t\right] + \sum_{m=m0}^{m-1} \sum_{n} D_{m,n} \psi_{m,n}\left[t\right]$$

(4)

where ϕ is the scaling function (father wavelet) and ψ is the wavelet function (mother wavelet), A is the approximate coefficient and D is the detail coefficient.

The multi-resolution analysis commonly uses discrete dyadic wavelet, in which positions and scales are based on powers of two. In this approach, the scaling function is depicted by the following equation:

$$\phi_{m0,n}\left[t\right] = 2^{m0/2} \phi\left(2^{m0} t - n\right)$$

(5)

that is, $\phi_{m0,n}$ is the scaling function at a scale of 2^{m0} shifted by n. Wavelet function is also defined as

$$\psi_{m,n}\left[t\right] = 2^{m/2} \psi\left(2^{m} t - n\right)$$

(6)

that is, $\psi_{m,n}$ is the mother wavelet at a scale of 2^{m} shifted by n.

Generally, approximate coefficients $A_{m0,n}$ are obtained through the inner product of the original signal and the scaling function

$$A_{m0,n} = \int_{-\infty}^{\infty} f(t)\phi_{m0.n}(t)dt \tag{7}$$

The approximate coefficients decomposed from a discretized signal can be expressed as

$$A_{(m+1),n} = \sum_{n=0}^{N} A_{m,n} \int \phi_{m.n}(t)\phi_{m+1.n}(t)dt = \sum A_{m,n}.g[n] \tag{8}$$

In the dyadic approach, the approximation coefficients $A_{m0,n}$ are at a scale of 2^{m0}. The filter, $g[n]$, is a low-pass filter. Similarly, the detail coefficients $D_{m,n}$ can be generally obtained through the inner product of the signal and the complex conjugate of the wavelet function:

$$D_{m,n} = \int_{-\infty}^{\infty} f(t).\psi_{m,n}^{*}(t)dt \tag{9}$$

The detail coefficients decomposed from a discretized signal can be expressed as

$$D_{(m+1),n} = \sum_{n=0}^{N} A_{m,n} \int \phi_{m.n}(t).\psi_{m+1.n}(t)dt = \sum A_{m,n}.h[n] \tag{10}$$

In the dyadic approach, $D_{m,n}$ are the detail coefficients at a scale of 2^{m0}. The filter, $h[n]$ is a high-pass filter.

The multi-resolution analysis utilizes discrete dyadic wavelet and extract approximations of the original signal at different levels of resolution. An approximation is a low-resolution representation of the original signal. The approximation at a resolution 2^{-m} can be split into an approximation at a coarser resolution 2^{-m-1} and the detail. The detail represents the high-frequency contents of the signal. The approximations and details can be determined using low- and high-pass filters. In the multi-resolution analysis, the approximations are split successively, while the details are never analysed further. The decomposition process can be iterated, with successive approximations being decomposed in turn; hence one signal is broken down into many lower-resolution components. This process is called the wavelet decomposition tree as shown in Figure 3. It illustrates the dyadic wavelet decomposition algorithm regarding the coefficients of the transform at different levels according to the description by Polikar et al. (1998) [33].
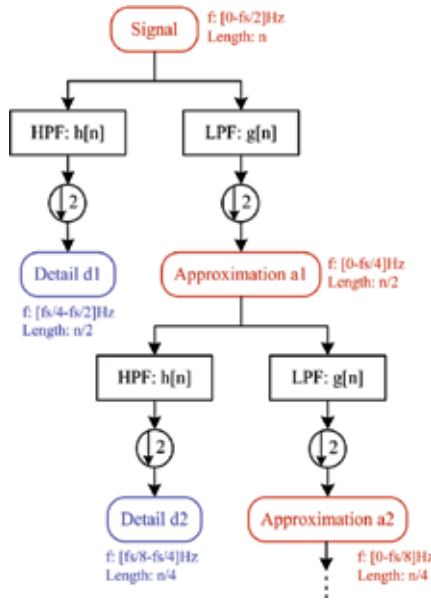
Figure 3. Dyadic wavelet decomposition algorithm [34].

4.2. The principle of wavelet packet decomposition

The wavelet packet transform is a direct expansion of discrete wavelet transform, where the details as well as approximation are split up. Therefore, this tree algorithm is a full binary tree that offers rich possibilities for signal processing and better signal representation in comparison to a discrete one.

A wavelet packet function has three naturally interpreted indices in time–frequency functions:

$$\psi_{j,k}^{i} = 2^{\frac{j}{2}} \psi^{i}\left(2^{j} t - k\right), \; i = 1, 2, 3, \ldots \tag{11}$$

where integers j, k, and i are called the scale, translation, and simulation parameters, respectively. Scaled filter $h(n)$ and the wavelet filter $g(n)$ are quadrature mirror filters associated with the scaling function $\Phi(t)$ and the wavelet function $\psi(t)$ [32]. The conjugate mirror filters h and g with finite impulse responses (FIRs) of size k can define the fast binary wavelet packet decomposition (WPD) algorithm of the signal $f(t)$:

$$\begin{cases} d_0^0(t) = f(t) \\ d_{j+1}^{2n}(t) = \sum_k h(k - 2t) d_j^i \; i = 0, 1, \ldots, 2^j - 1 \\ d_{j+1}^{2n+1}(t) = \sum_k g(k - 2t) d_j^i \end{cases} \tag{12}$$

The wavelet packet component signals $f_j^i(t)$ are produced by a combination of wavelet packet function $\psi_{j,k}^n(t)$ as follows:

$$f_j^i(t) = \sum_{i=1}^{2j} C_{j,k}^i(t)\psi_{j,k}^i(t) \tag{13}$$

where the wavelet packet coefficients $C_{j,k}^i(t)$ are calculated by

$$C_{j,k}^i(t) = \int_{-\infty}^{\infty} f(t)\psi_{j,k}^i(t)dt \tag{14}$$

Provided the wavelet packet functions are orthogonal

$$\psi_{j,k}^m(t)\psi_{j,k}^n(t) = 0 \text{ if } m \neq n \tag{15}$$

As data sets of wavelet packet coefficients increase in size, the energy principle is applied to current signals after WPT for fault location estimation [35].

4.3. A review of wavelet decomposition for fault detection

Different types of wavelet transform techniques have been widely used in algorithms designed for fault detection in electrical machines. Table 1 presents the common types of these techniques.

Ref	Year	Diagnostic Monitoring Techniques (MTs)	Signal Processing	Classifier and Decision-making Tool	Purpose	Achievement and Limitation
[5]	1996	Current (start-up)	short time fourier transform(STFT), continuous wavelet transform(CWT), Wigner distribution		To compare individual signal processing techniques using both test and actual data	The CWT has been proven to be the most efficient technique for the extraction of the frequency component of interest. Limitation: available. The technique would be of particular use to industrial applications where motors are frequently started on no load, or have been moved to a workshop environment where

Ref	Year	Diagnostic Monitoring Techniques (MTs)	Signal Processing	Classifier and Decision-making Tool	Purpose	Achievement and Limitation
						fully loaded conditions are neither practical nor achievable
[36]	2001	Motor current signature analysis (MCSA)	Discrete wavelet transform (DWT)	-	To develop current monitoring procedure for BRB detection	A new approach in detection of BRB having only stator current signal
[37]	2002	MCSA	WT,park transform(PT)	-	To compare model-based and signal-based approaches based on Park transform for BRB detection	The spectral decomposition obtained by the wavelet transform may be used to isolate different kinds of faults
[38]	2002	MCSA, voltage, speed	Wavelet packet decomposition (WPD)	Artificial neural network	To develop a model-based diagnosis system for detection of various faults including BRB	The proposed system was shown effective in detecting early stages of different IM faults
[39]	2003	MCSA	WPD	Artificial neural network	To improve MCSA monitoring procedure for BRB and air-gap eccentricity detection	It provides feature representations of multiple frequency resolutions for faulty modes
[40]	2004	Current (start-up)	DWT	-	To improve the start-up current monitoring procedure for BRB detection using a filter that actively tracks the changing amplitude, phase and frequency to extract the fundamental from the transient	This method does not require parameters such as speed or number of rotor bars. It is not load dependent and can be applied to IMs that operate continuously in the transient mode
[41]	2005	MCSA	fast fourier transform (FFT), WPD	-	To improve MCSA monitoring procedure for the detection of various faults including BRB	The features of BRB and static eccentricity yield similar results in the wavelet analysis, but are different in Fourier analysis. Therefore the use of both types of analysis together can distinguish the faults

Ref	Year	Diagnostic Monitoring Techniques (MTs)	Signal Processing	Classifier and Decision-making Tool	Purpose	Achievement and Limitation
[42]	2005	Current (start-up)	DWT	-	To develop start-up current monitoring procedure for BRB detection	The method is not load dependent and can be effective on small lightly loaded machines
[43]	2005	Current (envelope, start-up)	CWT	-	To develop start-up current monitoring procedure using envelope extraction of current spectrum for BRB detection	The procedure is not affected by other factors such as initial rotor position, phase of the supply and supply imbalance. It is able to classify the different degrees of BRB. Limitation: A partial BRB could not be indicated
[44]	2006	MCSA	WPD	Adaptive neuro-fuzzy	To present a novel online diagnostic algorithm for BRB and air-gap eccentricity detection in variable speed drive systems	Although the algorithm is able to detect the fault with high accuracy, the number of training iterations and the CPU processing time were reduced
[45]	2006	Instantaneous power	DWT	-	To improve IP monitoring for BRB detection under various load levels	Wavelet approach applied to IP showed superior ability for BRB detection compared to the frequency domain analysis
[46]	2006	MCSA	FFT, WPD	Fuzzy entropy–artificial neural network	To improve MCSA monitoring procedure for the detection of various faults including BRB	An approach was proposed based on Fourier transformation and wavelet transform and neural network system to classify the faults
[47]	2006	Current (start-up)	DWT	-	To develop start-up current monitoring procedure for BRB detection. To compare the influence of the discrete wavelet transform parameters (type of mother wavelet, order of the mother wavelet, sampling rate	The tests show that if the start-up transient is not very short, the reliability of the proposed method for BRB detection is similar to that of the classical approach, based on the Fourier transform, in the case of loaded motors. In addition, the method can detect faults in an unloaded condition, and it

Ref	Year	Diagnostic Monitoring Techniques (MTs)	Signal Processing	Classifier and Decision-making Tool	Purpose	Achievement and Limitation
					or number of levels of the decomposition) over the diagnosis	allows a correct diagnosis of a fault-free machine in some particular cases where Fourier analysis leads to an incorrect fault diagnosis
[48]	2007	Induced voltage	FFT, WT	-	To investigate the limitations and harmonics of the induced voltage after supply disconnection harmonics for BRB detection	Fourier transform did not provide information about fault severity and load variations. A method based on wavelet analysis of induced voltage spectrum was developed for BRB detection Limitation: Tests need to be carried out for fault-free motor to develop a baseline response. It is sensitive to changes in load, system inertia, rotor temperature and supply voltage
[49]	2007	MCSA	WPD	-	To detect incipient bearing fault via stator current analysis	Cover better analysis under various conditions and more tolerant frequency bands with WPD method
[50]	2007	MCSA	WPD	-	To detect real-time fault for various disturbances in three-phase IM	Selecting the optimal levels of decomposition and optimum mother wavelet
[51]	2008	MCSA	STFT, WT	-	To improve MCSA monitoring procedure for BRB and stator shorted turns detection	Wavelet decomposition is superior to STFT. Power spectral density for wavelet details was introduced as a merit factor for fault diagnosis. The proposed method can diagnose shorted turns and BRB in non-constant load–torque IM applications
[52]	2008	Current (start-up)	DWT	Principle component	To develop transient current monitoring	Feature reduction and extraction using component

Ref	Year	Diagnostic Monitoring Techniques (MTs)	Signal Processing	Classifier and Decision-making Tool	Purpose	Achievement and Limitation
				analysis (PCA), kernel PCA, support vector machine	procedure; uses intelligent system for detection and classification of various faults including BRB	analysis via PCA and KPCA are highlighted. The performance of WSVM is validated by applying it to fault detection and classification of induction motor based on start-up transient current signal. Limitation: A proper pre-processing for the transient current signal is needed to improve the emerging salient differences between conditions in induction motors
[35]	2008	MCSA	WPD	Artificial neural network	To estimate transmission line fault	A powerful and reliable method by applying the energy criterion after wavelet packet transform (WPT) for reducing the data size
[53]	2009	MCSA	WPD	Artificial neural network	To propose a novel online diagnosis algorithm for BRB detection	The diagnosis can be performed with reduced load condition. An accurate measurement of the slip speed is not necessary
[54]	2009	Current (start-up)	DWT	-	To develop start-up current monitoring procedure for distinguishing various faults including BRB and other phenomena, such as load–torque oscillations	The proposed methodology showed promising ability for the reliable discrimination of simultaneous electromechanical faults and the diagnosis of faults combined with other phenomena
[55]	2009	Current (envelopes)	DWT	-	To propose a new technique, slip independent, for BRB detection under different load levels	The proposed method gives the same reliable results for BRB detection under different load levels when applying to the stator-current space–vector magnitude and the

Ref	Year	Diagnostic Monitoring Techniques (MTs)	Signal Processing	Classifier and Decision-making Tool	Purpose	Achievement and Limitation
						instantaneous magnitude of the stator-current signal
[56]	2009	Vibration	WPD	Artificial Neural Network	To optimize gear failure identification using GAs and ANNs	The technique determines the best values 'mother wavelet', 'decomposition level' and 'number of neurons in hidden layer'
[57]	2009	Vibration	WPD	Hybrid support machine	To propose an intelligent method to diagnose rotating machinery failures	An accurate and quick fault-type estimation method by applying hybrid SVM to the energy criterion after WPA
[58]	2009	MCSA	DWT	-	To compare a different wavelet family for BRB fault detection	The technique determines the best mother wavelet
[59]	2010	MCSA	WT,PSD	-	To develop BRB detection methods based on MCSA	The method has the ability to detect BRB for both constant torque and for variable load torque
[60]	2011	MCSA	FFT,WT	-	To propose a new method for early fault detection	The approach has been proved to be effective to detect failures in its very early stages
[4]	2012	Vibration	WPD,EMD	Artificial neural network	To integrate the fine resolution advantage of WPD with the self-adaptive filtering characteristics of empirical mode decomposition (EMD) to early fault diagnosis	Ability to extract weak signals and early fault detection of rotating machinery
[61]	2013	MCSA	Stationary WPD	Multiclass support vector machines	BRB feature extraction by SWPT under lower-sampling rate	Lower computation and cost without any effect on the performance of SWPT to detect BRB
[62]	2013	Vibration	WPD,FFT	Artificial neural network	To classify fault and predict remaining useful life	To deal with complex problems and non-linear

Ref	Year	Diagnostic Monitoring Techniques (MTs)	Signal Processing	Classifier and Decision-making Tool	Purpose	Achievement and Limitation
						systems and predict remaining useful life
[63]	2014	Vibration	WPD	-	To improve the accuracy and rectify the distortion of WPT coefficients	Magnifying the amplitude of the fault characteristic frequency
[34]	2014	MCSA	DWT	-	To investigate the ability of different types of wavelet functions for early BRB detection	The reliability of the fault detection depends on the type of wavelet function applied for decomposition of the signal
[64]	2014	Apparent power	DWT	-	To develop air-gap eccentricity fault detection methods based on apparent power	The energy evaluation of a known bandwidth permits to define a fault severity factor (FSF)
[65]	2014	MCSA	DWT	Fuzzy support vector machine, principal component analysis, kernel neural network	To develop eccentricity fault detection methods and degree precisely based on MCSA in PMSM	The novel index for eccentricity fault diagnosis is introduced based on energy, peak, head angle of the peak, the area below the peak, the gradient of the peak and coefficients of the autoregressive (AR) model

Table 1. Summary of published paper with the aim of using wavelet transform for broken rotor bar and eccentricity fault detection

5. Case study 1

The detection of static eccentricity in three-phase LSPMSM using motor current signature analysis is studied. A detailed description of experimental test rig used in this study and the method used for signal measurement and analysis is provided in the following.

5.1. Experimental set-up

The experimental test rig is shown in Figure 4. The tested motor for both fault-free and faulty (with static eccentricity) cases is a three-phase LSPMSM with the specification as mentioned in Table 2. The motor is directly fed by the grid power supply, while the stator windings are

Y connected, and the current nominal value is 1.28 A. The LSPMSM is coupled to torque/speed sensor in order to measure the torque value in different operation conditions. On the other side, a mechanical load is provided by a DC-excited magnetic powder brake (MPB) coupled to torque/speed sensor. The specific load torque level could be furnished to the motor shaft by controlling the input dc voltage of MPB. This system is used to sample the stator current non-invasively when the motor is operated in the steady-state condition. Notably, only one phase-current signal is required to be recorded for the detection process in this study. The recorded signals are analysed by a computer-based signal processing program.
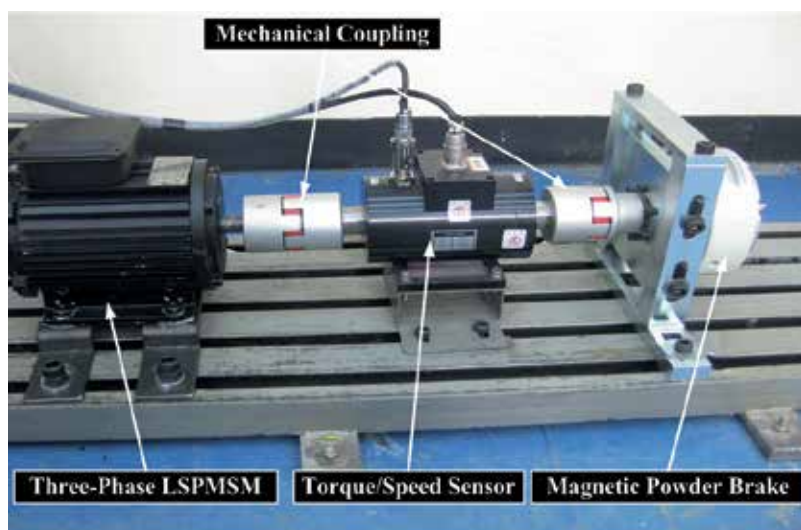
Figure 4. Experimental test rig

5.2. Method

The method proposed in this study for the creation of eccentricity fault in LSPMSM, by changing the original bearings of motor with a new set of bearing with larger inner diameter and smaller outer diameter, results in the creation of free space between the shaft and bearings and also between the bearings and the housing of end shields. Static eccentricity is created by fixing concentric inner rings between the new bearings and shaft on both ends of LSPMSM and non-concentric outer rings between the new bearings and housings of both end shields. The aforementioned strategy is used to create 33% and 50% static eccentricity in the motor discussed in the case study.

The current spectrum is stored with the sampling frequency (f_S) of 5 kHz over a total sampling period of 6.5 s, which allows the analysis of the signals with a minimum frequency of 0.15 Hz. Daubechies-24 (db24) is used as the mother wavelet in discrete wavelet transform (DWT) analyses. Since the four-pole, three-phase LSPMSM is considered, the characteristic frequency component associated with static eccentricity is located at 25 Hz, according to Eq. (3) [16].

Rated output power (HP)	1
Rated voltage (V)	415
Rated frequency (Hz)	50
Number of poles	4
Rated speed (RPM)	1500
Connection	Y
Air-gap length (mm)	0.30

Table 2. Specification of three-phase LSPMSM

The number of decomposition levels (l_d) can be determined using Eq. (16) which is $l_\mathrm{d}=7$ in this case.

$$l_\mathrm{d} = \frac{\log\left(f_\mathrm{S}\,/\,f_\mathrm{static}\right)}{\log\left(2\right)} \tag{16}$$

The frequency bands of wavelet signals are summarized in Table 3. Energies of the detail coefficient $E\left(D_j\right)$ are calculated using the following formulas [45]:

$$E\left(D_j\right) = \sqrt{\frac{1}{N_1}\sum_{i=1}^{N_1}\left(D_j\right)^2\left[i\right]} \tag{17}$$

where $j=1,\ 2,\ ...,\ l_\mathrm{d}$ and N_1 is the data length of the decomposition level.

Signal	Frequency band (Hz)
A_7	0–19.53
D_7	19.53–39.06
D_6	39.06–78.13
D_5	78.13–156.25

Table 3. The frequency bands of wavelet signals

5.3. Results and discussion

Figure 5 shows the stator current signal (original signal) and D_5, D_6, and D_7 are the detail signals obtained by db24 at level 7 for fault-free LSPMSM. The fault-related components (f_static) are visible at 25 Hz, which confirm the productivity of D_7 signal for the detection of static eccen-

tricity. The original and detail signals of LSPMSM with 33% and 50% static eccentricity are indicated in Figures 6 and 7, respectively.
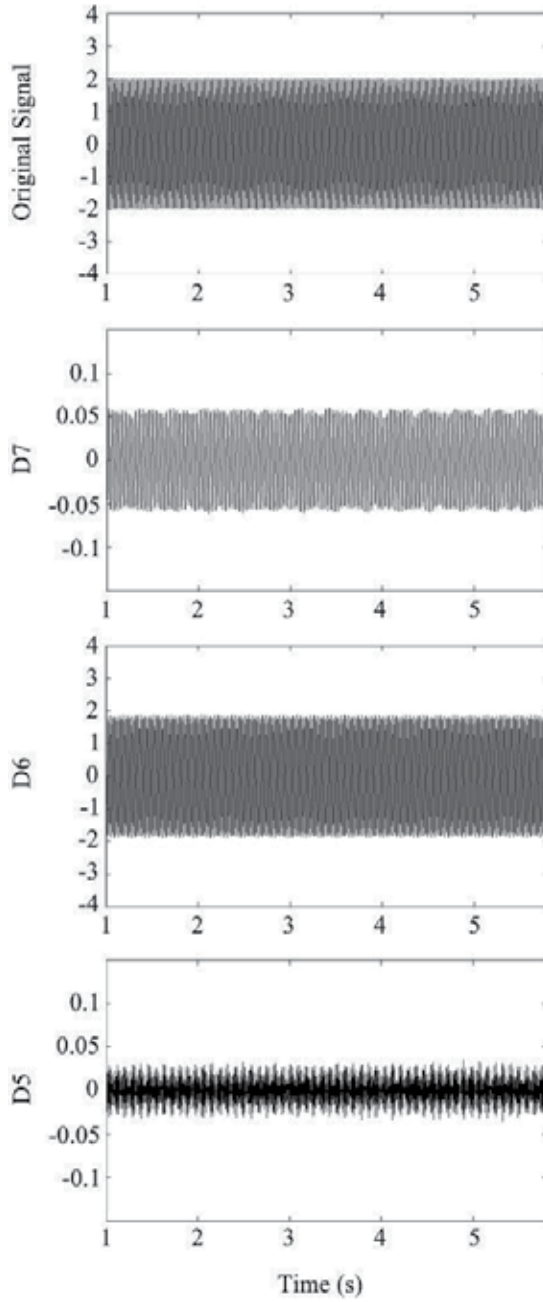
Figure 5. DWT analysis of current signal of fault-free LSPMSM

A comparison between Figures 5, 6, and 7 shows that the signals of D_7 are clear from any distortion in a fault-free motor while the high distortions are manifested in D_7 in the presence of static eccentricity that demonstrates the faulty condition of LSPMSM. The source of these distortions is due to the increase in the amplitudes of fault-related frequency components based on Eq. (3).
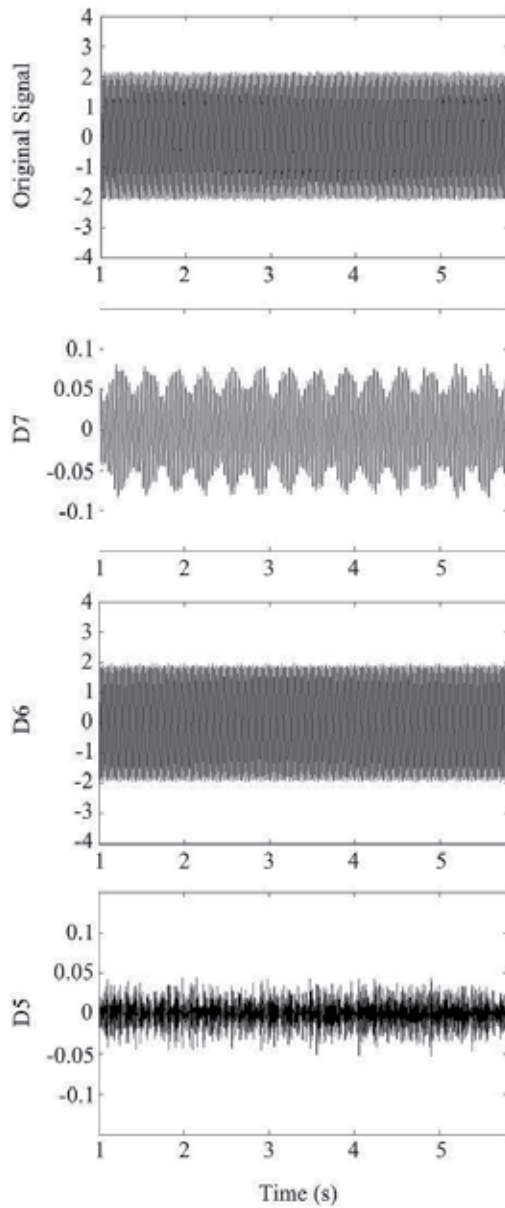
Figure 6. DWT analysis of current signal of LSPMSM under 33% static eccentricity
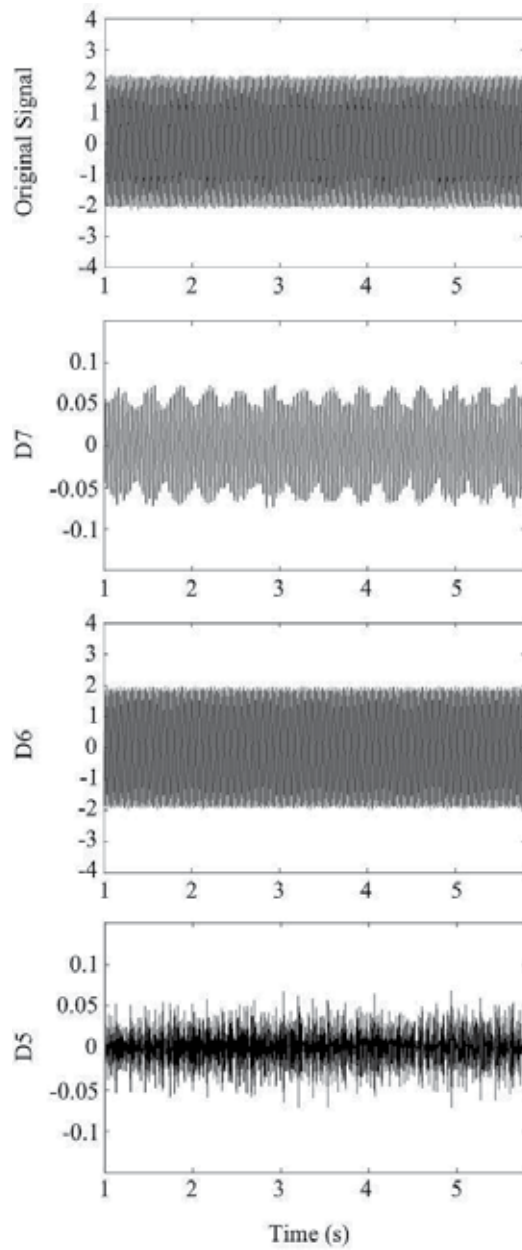
Figure 7. DWT analysis of current signal of LSPMSM under 50% static eccentricity

An effective static eccentricity detection index is introduced for three-phase LSPMSM based on the energy of D_7 for the stator current signal. The proposed index is examined for fault-free and eccentric LSPMSM with 33% and 50% static eccentricity as shown in Figure 8. The energy variation of D_7 (index) for stator current signal using db24 is provided in Table 4.
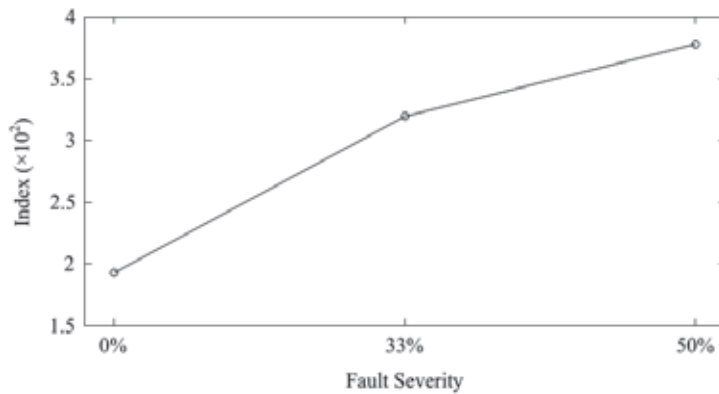
Figure 8. Static eccentricity severity versus proposed index (energy of D_7)

Index	Static eccentricity degree (%)		
	0	33	50
Energy of D_7	193	320	378

Table 4. Evaluation of proposed index due to fault degree

5.4. Conclusion

Discrete wavelet transform is employed to analyse the stator current signal of three-phase LSPMSM in order to propose an effective index for static eccentricity fault detection. The energy of detail signal (D_7) is introduced as eccentricity index. The achieved results confirm the productivity of the proposed method for the motor discussed in the case study.

6. Case study 2

The detection of broken rotor bar in three-phase squirrel cage induction motor using motor current signature analysis is studied. A detailed description of experimental test rig used in this study and the method used for signal measurement and analysis is explained in the following.

6.1. Experimental set-up

Figure 9 illustrates the experimental test rig used in this study. Table 5 presents the parameters of the three-phase squirrel cage induction motor used for both fault-free and faulty motors. The faulty motor is with three broken rotor bars. The motor is directly fed by the grid power supply, while the stator windings are Y connected and the current nominal value is 2.2 A. In order to measure the torque and speed value of the squirrel cage induction motor in different

operation conditions, a torque/speed sensor is coupled to it. A generator is used as a load and the specific load torque level can be furnished to the motor shaft by controlling the resistor connected to the generator. Recall that only one phase current signal is required to be recorded for the detection process in this study. The recorded signals are then analysed by a computer-based signal processing program.
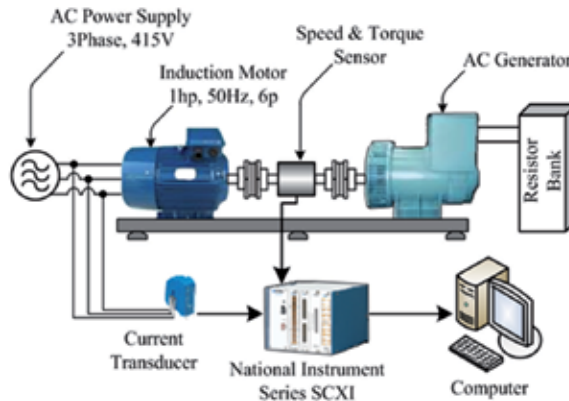
Figure 9. Experimental set-up

Rated output power (HP)	1
Rated voltage (V)	415
Rated frequency (Hz)	50
Number of poles	6
Rated speed (RPM)	1000
Connection	Y
Number of rotor bars	28

Table 5. Specification of a three-phase squirrel cage induction motor

6.2. Method

The architecture of the proposed system for broken rotor bar detection is shown in Figure 10, and the procedure used in this study is as follows: First, to force a real bar breakage in the rotor, a hole is drilled artificially in it. The original stator current was recorded from a three-phase induction motor. The stator current is sampled at 20 kHz lasting four seconds for both fault-free and faulty motors (three-rotor bar breakage) at 80% full load. The measured current signals are then decomposed using wavelet packet transform with two different purposes: One as a pre-processing of signal for FFT analysis and the frequency of $((1-2s)f_s)$ obtained is used as a fault feature for broken rotor bar detection. The other purpose of using WPT is for feature

extraction, where some statistical features determined by wavelet packet coefficients are used for broken rotor bar detection. For both purposes, Daubechies-44 (db44) is applied as a mother wavelet in 12 levels of decomposition. To extract the fault-related feature, those nodes are taken that involve fault frequency (f_{BRB}). Figure 11 shows the process explained above, called the wavelet packet tree. In this work, the signal energy, root mean square (RMS), and kurtosis are obtained as selected features for the diagnosis of the broken rotor bar.
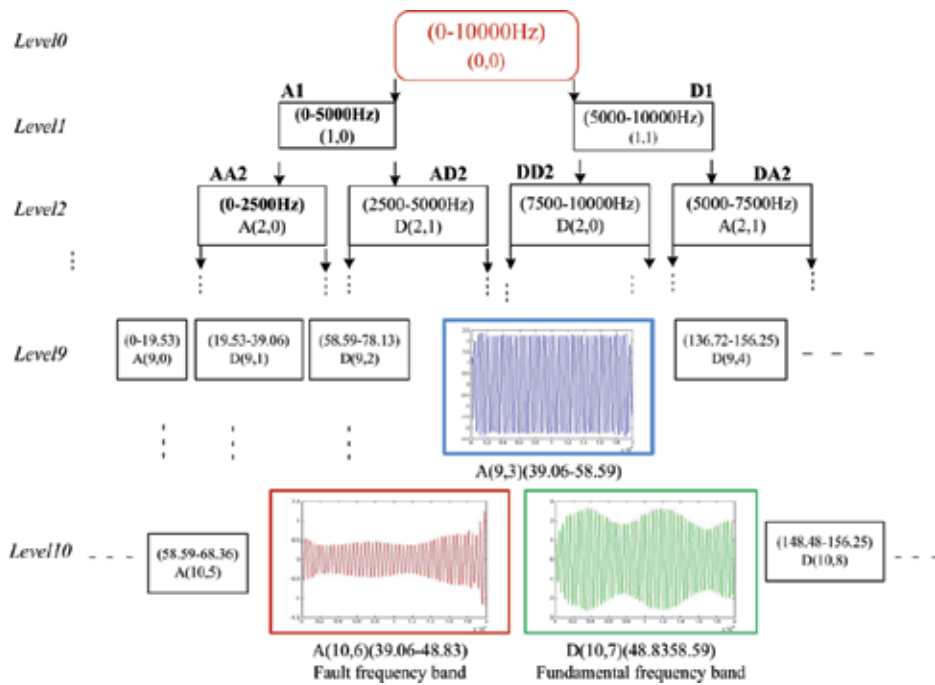
Figure 10. The architecture of the proposed system for broken rotor bar detection
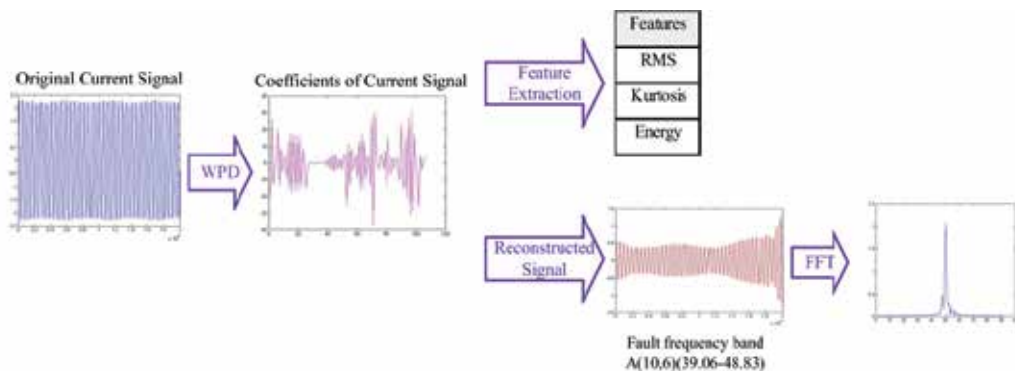
Figure 11. Approximations and details in wavelet packet decomposition

6.3. Results and discussion

In order to obtain the differences between fault-free and faulty conditions under 80% full-load conditions, WPD was used for the feature extraction. The WPD gives distinguishable signatures from stator current signal in a specific frequency band. After WPD of the current signal, two procedures for failure feature extraction using WPD are used (Figure 10). One procedure includes using FFT for the determination of amplitude of fault frequency and the other includes the statistical analysis of coefficients extracted by WPD.

The amplitude of fault frequency in the current spectrum for fault-free motors and for motors with three broken bars achieved in the first procedure is presented in Table 6. The results indicate that the amplitude of harmonic components $((1-2s)f_S)$ in both nodes, presented in Table 6, increase the faulty condition. However, the degree of increase is not significant, and it cannot be used to differentiate the conditions.

Node	Frequency Band	Amplitude (1-2s)f_s	
		Fault-free	Faulty
[10, 6]	(39.06–48.83)	0.43	0.43
[11, 13]	(46.39–48.83)	0.42	0.42
$f_{BRB} = (1-2s)f_S = 47.604$ Hz			

Table 6. Amplitudes of harmonic components for fault-free and faulty motors

In the second procedure, three statistical parameters including RMS, kurtosis and energy are calculated using the statistical analysis of coefficients determined by WPD of current signal. Table 7 presents these statistical parameters in three different nodes [10, 6], [11, 13] and [12, 26]. These parameters are compared to define the most appropriate frequency band that represents the frequency components from the broken rotor bar. According to Table 7, the nodes [11, 3] (46.39–48.83 Hz) in wavelet packet tree are the most dominant bands that can differentiate between fault-free and faulty motors under full load.

Feature	Condition	[10, 6]	[11, 13]	[12, 26]
RMS	Fault-free	11.82	15.93	40.36
	Faulty	12.96	17.78	22.06
Kurtosis	Fault-free	2.94	2.97	2.16
	Faulty	3.3	3.61	3.09
Energy	Fault-free	14,816	24,375	172,684
	Faulty	17,814	30,343	44,277

Table 7. Statistical features for fault-free and faulty motors

6.4. Conclusions

This case study proposes a feature extraction system for broken rotor bar detection using wavelet packet coefficients of the stator current. It is shown that in a faulty case, the amplitude in specific side bands increases and dominant features of signals can be extracted for fault diagnostics. The results of this study indicate that the energy, kurtosis and RMS value of WPD coefficients are the appropriate features for detecting broken rotor bar in particular bands.

Acknowledgements

Author details

Mohammad Rezazadeh Mehrjou[1,2], Norman Mariun[1,2], Mahdi Karami[1,2],
Samsul Bahari Mohd. Noor[2], Sahar Zolfaghari[2], Norhisam Misron[2],
Mohd Zainal Abidin Ab. Kadir[2], Mohd. Amran Mohd. Radzi[1,2] and
Mohammad Hamiruce Marhaban[2]

*Address all correspondence to: Mehrjou.mo@gmail.com

1 Centre for Advanced Power and Energy Research (CAPER), Faculty of Engineering, Universiti Putra Malaysia, Serdang, Malaysia

2 Department of Electrical and Electronic Engineering, Faculty of Engineering, Universiti Putra Malaysia, Serdang, Malaysia

References

[1] Didier G, Ternisien E, Caspary O, Razik H. A new approach to detect broken rotor bars in induction machines by current spectrum analysis. Mechanical Systems and Signal Processing. 2007; 21: 1127–1142.

[2] Andrew JK, Lin D, Dragan B. A review on machinery diagnostics and prognostics implementing condition-based maintenance. Mechanical Systems and Signal Processing. 2006; 20: 1483–1510.

[3] Chow MY. Guest editorial special section on motor fault detection and diagnosis. IEEE Transactions on Industrial Electronics. 2000; 47.5: 982–983.

[4]   Bin GF, Gao JJ, Li XJ, Dhillon BS. Early fault diagnosis of rotating machinery based on wavelet packets – Empirical mode decomposition feature extraction and neural network. Mechanical Systems and Signal Processing. 2012; 27: 696–711.

[5]   Burnett R, Watson J, Elder S. The application of modern signal processing techniques to rotor fault detection and location within three phase induction motors. Signal processing. 1996; 49.1: 57–70.

[6]   Bonnett AH, Yung C. Increased efficiency versus increased reliability. IEEE Industry Applications Magazine. 2008; 14.1: 29–36.

[7]   Bonnett AH, Soukup GC. Cause and analysis of stator and rotor failures in three-phase squirrel-cage induction motors. IEEE Transactions on Industry Applications. 1992; 28.4: 921–937.

[8]   Mehrjou MR, Mariun N, Hamiruce Marhaban M, Misron N. Rotor fault condition monitoring techniques for squirrel-cage induction machine – a review. Mechanical Systems and Signal Processing. 2011; 25.8: 2827–2848.

[9]   Ebrahimi BM, Faiz J, Lotfi-fard S, Pillay P. Novel indices for broken rotor bars fault diagnosis in induction motors using wavelet transform. Mechanical Systems and Signal Processing. 2012; 131–145.

[10] Thomson WT, Fenger M. Current signature analysis to detect induction motor faults. IEEE Industry Applications Magazine. 2001; 7.4: 26–34.

[11] Bellini A, Filippetti F, Tassoni C, Capolino GA. Advances in diagnostic techniques for induction machines. IEEE Transactions on Industrial Electronics. 2008; 55.12: 4109–4126.

[12] Cameron JR, Thomson WT, Dow AB. Vibration and current monitoring for detecting airgap eccentricity in large induction motors. In: Proceedings of IEE Electric Power Applications; 1986. pp. 155–163.

[13] Nandi S, Toliyat HA, Li X. Condition monitoring and fault diagnosis of electrical motors – a review. IEEE Transactions on Energy Conversion. 2005; 20.4: 719–729.

[14] Faiz J, Ojaghi M. Different indexes for eccentricity faults diagnosis in three-phase squirrel-cage induction motors: a review. Mechatronics. 2009; b19: 2–13.

[15] Thomson WT, Gilmore RJ. Motor current signature analysis to detect faults in induction motor drives–fundamentals, data interpretation and industrial case histories. In: Proceedings of the 32nd Turbomachinery Symposium, Houston, TX, USA; 2003. pp. 145–156.

[16] Karami M, Mariun N, Mehrjou MR, Ab Kadir MZA, Misron N, Mohd Radzi MA. Static eccentricity fault recognition in three-phase line start permanent magnet synchronous motor using finite element method. Mathematical Problems in Engineering. 2014; 1–12.

[17] Torkaman H, Afjei E. Sensorless method for eccentricity fault monitoring and diagnosis in switched reluctance machines based on stator voltage signature. IEEE Transactions on Magnetics. 2013; 49.2: 912–920

[18] Hong J, Park S, Hyun D, Kang T, Lee SB, Kral C, Haumer A. Detection and classification of rotor demagnetization and eccentricity faults for PM synchronous motors. IEEE Transactions on Industry Applications. 2012; 48.3: 923–932.

[19] Wiedenbrug EJ, Teska M, Nandi S, Chelvan IT. Automated monitoring of airgap eccentricity for inverter-fed induction motors under standstill conditions. IEEE Transactions on Industry Applications. 2011; 47.3: 1257–1266.

[20] Dorrell DG, Cossar C. A vibration-based condition monitoring system for switched reluctance machine rotor eccentricity detection. IEEE Transactions on Magnetics. 2008; 44.9: 2204–2214.

[21] Nandi S, Bharadwaj R, Toliyat HA, Parlos AG. Study of three phase induction motors with incipient rotor cage faults under different supply conditions. In: Proceedings of IEEE Industry Applications Conference, 34th IAS Annual Meeting; 1999. pp. 1922–1928.

[22] Sasi AB, Gu F, Li Y, Ball AD. A validated model for the prediction of rotor bar failure in squirrel-cage motors using instantaneous angular speed. Mechanical Systems and Signal Processing. 2006; 20.7: 1572–1589.

[23] Ilonen J, Kamarainen JK, Lindh T, Ahola J, Kälviäinen H, Partanen J. Diagnosis tool for motor condition monitoring. IEEE Transactions on Industry Applications. 2005; 41.4: 963–971.

[24] Pennacchi P, Bachschmid N, Vania A, Zanetta GA, Gregori L. Use of modal representation for the supporting structure in model-based fault identification of large rotating machinery : Part 1- theoretical remarks. Mechanical Systems and Signal Processing. 2006; 20.3: 662–681.

[25] Bachschmid N, Pennacchi P, Tanzi E. Cracked rotors: a survey on static and dynamic behaviour including modelling and diagnosis. Springer Science & Business Media, 2010. ISBN 978-3-642-01484-0.

[26] Siddique A, Yadava GS, Singh B. A review of stator fault monitoring techniques of induction motors. IEEE Transactions on energy conversion. 2005; 20.1: 106–114.

[27] Thorsen OV, Dalva M. A survey of faults on induction motors in offshore oil industry, petrochemical industry, gas terminals, and oil refineries. IEEE Transactions on Industry Applications. 1995; 31.5: 1186–1196.

[28] Acosta GG, Verucchi CJ, Gelso ER. A current monitoring system for diagnosing electrical failures in induction motors. Mechanical Systems and Signal Processing. 2006; 20: 953–965.

[29] Kliman GB, Koegl RA, Stein J, Endicott RD, Madden MW. Noninvasive detection of broken rotor bars in operating induction motors. IEEE Transactions Energy Conversion 1988; 3.4: 873–879, 1988

[30] Daubechies I. The wavelet transform, time-frequency localization and signal analysis. IEEE transactions on information theory. 1990; 36.5: 961–1005.

[31] Peng ZK, Chu FL. Application of the wavelet transform in machine condition monitoring and fault diagnostics: a review with bibliography. Mechanical Systems and Signal Processing. 2004; 18.2: 199–221.

[32] Mallat SG. A theory for multiresolution signal decomposition: the wavelet representation. IEEE Transactions on Pattern Analysis and Machine Intelligence. 1989; 11.7: 674–693.

[33] Polikar R, Udpa L, Udpa SS, Taylor T. Frequency invariant classification of weld inspection signals. IEEE Ultrasonics Ferroelectrics and Frequency Control. 1998; 45.3: 614–625.

[34] Mehrjou M R, Mariun N, Karami M, Misron N, Toosi S, Zare MR. Evaluation of wavelet-functions for broken rotor bar detection of induction machine using coefficient-related features. International Journal of Applied Electronics in Physics & Robotics. 2013; 1.1: 18–23.

[35] Ekici S, Yildirim S, Poyraz M. Energy and entropy-based feature extraction for locating fault on transmission lines by using neural network and wavelet packet decomposition. Expert System Application. 2008; 34.4: 2937–2944.

[36] Abbaszadeh K, Milimonfared J, Haji M, Toliyat HA. Broken bar detection in induction motor via wavelet transformation. In: Proceedings of the 27th Annual Conference of the IEEE in Industrial Electronics Society; 2001. pp. 95–99.

[37] Combastel C, Lesecq S, Petropol S, Gentil S. Model-based and wavelet approaches to induction motor on-line fault detection. Control Engineering Practice. 2002; 10.5: 493–509.

[38] Kim K, Parlos AG. Induction motor fault diagnosis based on neuropredictors and wavelet signal processing. IEEE/ASME Transactions Mechatronics. 2002; 7.2: 201–219.

[39] Ye Z, Wu B, Sadeghian A. Current signature analysis of induction motor mechanical faults by wavelet packet decomposition. IEEE Transactions on Industry Electronics. 2003; 50.6: 1217–1228.

[40] Douglas H, Pillay P, Ziarani A. A new algorithm for transient motor current signature analysis using wavelets. IEEE Transactions on Industry Applications. 2004; 40.5: 1361–1368.

[41] Bae H, Kim S, Kim YT, Lee SH. Application of time-series data mining for fault diagnosis of induction motors. Lecture Notes in Computer Science Computational Science and Its Applications. 2005; 1085–1094.

[42] Douglas H, Pillay P, Ziarani A. Broken rotor bar detection in induction machines with transient operating speeds. IEEE Transactions Energy Conversion. 2005; 20.1: 135–141.

[43] Supangat R, Ertugrul N, Soong L, Gray D, Hansen C, Grieger J. Broken rotor bar fault detection in induction motors using starting current analysis, In: Proceedings of European Conference on Power Electronics and Application, Dresden, Germany, 2005.

[44] Ye Z, Sadeghian A, Wu B. Mechanical fault diagnostics for induction motor with variable speed drives using adaptive neuro-fuzzy inference system. Electric Power Systems Research. 2006; 9, 10: 742–752.

[45] Kia SH, Mabwe AM, Henao H, Capolino GA. Wavelet based instantaneous power analysis for induction machine fault diagnosis. In: Proceedings 32nd Annual Conference on IEEE Industrial Electronics, IECON; 2006. pp. 1229–1234.

[46] Lee SH, Cheon SP, Kim Y, Kim S. Fourier and wavelet transformations for the fault detection of induction motor with stator current. Lecture Notes in Computer Science. Springer. 2006; 4114: 557–569.

[47] Antonino-Daviu J, Riera-Guasp M, Roger-Folch J, Palomares M. Validation of a new method for the diagnosis of rotor bar failures via wavelet transform in industrial induction machines. IEEE Transactions on Industry Applications. 2006; 42.4: 990–996.

[48] Supangat R, Grieger J, Ertugrul N, Soong WL, Gray DA, Hansen C. Detection of broken rotor bar faults and effects of loading in induction motors during rundown. In: Proceedings of IEEE International Electric Machines and Drives Conference; 2007. pp. 196–201.

[49] Zarei J, Poshtan J. Bearing fault detection using wavelet packet transform of induction motor stator current. Tribology International. 2007; 40: 763–769.

[50] Khan MASK, Member S, Radwan TS, Member S, Rahman MA. Real-time implementation of wavelet packet transform-based diagnosis and protection of three-phase induction motors. IEEE Transactions on Energy Conversion. 2007; 22.3: 647–655.

[51] Cusido J, Romeral L, Ortega JA, Rosero JA, Espinosa AG. Fault detection in induction machines using power spectral density in wavelet decomposition. IEEE Transactions on Industrial Electronics. 2008; 55.2: 633–643.

[52] Widodo A, Yang BS. Wavelet support vector machine for induction machine fault diagnosis based on transient current signal. Expert Systems with Applications. 2008; 35.1–2: 307–316.

[53] Sadeghian A, Ye Z, Wu B. Online detection of broken rotor bars in induction motors by wavelet packet decomposition and artificial neural networks. IEEE Transactions on Instrumentation and Measurement. 2009; 58.7: 2253–2263.

[54] Antonino-Daviu J, Rodriguez PJ, Riera-Guasp M, Pineda-Sanchez M, Arkkio A. Detection of combined faults in induction machines with stator parallel branches through the DWT of the startup current. Mechanical Systems and Signal Processing. 2009; 23.7: 2336–2351.

[55] Hedayati Kia S, Henao H, Capolino GA. Diagnosis of broken-bar fault in induction machines using discrete wavelet transform without slip estimation. IEEE Transactions on Industry Applications. 2009; 45.4: 1395–1404.

[56] Rafiee J, Tse PW, Harfi A, Sadeghi MH. A novel technique for selecting mother wavelet function using an intelligent fault diagnosis system. Expert Systems with Applications. 2009; 36: 4862–4875.

[57] Xian GM, Zeng BQ. An intelligent fault diagnosis method based on wavelet packet analysis and hybrid support vector machines. Expert Systems Applications. 2009; 36: 12131–12136.

[58] Mehrjou MR, Mariun N, Hamiruce Marhaban M, Misron N. Evaluation of Fourier and wavelet analysis for efficient recognition of broken rotor bar in squirrel-cage induction machine. In: Proceedings of IEEE International Conference on Power and Energy, Kuala Lumpur, Malaysia, 2010.

[59] Cusido J, Romeral L, Ortega JA, Garcia A, Riba JR. Wavelet and PDD as fault detection techniques. Electric Power Systems Research. 2010; 80.8: N915–N924.

[60] García-Escudero LA, Duque-Perez O, Morinigo-Sotelo D, Perez-Alonso M. Robust condition monitoring for early detection of broken rotor bars in induction motors. Expert Systems with Applications. 2011; 38.3: 2653–2660.

[61] Keskes H, Braham A, Lachiri Z. Broken rotor bar diagnosis in induction machines through stationary wavelet packet transform and multiclass wavelet SVM. Electric Power Systems Research. 2013; 97: 151–157.

[62] Zhang Z, Wang Y, Wang K. Fault diagnosis and prognosis using wavelet packet decomposition, Fourier transform and artificial neural network. Journal of Intelligent Manufacturing.2013; 24:1213-1227.

[63] Jiao X, Ding K, He G. An algorithm for improving the coefficient accuracy of wavelet packet analysis. Measurement. 2014; 47: 207–220.

[64] Yahia K, Cardoso AJM, Ghoggal A, Zouzou SE. Induction motors airgap-eccentricity detection through the discrete wavelet transform of the apparent power signal under non-stationary operating conditions. ISA Transactions. 2014; 53: 603–611.

[65] Ebrahimi BM, Roshtkhari MJ, Faiz J, Khatami SV. Advanced eccentricity fault recognition in permanent magnet synchronous motors using stator current signature analysis. IEEE Transactions on Industrial Electronics.2014; 61.4: 2041–2051.

Empirical Wavelet Transform-based Detection of Anomalies in ULF Geomagnetic Signals Associated to Seismic Events with a Fuzzy Logic-based System for Automatic Diagnosis

Omar Chavez Alegria, Martin Valtierra-Rodriguez,
Juan P. Amezquita-Sanchez, Jesus Roberto Millan-Almaraz,
Luis Mario Rodriguez, Alejandro Mungaray Moctezuma,
Aurelio Dominguez-Gonzalez and Jose Antonio Cruz-Abeyro

Additional information is available at the end of the chapter

Abstract

Owing to the relevance and severity of damages caused by earthquakes (EQs), the development and application of new methods for seismic activity detection that offer an efficient and reliable diagnosis in terms of processing and performance are still demanding tasks. In this work, the application of the Empirical Wavelet Transform (EWT) for seismic detection in ultra-low-frequency (ULF) geomagnetic signals is presented. For this, several ULF signals associated to seismic activities and random calm periods are analysed. These signals have been obtained through a tri-axial fluxgate magnetometer at the Juriquilla station localized in Queretaro, Mexico, longitude -100.45° N and latitude 20.70°E. In order to show the advantages of the proposal, a comparison with the discrete wavelet transform (DWT) is presented. The results shown a better detection capability of seismic signals before, during, and after the main shock than the ones obtained by the DWT, which makes the proposal a more suitable and reliable tool for this task. Finally, a fuzzy logic (FL)-based system for automatic diagnosis using the variance of the EWT outputs for the tri-axial fluxgate magnetometer signals is also proposed.

Keywords: Empirical Wavelet Transform, Time-Frequency Analysis, Earthquake interaction, forecasting, prediction

1. Introduction

Among the natural disasters, the EQs have attracted the interest of many researchers around the world due to the huge amount of human, material, and economic losses [1]. They have been focused on finding pre-seismic precursors for prediction and forecasting tasks [2-6]. In this regard, different electromagnetic phenomena (EP) encompassing a large frequency range, being the ultra-low-frequency (ULF) range one of the most promising, have been associated with EQs because they typically occur during, but sometimes prior to seismic activity [7-14] Although many detection methods have been proposed, the relevance and severity of EQs damages demand still more efficient and reliable diagnosis methods.

Techniques and methods such as polarization or spectral density ratio analysis [15-16], transfer function analysis [17], fractal analysis [18-22], singular value decomposition [23], principal component analysis [16, 21], and the discrete wavelet transform (DWT) [2, 24], among others have been proposed to analyse the ULF geomagnetic signals associated to EQs. Yet, despite showing promising results, the inherent characteristics of the ULF geomagnetic signals such as high noise levels, weak amplitude, and interferences from other sources due to the distance between the epicenter and sensor, among others may compromise the performance and reliability of the analysis. From this point of view, the development and application of new detection methods to make a more efficient and reliable diagnosis in terms of processing and performance are still interesting research fields.

In this chapter, the application of the empirical wavelet transform (EWT) to ULF signals for detecting seismic precursor anomalies is presented. Besides, a comparison with the DWT is carried out in order to show the EWT advantages. Moreover, a fuzzy logic (FL) system for automatic diagnosis using the variance of the EWT results is proposed. For this, three ULF signals associated to seismic activities and random calm periods are analysed. The obtained results show the usefulness and effectiveness of the proposed methodology, making it a suitable and reliable tool to detect ULF anomalies.

2. ULF geomagnetic data

In order to investigate the relationships between ULF geomagnetic signals and pre-seismic anomalies, ULF geomagnetic data from Juriquilla seismic station, located in Queretaro, Mexico, with geographic coordinates: longitude -100.45° N and latitude 20.70° E, are used. The ULF geomagnetic signals are monitored by means of a fluxgate magnetometer. It allows monitoring three mutually orthogonal components of the magnetic field, two horizontal (Mx: North-South and My: East-West) components and a vertical component (Mz). The three geomagnetic components are measured using a sampling frequency of 1 Hz to obtain 65,000 samples during a time window of 18 hrs, which comprise 9 hours before the main shock and 9 hrs after it. In this research, three recent seismic events with magnitude greater than 6.0 are analysed. Further, for comparison purposes, random analyses during periods of seismic calm are used. Table 1 summarize the characteristics of the studied EQs.

To discriminate the geomagnetic activity of the magnetosphere because of the solar activity and cultural noise, the analysed EQs data are compared with the geomagnetic activity expressed by Dst index (http://wdc.kugi.kyoto-u.ac.jp/dstdir/), where those indices apparently had no correlation with EQs variation.

Event	Year	Month	Day	Hour	Min	Longitude	Latitude	Magnitude, M	Depth, km	Distance, km	ϱ, km	Distance/ϱ
1	2009	8	3	13	0	-112.24	28.48	6.9	10	1473	2292	0.64
2	2009	9	24	2	16	-107.43	17.72	6.2	21	8052	1109	0.73
3	2010	6	30	2	22	-98.03	16.22	6.0	8	563	684	0.82

Note: The Year / month / day / hour / minute are the exact time of the EQ (Local Time); Latitude and Longitude are the geographic coordinates of the epicenter, Magnitude and Depth are the EQ measures, Distance is the distance between the epicenter and Juriquilla station, and p is the radius of the EQ preparation.

Table 1. Characteristics of the Earthquakes occurred in Mexico during 2009–2010. Their magnitudes are presented in bold (Catalogue of National Seismological Service, Mexico)

3. Wavelet transform

This section presents the theoretical background of the Discrete Wavelet transform and the Empirical Wavelet Transform used for the analysis of ULF signals.

3.1. Discrete wavelet transform

Discrete Wavelet Transform (DWT) is a useful method for analysis of non-stationary, no linear and transient signals because it decomposes the time series signal into multiple time-frequency levels retaining the characteristics of the analysed signal [2]. DWT is defined by Eq. (1), where $x(n)$ and $h(n)$ denote the discrete signal and the wavelet basis function, respectively, of the total number N of samples contained in the signal $x(n)$. j and k represent the time scaling, and the shifting of the discrete wavelet function, respectively.

$$DWT_{j,k} = \sum_N x(n)\overline{h_{j,k}(n)}$$

(1)

The DWT is calculated using a set of low- and high-pass filters bank called approximations (AC_L) and details (DC_L) into desired levels L (Mallat algorithm), respectively, as shown in Figure 1. Based on the Mallat algorithm, the approximation obtained from the first level is split into a new decomposition and approximation and this process is repeated [25]. Once the discrete time signal $x(n)$ has been decomposed into the desired levels, the signal is reconstructed by applying the decomposition process in an inverse way, which is known as the inverse discrete wavelet transform (IDWT).
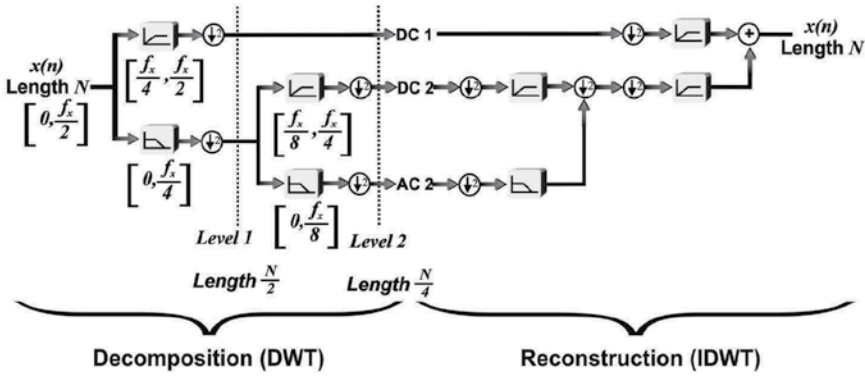
Figure 1. DWT basis construction.

According to the Mallat algorithm, the frequency band for the approximations AC_L and decompositions DC_L DC are given by Eq. (2) and Eq. (3), respectively, where F_s represents the sampling frequency of the signal.

$$AC_L \Rightarrow \left[0, \frac{F_s}{2^{L+1}} \right] \tag{2}$$

$$DC_L \Rightarrow \left[\frac{F_s}{2^{L+1}}, \frac{F_s}{2^L} \right] \tag{3}$$

Different types of wavelet mother function have been proposed to analyse ULF signals in order to find anomalies related with EQs such as Daubechies, Haar, Morlet, Symlets, Coiflets, and Meyer (Figure 2). However, it has been demonstrated that the most effective to analyse ULF signals is the Daubechies mother function [2, 24, 26]. For this reason, Daubechies as mother wavelet is used in this work.

3.2. Empirical wavelet transform

EWT is a new adaptive wavelet transform capable of decomposing a time series signal $x(t)$ into adaptive time-frequency sub-bands according to its contained frequency information [27]. This advantage allows generating narrow time-frequency sub-bands, unlike the DWT where the calculated time-frequency sub-bands depend on sampling frequency of the time signal. To provide an adaptive wavelet with respect to the analysed signal, the segmentation of the signal is an important step in the EWT. It can be performed either manually or by means of the Fourier spectrum. If the signal is segmented manually, the boundaries of the wavelet filters can be user selected as contiguous segments. On the other hand, using the Fourier spectrum, first, the local maxima of the Fourier spectrum $x(\omega)$ x are calculated. Next, the boundaries ω_i ω of each segment are defined as the center between two consecutive maxima. Thus, the Fourier support $[0, \pi]$ is segmented N into contiguous sets or frequency bands. In both segmentations, each frequency band is indicated by $\Lambda_n = [\omega_{n-1}, \omega_n]$ $\Lambda n = [\omega$ and satisfy, as shown in Figure. 3. A
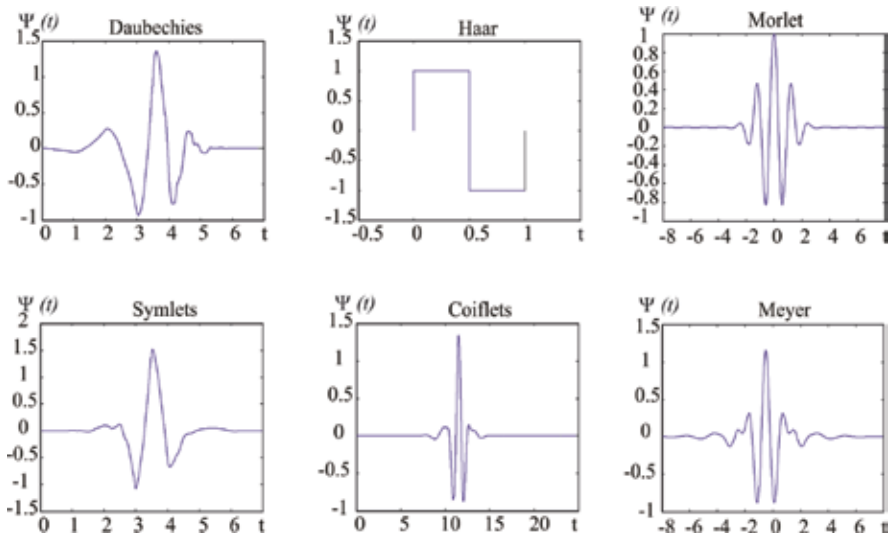
Figure 2. Wavelets used in ULF signals.

transition phase of width $2\tau_n$ 2τ is defined to obtain a tight frame around each ω_n ω. A more detailed selection of τ_n τ is presented in [27]. Observing Figure. 3, the empirical wavelets are defined by one low-pass represented by LPF $\phi_n(\omega)$ and $N-1$ N band-pass $\psi_n(\omega)$ filters represented by BPF corresponding to the approximation and details components, respectively, on each Λ_n Λn.
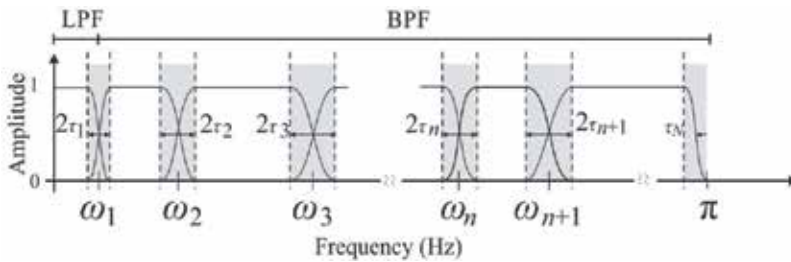
Figure 3. EWT basis construction.

Following the idea used in deriving the Meyer's wavelet, [27] defines the empirical scaling function to estimate the low-pass wavelet filter coefficients according to following Equation:

$$\phi_n(\omega) = \begin{cases} 1 & if \: |\omega| \leq \omega_n - \tau_n \\ cos\left[\dfrac{\pi}{2}\beta\left(\dfrac{1}{2\tau_n}\left(|\omega| - \omega_n + \tau_n\right)\right)\right] & if \: \omega_n - \tau_n \leq |\omega| \leq \omega_n + \tau_n \\ 0 & otherwise \end{cases} \tag{4}$$

And an empirical wavelet function to build the N-1 band-pass filters as:

$$\psi_n(\omega) = \begin{cases} 1 & if\ \omega_n + \tau_n \le |\omega| \le \omega_{n+1} - \tau_{n+1} \\ \cos\left[\frac{\pi}{2}\beta\left(\frac{1}{2\tau_{n+1}}\left(|\omega| - \omega_{n+1} + \tau_{n+1}\right)\right)\right] & if\ \omega_{n+1} - \tau_{n+1} \le |\omega| \le \omega_{n+1} + \tau_{n+1} \\ \sin\left[\frac{\pi}{2}\beta\left(\frac{1}{2\tau_n}\left(|\omega| - \omega_n + \tau_n\right)\right)\right] & if\ \omega_n + \tau_n \le |\omega| \le \omega_n + \tau_n \\ 0 & otherwise \end{cases} \tag{5}$$

where $\beta(x)$ is a polynomial function taken as $\beta(x) = x^4(35 - 85x + 70x^2 - 20x^3)$

After having built the wavelet filters, the signal $x(t)$ is decomposed into different frequency bands through empirical wavelet transform defined by

$$W_f^\epsilon(n, t) = F^{-1}\left(x(\omega)\psi_n(\omega)\right) \tag{6}$$

$$W_f^\epsilon(0, t) = F^{-1}\left(x(\omega)\phi_n(\omega)\right) \tag{7}$$

where the details $W_f(n, t)$ and approximation $W_f(0, t)$ coefficients are obtained by the inner products of the signal with the empirical wavelets low-pass and band-pass filters, respectively, and F^{-1} is the inverse Fourier transform.

4. EWT and fuzzy logic system

This section presents the proposed methodology. It consists of the ULF geomagnetic signals analysis through the EWT, then a statistical parameter based on the variance is applied and, finally, an automatic diagnosis by means of a FL system is computed as shown in Figure. 4.

Figure 4. Proposed methodology.

4.1. EWT analysis

Generally, the pre-seismic anomalies are too much weak to be detected by the Fourier transform (Chavez et al., 2010); hence, the frequency bands are selected manually using the EWT. Several experimental using both algorithms are carried out to estimate the best frequency band of the ULF geomagnetic signal to detect anomalies associated to the EQs. After the experimental runs, it is found that for the EWT algorithm the frequency band from 0.0470 to 0.0781 Hz and for the DWT algorithm the frequency band or third decomposition from 0.0625 to 0.125 Hz with a Daubechies wavelet of order 5 generate the best results, enhancing correlation with associated seismic anomalies events. Figure. 5 presents the obtained results for the EWT and the DWT, where both the seismic calm signal (left-side plots) and the seismic activity signal (right-side plots), which corresponds to event 1 (Table 1), can be observed. Figure.5(a) shows that in both analysis, the seismic calm period do not present significant spikes over time, indicating the absence of seismic activity. On the other hand, observing the results shown in Figure. 5(b), both time-frequency analysis can detect the occurrence of peaks prior to seismic (Pre-seismic event zone) and another peaks after the main shock (Post-seismic event zone). These magnetic perturbations occur about 8hrs before the main shock and about 2 hrs after it. Open circles remark perturbations in the signal.. But, it is noticeable that, using the EWT method, it is better noticeable of the pre-seismic and post-seismic anomalies.
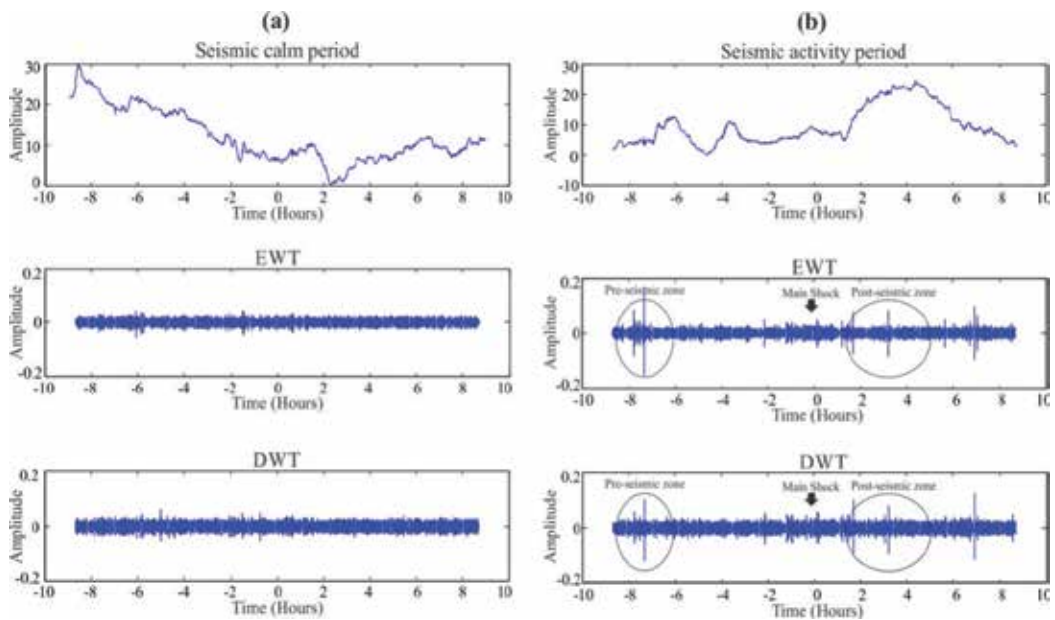
Figure 5. Comparison between the EWT time-frequency analysis and DWT time-frequency analysis; for (a) seismic calm, and (b) with seismic activity.

In order to evaluate the significance of these results, a complementary statistical analysis based on the variance of the EWT and DWT results is computed to measure the fluctuations between seismic activity and seismic calm period as follows:

$$V = \frac{1}{N} \sum_{n=1}^{N} \left[x(n) - \bar{x} \right] \tag{8}$$

where V is the variance of each data window at the frequency band, N is the total of data analysed for the region of interest, x(n) is the input sequence, and $\bar{x}$ is the mean value of x(n). Figures. 6(a) 6(b) show the variance (V) results obtained by the EWT and the DWT method, respectively, for seismic activity and seismic calm period. The results correspond to running data windows each 1000 samples. It is observed that the EWT method presents a better performance to detect seismic anomalies than DWT method. Hence, it can be established that the EWT analysis allows the observation of ULF signal perturbations with low amplitude and embedded in high level of noise.
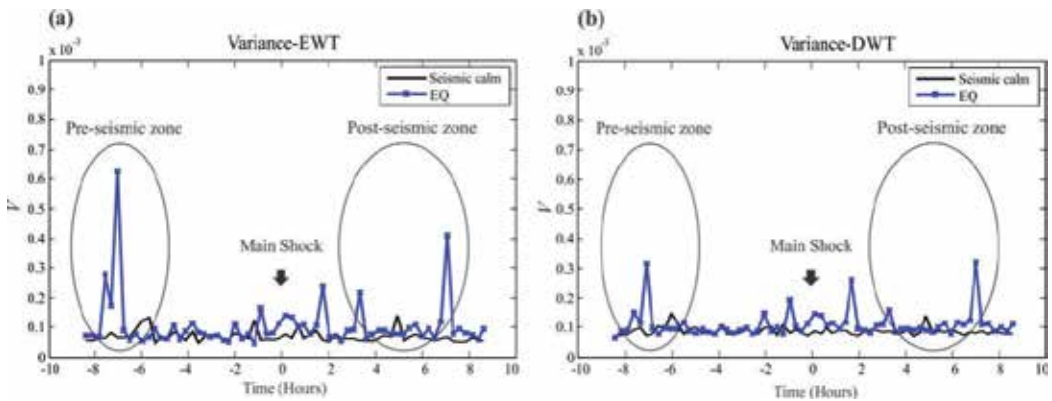
Figure 6. Variance (V) of the seismic activity and seismic calm period using: (a) EWT and (b) DWT.

4.2. Study cases

After showing in the previous section that EWT improves the correlation between the seismic event and the ULF electromagnetic signal, the proposed EWT time-frequency analysis is applied to seismic calm and three seismic events with different geographical location. Figure. 7 shows the EWT time-frequency analysis for seismic calm period and the 3 seismic events. The three components of the magnetic field, Mx, My, and Mz, are analysed as shown in Figure. 7. The main shock position is indicated by an arrow and two circles. It shows the pre-seismic and post-seismic anomalies associated with the EQs. The EWT results for seismic calm period do not present significant spikes over time, indicating the absence of seismic activity, as shown in Figure. 7(a-c); unlike the signals with seismic activity where several spikes appear before and after the main shock. All the analysed signals comprise 9 hrs before and 9 hrs after each seismic event, considering the time zero as the specific time of the occurrence of the EQ.

Similar to previous section, to evaluate the significance of the results, a complementary statistical analysis based on the variance of the EWT results is computed to measure the fluctuations between seismic activity and seismic calm period. Figure. 8 shows the variance V results obtained for three analysed seismic events as well as for their three components (Mx, My, and Mz). The results correspond to running data windows each 1000 samples. According
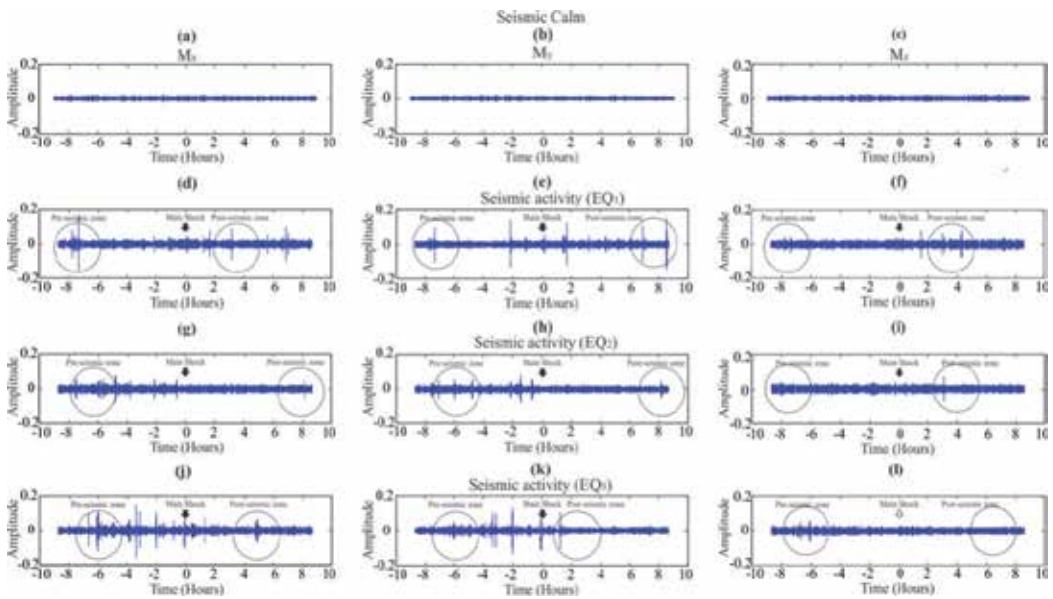
Figure 7. EWT analysis of the three geomagnetic components: Mx, My and Mz, for a seismic calm (a-c), and with seismic activity: (d) to (f) EQ1, (g) to (i) EQ2, and (j) to (l) EQ3.

to the obtained results in Figure.8(a-c), there are important variations of V for the three components that could be associated with occurrence of the EQs. As observed, V increases before, during and, after the seismic event on the three components: Mx (a), My (b), and Mz (c). Observing Figure. 8, the Mx geomagnetic component presents an important variance in three different ranges: from 8 to 5 hrs before seismic event, between 2hr before and 2hr after the main shock, and from 3 to 7 hrs after the main EQs (post-seismic zone). The My component shows variance in different ranges, from 8 to 6 hrs before seismic event, between 2 hrs before and 2 hrs after main shock, and from 3 to 8 hrs after the main EQs. Finally, the Mz geomagnetic component also presents variance in three different ranges: from 8 to 6 hrs before seismic event, 2 hrs before and 2 hrs after main shock, and from 4 to 8 hrs after seismic event. In summary, these results show that the EWT is adequate to find electro-magnetic seismic precursors related to the variance magnitude.
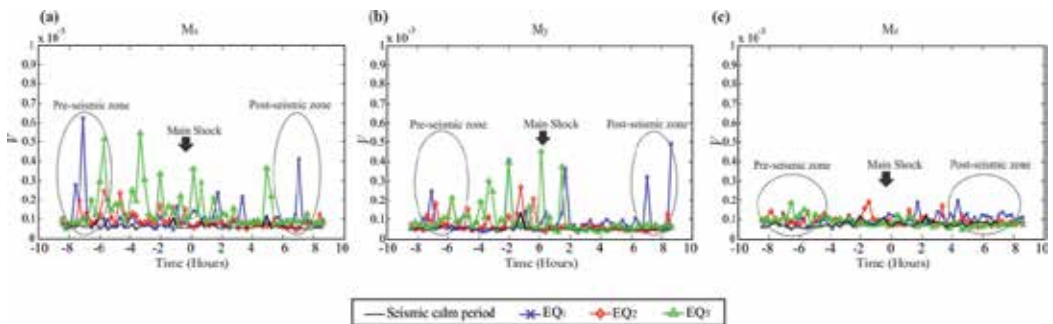
Figure 8. Variance of the EWT for the three geomagnetic components: (a) Mx, (b) My, and (c) Mz.

4.3. Fuzzy logic-based system

Once the variance of the EWT signals is computed, a FL-based system is used for automatically diagnosing the severity of the ULF geomagnetic variations associated to seismic events. A FL system represents a group of rules for reasoning under uncertainty in an imprecise or fuzzy manner. It is usually used when a mathematical model of a process does not exist or does exist but is too difficult to encode and too complex to be evaluated fast enough for real time operation. Besides, it can use several sources of information in order to take a decision according to a particular objective.

The designed and implemented FL system to perform the diagnosis process is a Mamdani-type fuzzy inference system with two inputs, one output, and 16 rules. The system uses Max–Min composition, and the centroid of area method for defuzzification. The inputs are the variance of EWT results for the signals Mx and My, the Mz signal is not considered since it presents a low difference between seismic activity and calm period. These inputs are partitioned into four trapezoidal membership function sets, as shown in Figures. 9(a) and 9(b). They are labelled as NV (normal variance), LV (low variance), MV (medium variance), and HV (high variance). The output is also divided into four trapezoidal membership functions as shown in Figure. 9(c), their labels are NF (normal fluctuations), LF (low fluctuations), MF (medium fluctuations), and HF (high fluctuations). The crisp output of the Mamdani FL system can assume values between 0.5 and 4.5, where normal variations = 1, low variations = 2, medium variations = 3, and high variations = 4. The parameters of membership functions are determined according to the interpretation of the variance results by the authors. The set of rules that classifies the inputs variance is show in Table 2; there, one rule can be read as follows if (variance Mx is NV and variance My is NV) (light gray) then the geomagnetic fluctuations magnitude is NF (dark gray), and so on.

Geomagnetic Fluctuations Magnitude	Variance (M_y)			
	NV	LV	MV	HV
Variance (M_x) NV	NF	NF	LF	MF
LV	LF	LF	MF	HF
MV	LF	MF	HF	HF
HV	MF	HF	HF	HF

Table 2. Rules table for the proposed FL
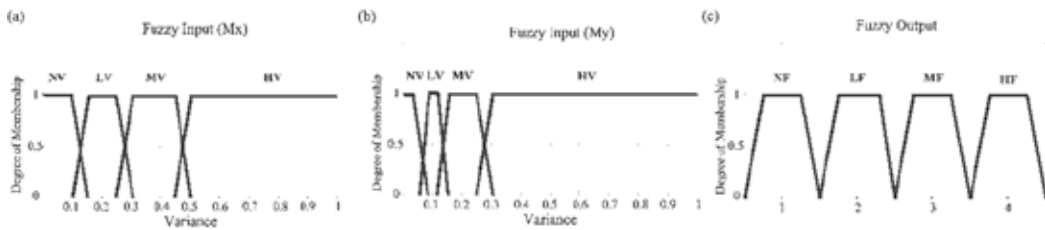
Figure 9. Membership functions: (a) Input Mx variance, (b) Input My variance, and (c) Output diagnosis.

The FL output for a calm period signal is shown in Figure. 10(a), where most of the results are Normal and only a few data indicate Low ULF geomagnetic variations. On the other hand, the outputs for the three geomagnetic signals associated to EQs indicate many Medium and High variations as shown in Figure. 10(b-d); therefore, if these results are obtained in future data they could be associated to seismic activities.
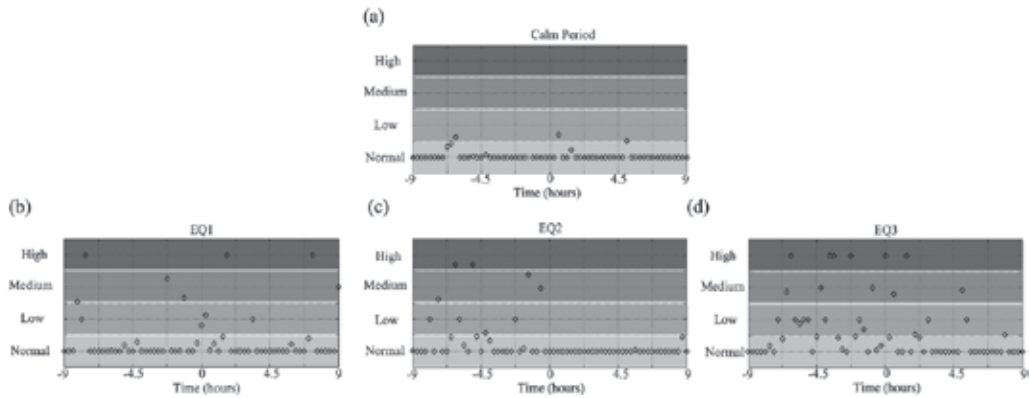
Figure 10. FL-based diagnosis for the analysed cases: (a) calm period and (b-d) seismic activities associated to ULF geomagnetic variations.

5. Conclusions

In this chapter, a new time-frequency study based on the EWT for analysing ULF geomagnetic signals, at Juriquilla station in Queretaro Mexico, is presented. In order to prove the effectiveness of the EWT algorithm; three real data of EQs are analysed. The results demonstrate that the proposal has a greater detectability than DWT for detecting anomalies before, during, and after the main shock since EWT allows selecting narrow time-frequency sub-bands, unlike the DWT where the calculated time-frequency sub-bands depend on sampling frequency of the time signal. Further, the variance, a statistical complementary analysis, shows that a seismic event can be detected from 8 to 5 hrs before it occurs. It also indicates that relevant information can be obtained from 563 to 1473 km (epicenter distance) to the testing station. Therefore, the proposed time-frequency analysis can extract the abnormal signals in the ULF range of the EP related to different stages of the EQ preparation. Finally, the proposed FL system can automatically classify the magnitude variations of the EP into Normal, Low, Medium, and High variations using both Mx and My signals, where is found that Medium and High variations could be associated to seismic activities.

In a future work, the overall methodology will be implemented into a digital signal processor (DSP) for online and continuous monitoring of ULF geomagnetic variations and possibly used for obtain a implicit correlation between the seismic magnitude and the ULF geomagnetic signals.

Author details

Omar Chavez Alegria[1], Martin Valtierra-Rodriguez[2], Juan P. Amezquita-Sanchez[1*],
Jesus Roberto Millan-Almaraz[2], Luis Mario Rodriguez[3], Alejandro Mungaray Moctezuma[3],
Aurelio Dominguez-Gonzalez[1] and Jose Antonio Cruz-Abeyro[4]

*Address all correspondence to: jamezquita@uaq.mx

1 Engineering Department, Autonomous University of Queretaro, Queretaro, Mexico

2 Physics and Mathematics Department, Autonomous University of Sinaloa, Cualiacan,
Sinaloa, Mexico

3 Engineering Department, Autonomous University of Baja California, Baja California, México

4 Geoscience Centre, National Autonomous University of Mexico, Juriquilla, Queretaro,
Mexico

References

[1] Zhang, Q., Zhang, Y., Yang, X. Su, B. Automatic Recognition of Seismic Intensity Based
on RS and GIS: A Case Study in Wenchuan Ms 8.0 Earthquake of ChinaThe Scientific
World Journal 201420141-8

[2] Chavez, O., Millan-Almaraz, J. R. Perez-Enriquez, R. et al.Detection of ULF geomagnet-
ic signals associated with seismic events in Central Mexico using Discrete Wavelet
TransformNatural Hazards and Earth System Sciences2010; 1012)2557–2564.

[3] Moriya, T., Mogi, T., Takada, M.Anomalous pre-seismic transmission of VHF-band radio
waves resulting from large earthquakes, and its statistical relationship to magnitude of
impending earthquakesGeophysical Journal International2010;1802)858-870.

[4] Wei, C., Zhang, Y., Guo, X., et al. Thermal Infrared Anomalies of Several Strong Earth-
quakesThe Scientific World Journal2013; 20131-11.

[5] Lin, J.W.Ionospheric Anomalies Related to the (M = 7.3), August 27, 2012, Puerto
Earthquake, (M = 6.8), August 30, 2012 Jan Mayen Island Earthquake, and (M = 7.6),
August 31, 2012, Philippines Earthquake: Two-Dimensional Principal Component
AnalysisThe Scientific World Journal2013;20131-8.

[6] Gambino, S., Laudani, A. Manglagli, S.Seismicity Pattern Changes before the M=4.8
Aeolian Archipelago (Italy) Earthquake of August 16, 2010The Scientific World Jour-
nal2014; 20141-8.

[7] Warwick, J. W., Stoker, C. Meyer, T. R.Radio emission associated with rock fracture: Possible application to the great Chilean earthquake of May 22, 1960Journal of Geophysical Research: Solid Earth1982; 87B4)2851–2859.

[8] Johnston, M. J. S. Review of electric and magnetic fields accompanying seismic and volcanic activitySurveys in Geophysics1997;185)441–475.

[9] Hayakawa, M. Molchanov, O.Seismo Electromagnetics Lithosphere Atmosphere-Atmosphere-Ionosphere Coupling. TERRAPUB Tokyo Japan2002; 477.

[10] Otha, K., Watanabe, N. Hayakawa, M. The observation of ultra-low frequency emissions at Nakatsugawa, Japan, in possible association with the Sumatra, Indonesia, earthquake.International Journal of Remote Sensing 2007; 28(13-14) 3121-3131.

[11] Molchanov, O. A. Hayakawa, M.Seismo-Electromagnetics and Related Phenomena, History and latest results. TERRAPUB Tokyo Japan2008; 189.

[12] Kushwah, V., Singh, V. Singh, B. Ultra low frequency (ULF) amplitude observed at Agra (India) and their association with regional earthquakes. Physics and Chemistry of the Earth2009; 34(6) 367–272.

[13] Karia, S., Sarkar, S., Pathak, K., et al. Analysis of space- and ground-based parameters prior to an earthquake on 12 December 2009. International Journal of Remote Sensing 2013;34(21), 7779-7795.

[14] Borovsky, J. E. Denton, M. H. Exploring the cross correlations and autocorrelations of the ULF indices and incorporating the ULF indices into the systems science of the solar wind-driven magnetosphere. Journal of Geophysical Research: Space Physics2014; 119(6) 4307-4334.

[15] Hayakawa, M., Kawate, R., Molchanov, O. Yumoto. K. Results of ultra-low frequency magnetic field measurements during the Guam earthquake of 8 August 1993. Geophysical Research Letters1996: 23(3) 241–244.

[16] Hattori, K., Serita, A., Gotoh, K., et al. ULF geomagnetic anomaly associated with 2000 Izu islands earthquake swarm. Japan. Physics and Chemistry of the Earth 2004; 29(4) 425–436.

[17] Harada, M., Hattori, K. Isezaki, N. Transfer function analysis approach for anomalous ULF geomagnetic field change detection. Physics and Chemistry of the Earth2004; 29(4) 409– 417.

[18] Smirnova, N., Hayakawa, M.Gotoh. K. Precursory behavior of fractal characteristics of the ULF electromagnetic fields in seismic active zones before strong earthquakes. Physics and Chemistry of the Earth2004; 29(4) 445–451.

[19] Ida, Y., Hayakawa, M., Adalev, A.Gotoh, K. Multifractal analysis for the ULF geomagnetic data during the 1993 Guam earthquake. Nonlinear Processes in Geophysics2005; 12(2) 157–162.

[20] Ida, Y. Hayakawa, M. Fractal analysis for the ULF data during the 1993 Guam earth-quake to study prefracture criticality. Nonlinear Processes in Geophysics, 2006; 13(4) 409–412.

[21] Kotsarenko, A., Molchanov, O., Hayakawa, M., et al. Investigation of ULF magnetic anomaly during Izu earthquake swarm and Miyakejima volcano eruption at summer 2000, Japan. Natural Hazards and Earth System Sciences2005; 5 63–69.

[22] Kotsarenko, A., PerezEnriquez, R.,Lopez Cruz-Abeyro, J. A., et al. ULF geomagnetic anomalies of possible seismogenic origin observed at Teoloyucan station, Mexico, in 1999–2001: Intermediate and Short-Time Analysis. Tectonophysics2007; 431(1) 249–262.

[23] Hattori, K., Serita, A., Yoshino, C., et al. Singular spectral analysis and principal component analysis for signal discrimination of ULF geomagnetic data associated with 2000 Izu Island earthquake swarm. Physics and Chemistry of the Earth2006; 31(4) 281–291.

[24] Han, P., Hattori, K., Hirokawa, M., et al. Statistical analysis of ULF seismomagnetic phenomena at Kakioka, Japan, during 2001–2010. Journal of Geophysical Research: Space Physics 2014; 119(6) 4998-5011.

[25] Amezquita-Sanchez, J. P., Adeli, H. Signal Processing Techniques for Vibration-Based HealthMonitoring of Smart Structures. Archives of Computational Methods in Engineering 2014; DOI: 10.1007/s11831-014-9135-7.

[26] Jach, A. P., Kokoszka, Sojka, J., Zhu, L. Wavelet-based index of magnetic storm activity. Journal of Geophysical Research: Space Physics 2006; 111(A9) 1-11.

[27] Gilles, J. Empirical wavelet transform. IEEE Transaction on Signal. Processing2013; 61(16) 3999-4010.

Edited by Dumitru Baleanu

The book contains six chapters. The use of the progressive regressive strategy for biometrical authentication through the use of human gait and face images was investigated. A new lossy image compression technique that uses singular value decomposition and wavelet difference reduction technique was proposed. The best wavelet packet based selection algorithm and its application in image denoising was discussed. The scaling factor threshold estimator in different color models using a discrete wavelet transform for steganographic algorithms was presented. The extraction of features appearing in current signal using wavelet analysis when there is rotor fault of eccentricity and broken rotor bar was debated. The application of the empirical wavelet transform for seismic anomalies detection in ultralow-frequency geomagnetic signals was illustrated.

Photo by Egor Lisovskiy / DollarPhoto

IntechOpen